

Impairments in Coordinated Cellular Networks: Analysis, Impact on Performance and Mitigation

vorgelegt von
Dipl.-Ing. M.Sc.
Konstantinos Manolakis
geboren in Thessaloniki, Griechenland

von der Fakultät IV – Elektrotechnik und Informatik
der Technischen Universität Berlin
zur Erlangung des akademischen Grades

Doktor der Ingenieurwissenschaften
- Dr.-Ing. -

genehmigte Dissertation

Promotionausschuss:

Vorsitzender:	Prof. Dr.-Ing. Adam Wolisz	Technische Universität Berlin
Gutachter:	Prof. Dr. Giuseppe Caire	Technische Universität Berlin
Gutachter:	Prof. Dr. Christian Oberli	Pontificia Universidad Católica de Chile
Gutachter:	Prof. Dr. Constantinos Papadias	Athens Information Technology
Gutachter:	Dr.rer.nat. Volker Jungnickel	Fraunhofer Heinrich-Hertz-Institut

Tag der wissenschaftlichen Aussprache: 7. November 2014

Berlin 2015

Abstract

Base station cooperation is recognized as a key technology for future wireless cellular communication networks. Considering antennas of distributed base stations and those of multiple terminals within those cells as a distributed multiple-input multiple-output (MIMO) system, this technique has the potential to eliminate inter-cell interference by joint signal processing and to enhance spectral efficiency in this way. Although the theoretical gains are meanwhile well-understood, it still remains challenging to realize the full potential of such cooperative schemes in real-world systems.

Among other factors, such as the limited overhead for pilot symbols and for the feedback and backhaul, these performance limitations are related to channel and synchronization impairments, such as channel estimation, feedback quantization and channel aging, as well as imperfect carrier and sampling synchronization among the base stations. Because of these impairments, joint data precoding results to be mismatched with respect to the actual radio channel and the gains of base station cooperation are limited.

In order to analyze the signal distortion and the interference among the multiple users, which are caused by mismatched data precoding, it is required to model and investigate impairment effects isolatedly. Therefore, a signal model is provided for base-coordinated orthogonal frequency division multiplexing (OFDM) transmission with channel and synchronization impairments, and closed-form expressions are derived for the mobile users' signal-to-interference ratio (SIR). Analytical results are numerically verified and lead to practical system requirements. Based on channel modeling and outdoor measurements, inter-site distance limitations for interference-free and time-synchronous transmission are also investigated.

It is further discussed how to synchronize distributed base stations by using commercial oscillators locked to externally provided references, e.g. signals provided by Global Positioning System (GPS). Mitigation techniques including adaptive feedback compression and channel prediction are developed. Adaptive feedback compression keeps the channel mean square error (MSE) below a threshold and achieves more than order of magnitude overhead reduction. Doppler-delay based channel prediction reduces the delay-based MSE by 10 dB, approximately.

For evaluating purposes, the spatial channel model extended (SCME) as well as channel data from outdoor measurements are used. Multi-cellular simulations reveal that the users' SIR can be enhanced by 10 dB on average. Practically this means that larger feedback delays, higher mobilities and a larger number of users can be supported in coordinated multi-point (CoMP), compared to than previously believed.

Zusammenfassung

Die Kooperation von Basisstationen wird als eine vielversprechende Technik für zukünftige drahtlose Kommunikationsnetze angesehen. Diese Technik betrachtet die Antennen von Basisstationen zusammen mit den Antennen mobiler Nutzer innerhalb von Zellen als ein räumlich verteiltes multiple-input multiple-output (MIMO) System und eröffnet dadurch die Möglichkeit, durch eine gemeinsame Signalverarbeitung die Inter-Zell-Interferenz zu beseitigen und die spektrale Effizienz zu erhöhen. Obwohl mittlerweile die theoretischen Grenzen solcher kooperativer Schemata bekannt und gut verstanden sind, besteht die größte Herausforderung noch immer in der Umsetzung und praktischer Realisierung und zwar in der Form, dass das theoretische Potential vollständig ausgeschöpft wird.

Zum einen ist der vertretbare Mehraufwand für Pilotsymbole, Feedback und Backhaul begrenzt. Zum anderen ist die Performanz auf Grund von imperfekter Kanalkennntnis und Synchronisation limitiert, welche durch Kanalschätzung, Feedbackquantisierung, Alterung der Kanalinformation, sowie durch unterschiedliche Träger- und Abtastfrequenzen zwischen den Basisstationen entsteht. Diese Beeinträchtigungen haben zur Folge, dass die gemeinsame Vorkodierung der Daten in Bezug auf den tatsächlichen drahtlosen Übertragungskanal fehlangepasst ist und sich so die Kooperationsgewinne deutlich reduzieren.

Um die Signalverzerrung und die Interferenz zwischen den Nutzern, die durch fehlangepasste Vorkodierung verursacht wird zu analysieren, müssen die Einflussfaktoren jeweils individuell untersucht werden. Dazu wird zunächst ein Signalmodell für die koordinierte orthogonal frequency division multiplexing (OFDM)-Übertragung entwickelt, welches die Effekte der imperfekten Kanalkennntnis und Synchronisation berücksichtigt und zudem erlaubt, analytische Ausdrücke für das Signal-zu-Interferenz Verhältnis (SIR) der mobilen Nutzer herzuleiten. Die analytischen Ergebnisse werden anschließend numerisch verifiziert und entsprechende Systemanforderungen werden spezifiziert. Unter der Verwendung geeigneter Kanalmodelle sowie realer Kanalmessdaten werden Schranken für den maximalen Abstand zwischen Basisstationen abgeleitet, welche eine interferenzfreie und zeitsynchrone Datenübertragung erlauben.

Weiterhin wird die Synchronisation von verteilten Basisstationen diskutiert, welche auf der Nutzung kommerzieller Oszillatoren basiert, welche an externe Referenzen, z. B. Global Positioning System (GPS), angebunden sind. Es werden Methoden zur Abschwächung der Beeinträchtigungen entwickelt, wie etwa adaptive Feedbackkompression und Kanalprädiktion. Die adaptive Feedbackkompression ermöglicht es den mittleren quadratischen Kanalschätzfehler (MSE) unterhalb einer bestimmten Schranke zu halten und dabei gleichzeitig die Feedbackinformation um eine Größenordnung zu reduzieren. Dagegen ist eine auf

Doppler-Verzögerungen basierende Kanalprädiktion in der Lage den MSE um 10 dB zu reduzieren.

Zur Bewertung der Performanz werden das spatial channel model extended (SCME) Kanalmodell sowie reale Kanalmessdaten verwendet. Multi-zellulare Simulationen zeigen, daß das mittlere SIR pro Nutzer um 10 dB angehoben werden kann. Praktisch bedeutet dies, daß entgegen der bisherigen Meinung neben größeren Feedbackverzögerungen und einer höheren Mobilität auch eine größere Anzahl von Nutzern unterstützt werden kann.

Acknowledgements

During the previous years, which I spent as member of the scientific staff at the Technische Universität Berlin and the Fraunhofer Heinrich Hertz Institute, I had the opportunity to work on my dissertation in a very inspiring academic environment. Part of this work was financially supported by the Deutsche Forschungsgemeinschaft (DFG), which I would like to acknowledge here.

First of all, I feel obliged to thank Prof. Adam Wolisz, who supported me in a critical phase and kept advising me until the end of my doctoral studies. I would also like to express my gratitude to Prof. Giuseppe Caire for his effort to review my thesis and for being the main examiner, and to Prof. Constantinos Papadias, who also reviewed my thesis and served as a member of the committee.

I am very thankful to Prof. Christian Oberli for his advising during the previous years. Through our close collaboration, and thanks to his excellent teaching skills and large amount of patience, I could learn a lot from him. Moreover, Christian offered me the opportunity to work with him and his group at the Pontificia Universidad Católica in Santiago, Chile. The periods I spent there were highly productive and enriched me with diverse experience, for which I feel very lucky and thankful to him.

The next few lines will be hardly enough for expressing my gratitude to Dr. Volker Jungnickel, the person who made it possible for me to enter the world of scientific research and who supported me the first steps. Through all the years, I enjoyed his exemplary guidance and the privilege having him as a mentor. On this way, which was often not easy, Volker's encouragement and motivation helped me to move forward.

My thanks further go to colleagues from the TU Berlin and the Fraunhofer HHI, with whom we spent plenty of time, shared new ideas and a lot of nice memories.

The last part of my acknowledgements is dedicated to my family, to whom I own a lot, and from whom I have been always receiving a lot of support and love. My wife Marina has been on my side, and I would like to thank for her understanding and for her love.

Contents

1	Introduction	1
1.1	Motivation	1
1.2	Goals and objectives	3
1.3	Structure and main contributions	4
1.4	Notation and definitions	7
2	CoMP with Impairments: A High-Level Model and Interference Analysis	9
2.1	Multiple antennas and coordinated transmission	11
2.1.1	Multiple-input multiple-output (MIMO) systems	11
2.1.2	Coordinated multi-point (CoMP)	15
2.2	Signal model for the impaired CoMP downlink	18
2.3	Analysis of signal and interference power	21
2.4	Transmit power in JT CoMP systems	24
2.5	Evaluation of downlink SIR	25
2.6	Summary of Chapter 2	26
3	Inter-site-distance limitations for CoMP	29
3.1	Inter-symbol-interference in JT CoMP using OFDM	30
3.2	Modeling of the multi-cell broadband radio channel	31
3.3	Parameter extraction from multi-cell channel measurements	33
3.4	Model validation and results	35
3.5	Summary of Chapter 3	38
4	Synchronization Impairments in OFDM-based CoMP	41
4.1	MIMO-OFDM signal model with carrier and sampling frequency offsets	43
4.2	Precoded multi-cell downlink signal model	47
4.3	Analysis of signal and interference powers	49
4.3.1	Power of the user's self-signal	49
4.3.2	Power of the inter-user interference	52
4.3.3	Power of the inter-carrier interference	53
4.3.4	ICI-to-IUI ratio and SIR	54
4.3.5	The value of user selection in JT CoMP and an SIR bound	55
4.4	Evaluation and numerical validation	56
4.5	Model simplification and MSE analysis	59

4.6	Recommendations for CoMP system design	63
4.7	Summary of Chapter 4	64
5	Channel Impairments and Mitigation Techniques for CoMP	67
5.1	Analysis of JT CoMP with channel impairments	67
5.1.1	Signal model	68
5.1.2	Power analysis of self-signal and inter-user interference	71
5.1.3	Model simplification and MSE analysis	74
5.2	Feedback compression for JT CoMP	77
5.2.1	CSI feedback in multi-cellular JT CoMP systems	77
5.2.2	A feedback compression scheme for JT CoMP	78
5.2.3	Evaluation of feedback compression scheme	87
5.3	Compensation by channel prediction	91
5.3.1	Doppler-delay based channel prediction	93
5.3.2	Evaluation of the channel MSE	96
5.4	SIR gains by mitigation of channel impairments in JT CoMP	106
5.5	Summary of Chapter 5	108
6	Conclusions and Outlook	111
6.1	Summary and conclusions	111
6.2	Outlook towards next generation systems	113
7	Appendices	117
7.1	Appendices of Chapter 2	117
7.1.1	Mean value of the eigenvalues of the Wishart matrix	117
7.1.2	Mean value of the inverse eigenvalues of the Wishart matrix	118
7.2	Appendices of Chapter 4	119
7.2.1	Analysis of K_U , K_{IUI} and K_{ICI}	119
7.2.2	Analysis of B_1 and B_2	119
7.2.3	Power of a periodic band-limited function sampled with an offset	121
7.3	Appendices of Chapter 5	123
7.3.1	High resolution estimator	123
	List of Abbreviations	125
	List of Figures	128
	List of Tables	133
	Publication List	137
	Bibliography	141

1 Introduction

1.1 Motivation

During the past years, wireless radio communications have met a huge evolution, especially commercial cellular telephony and data transmission. Probably the most groundbreaking innovation has been the development of multiple-antenna systems, also known as multiple-input multiple-output (MIMO). These techniques have gained an extraordinary interest, as they can substantially increase the maximal amount of data that can be transmitted over the radio channel, also termed as *channel capacity*.

Considering typical urban environments, multi-path propagation of radio waves typically results into independent channels between multiple transmit and receive antennas. In multiple-antenna systems, this enhances the spatial dimension of the MIMO channel and offers additional degrees of freedom. For data transmission between a transmitter and a receiver equipped with multiple antennas, these additional degrees of freedom can be used either for the transmission of multiple data streams, which increases the achievable data rate, or for a multiple transmission or reception of a single data stream, which provides a connection with higher quality.

Cellular networks using MIMO can jointly serve multiple users on the same time and frequency resource. In the downlink transmission, a so-called *spatial precoding* is performed at the base station, for which knowledge of the full channel matrix is required. Precoded signals are simultaneously transmitted over the MIMO channel in a way that at the geographic location of each user, the transmitted signals from multiple antennas overlap constructively for the user's own data signal and destructively for the other users' signals. In this way, each user ideally receives its own signal, free of inter-user interference. Of course, in multi-cellular networks there will be still substantial interference between the cells limiting the overall performance.

Base station cooperation, also known as *coordinated multi-point (CoMP)*, can be understood as an extension of MIMO, in which antennas of multiple distributed base stations and those of multiple users served within those cells are considered as a geographically distributed MIMO system. Going a step further than MIMO, CoMP aims to eliminate the interference between adjacent cells, which is particularly helpful for the users close to the border between cells.

For realizing the potential of multiple antenna techniques at a reasonable cost of computational complexity, simple signal processing at the transmitter and the receiver side needs to be considered. Providing high data rates to the users also requires a large band-

width, which means that the transmission scheme has to deal with broadband channels, which are typically characterized by strong frequency selectivity because of multi-path proportion effects. A technique fulfilling those requirements is orthogonal frequency division multiplexing (OFDM). Thanks to its fast Fourier transform (FFT)-based implementation, OFDM has moderate computational requirements and is relatively simple to implement. Furthermore, this multiplexing technique lends itself very well for transmission over frequency-selective channels, as it divides the available bandwidth in a number of narrow frequency bands, where each of them observes frequency-flat fading and can be processed as a single-carrier transmission. Mapping data onto those subcarriers, and transmitting parallel data streams over orthogonal sub-channels offers large frequency diversity gains. The combination of MIMO and OFDM offers flexibility in assigning spatial streams and frequencies to the users and leads to high spatial and frequency diversity gains.

Realizing the theoretical performance gains of MIMO under real-world conditions, and especially the ones of distributed CoMP, is a challenging goal and is considered as an open research field. The full gains of MIMO techniques can be only attained under perfect knowledge of the radio channel and perfect time and frequency synchronization among distributed transmitters. This requirement stems from the fact that precoded signals must align in both magnitude and phase with respect to the transmission channel so that for each user, its own signal contributions overlap constructively and the signals from other users cancel out.

However, in real-world systems there are always precoder misalignments due to several impairment effects, making the deployment of distributed CoMP a non-trivial task. First, base stations obtain quantized estimates of the channel rather than a perfect knowledge of it. In addition, there is a delay, equal to the time between when the channel is estimated and when this estimate is used for precoding the data transmission. Due to time variance of the mobile radio channel, the calculated precoder will be thus outdated with respect to the channel over which data are transmitted. Furthermore, precoded signals need to be transmitted coherently from multiple distributed base stations, which must be synchronized accurately in their carrier and sampling frequencies. As distributed base stations use their own local oscillators and sampling references, synchronization conditions can be significantly more challenging in CoMP than for non-distributed transmission. It is noted that high sensitivity to synchronization impairments is also a characteristic of OFDM [30]. Finally, due to propagation delay differences to mobile users, limitations in time synchronization are also stricter than for non-distributed architectures. All the above transmission misalignments impose a precoder mismatch and several restrictions and cause interference among the jointly served users, which is a reason for performance degradation.

The high sensitivity of CoMP to channel and synchronization impairments has been also clearly observed by field trials conducted at the multi-cellular test network at the Fraunhofer Heinrich Hertz Institute (HHI) in Berlin, Germany. It quickly became evident how critical those effects are and that mitigation techniques will be needed in order to

perform successfully interference-free coordination of distributed base stations. However, the high complexity of the deployed adaptive MIMO procedures and a multitude of control loops for gain, time and frequency synchronization, channel estimation and channel state information feedback mask the true sources of performance degradation and limit insights into what adequate requirements are. These effects can only be figured out by careful theoretical analysis with support from experimental observation.

1.2 Goals and objectives

This thesis investigates wireless cellular networks that use base station coordination, under realistic conditions where transmission is impaired by imperfect channel knowledge and synchronization misalignments. The objective of this work consists within the analysis and investigation of the influence of those impairments onto the performance of CoMP systems and the development of appropriate mitigation techniques for compensating the performance losses. The goals include fundamental modeling and analysis in order to understand the essential effects, system performance evaluation and requirement specification as well as the development of novel concepts and practical solutions. In order to systematically approach the overall problem, the objectives are organized as follows.

1. **System modeling and mathematical analysis**
2. **Evaluation of performance degradation and specification of system requirements**
3. **Development of mitigation techniques and evaluation of performance gains and losses**

The definition and fulfillment of the above goals is based on following *hypotheses*:

1. The performance degradation of a distributed MIMO-OFDM system due to channel and synchronization impairments can be described with a unified mathematical framework and a common signal model.
2. Impairments cause critical problems that can limit the performance gains promised by CoMP technology to a point at which it provides no advantage over networks without base station coordination. Performance evaluation provides system requirements for beneficial network coordination.
3. Counting with accurate signal models allows for formulating mitigation algorithms for the mentioned impairments. These techniques yield substantially better performance.

In terms of *methodology*, the work begins with providing a system and signal model for the impaired CoMP. The mathematical model is used for deriving general analytical expressions for the mobile users' signal-to-interference ratio (SIR). The signal model is

further specialized for the cases of channel aging and synchronization misalignments and OFDM is included. For each impairment, a deep investigation of its role, as well as evaluation of the impact of several parameters onto the system performance is carried out. Analytically derived results are verified by numerical simulations. The results are used for specifying system requirements and discussing performance limitations. Furthermore, new mitigation techniques such as adaptive feedback compression and Doppler-delay channel prediction are introduced. The proposed techniques enable spectrally efficient CoMP transmission for practical systems, also considering system and computational complexity as well as hardware capability. The system concept is re-evaluated after compensating the impairment effects in terms of realistic multi-cellular simulations using Third Generation Partnership Project (3GPP) Long Term Evolution (LTE) parameters [31]. For data transmission, the spatial channel model extended (SCME) [32] as well as channel data from outdoor broadband measurements are considered in the multi-cellular simulations.

1.3 Structure and main contributions

In what follows, an outline of this work is provided and the main contributions are briefly summarized for each chapter. The relevant own publications are also mentioned.

The problem addressed in **Chapter 2** is the analysis of the inter-user interference and the resulting SIR in CoMP systems with impairments. After providing basic background knowledge on MIMO and CoMP, a high-level system and signal model for the CoMP downlink with mismatched zero-forcing (ZF) precoding due to impairments is derived. Based on this mathematical model, which is used and further extended through this work, a power analysis of self-user signal and inter-user interference is provided. Using random matrix theory and the statistical properties of the singular values of the channel matrix, the following main results are obtained.

- Analytical expressions for the users' mean SIR in a Rayleigh fading channel and an SIR upper bound. The SIR is found to be inversely proportional to the channel mean square error (MSE), grows with the numbers of base stations and drops with the number of users.
- The value of user selection for gaining robustness against imperfect precoding is shown. Users whose channel vectors are nearly orthogonal should be jointly served, so that the SIR approaches the upper bound. Some recent results indicate that realistic selection yields channel matrices that are more close to the Rayleigh fading bound, which is also derived here.

Part of the work included in Chapter 2 has been published in [9] and [19].

Chapter 3 investigates the inter-site distance (ISD) limitations of base-coordinated wireless networks, so that time synchronization of OFDM signals with propagation delay differences and interference-free removal of the cyclic prefix are possible.

- A statistical channel model for broadband multi-point transmission is provided, verified and parameterized by real-world outdoor channel measurements in terms of root mean square (RMS) delay spread and 95% excess delay.
- It is found that by using a larger antenna downtilt, significantly smaller channel delay spreads can be realized and the inter-cell interference becomes much more concentrated.
- Model-based prediction of the excess delay statistics for larger ISDs indicates that base station cooperation is feasible without violating the LTE short cyclic prefix in more than 5% of the cases.

Part of the work included in Chapter 3 has been published in [18].

Chapter 4 investigates CoMP systems with synchronization misalignments and their influence on the system performance. The main contributions and findings are following.

- An exact signal model for MIMO-OFDM with individual carrier and sampling frequency offsets at all transmitters and receivers is provided. The model is further applied to the CoMP downlink using ZF precoding.
- It is shown that carrier frequency offsets have a significantly higher impact onto the signal distortion than sampling frequency offsets.
- Analytical expressions for the mean power of the users' self-signal, inter-user and inter-carrier interference are provided. For practical purposes, the inter-user interference dominates on the inter-carrier interference.
- CoMP synchronization misalignments on the terminals' side do not generate inter-user interference, but only inter-carrier interference.
- SIR expressions are provided for the Rayleigh fading channel and an upper SIR bound are provided for CoMP. The mean SIR drops with the square of time and is inversely proportional to the variance of the base stations' frequency offsets. The SIR grows with the numbers of base stations and and drops with the number of users.
- The model is simplified and expressions for the (equivalent) channel MSE due to carrier frequency offsets is derived.
- Synchronization requirements for CoMP are synthesized. In order to meet those requirements, distributed synchronization using oven-controlled crystal oscillators (OCXOs) locked to either a Global Positioning System (GPS) reference, or another precise clock provided over the backhaul network is proposed.

Part of the work included in Chapter 4 has been published in [1], [8] and [92].

In **Chapter 5**, the high-level signal model for CoMP with mismatched precoding, which has been derived in Chapter 2, is specialized for imperfect channel estimation, feedback quantization and channel aging and analytical SIR expressions are derived. Relations between channel estimation and quantization accuracy, mobility and feedback delay are elaborated, while system requirements and limitations are discussed. The model is simplified and MSE expressions are provided for each channel impairment. Results show that channel aging effects is mainly responsible for the performance limitation of CoMP.

Towards mitigation, a feedback compression technique is proposed for minimizing the feedback overhead and reducing the feedback delay. The time-domain method considers noise and interference, while clustering of the strongest base stations is also included. The scheme is evaluated over the SCME as well as over measured channels.

Channel aging effects are combated by channel prediction, where channel taps are estimated over a short observation time, before a high-resolution algorithm detects the major Doppler frequencies for each channel tap and prediction is performed by time extrapolation. Evaluation over the SCME as well as using data from outdoor channel measurements is performed. The main results are following.

- The channel MSE can be reduced by around 10 dB for typical feedback delays between 2 and 10 ms. Larger delays and higher mobility can be supported, compared to than previously believed.
- The method does not need additional transmit or receive antennas and is able to estimate the Doppler frequencies from a short channel observation time.
- Computationally complex estimation of Doppler frequencies can be implemented at the base station without performance penalties.
- Multi-cellular simulations using CoMP were performed and SIR gains of around 10 dB were observed when using Doppler-delay channel prediction, compared to using only the delayed feedback.

Part of the work included in Chapter 5 has been published in [87], [106], [7], [8] and [11].

The major results of this work are summarized in **Chapter 6**. Conclusions on CoMP with impairments and a higher-level discussion are provided. Furthermore, open research topics are highlighted, with an outlook towards next-generation (5G) systems. A vision of a 5G network is discussed, which includes CoMP, small cells and a very large number of transmit antennas (massive MIMO). Finally, a concept is drawn for a 5G network, which shall integrate in a practical way all above technologies.

Appendices are included in **Chapter 7**, where notation and definitions, as well as mathematical proofs of several expressions and statements used in this work are provided.

1.4 Notation and definitions

Scalars, vectors and matrices

Vectors are written in bold small letters \mathbf{x} , while for matrices bold capital letters are used \mathbf{H} . Single elements of a matrix are indicated by a two-letter subscript, so that H_{ub} points to the element in row u and column b of matrix \mathbf{H} . The element found in row u of vector \mathbf{x} is denoted by x_u .

For scalars, $[\cdot]^*$ denotes the complex conjugate operator, while for matrices and vectors the transpose and conjugate transpose (Hermitian) operators are given by $[\cdot]^T$ and $[\cdot]^H$, respectively. The inverse of a matrix \mathbf{H} is denoted by \mathbf{H}^{-1} . Notation $\text{tr}(\mathbf{X})$ stands for the trace of an N -by- N square matrix \mathbf{X} , i.e. $\text{tr}(\mathbf{X}) = \sum_{n=1}^N X_{nn}$. A diagonal matrix \mathbf{Z} with on-diagonal elements given by the vector \mathbf{x} , is denoted by $\mathbf{Z} = \text{diag}(\mathbf{x})$. The identity matrix is represented by \mathbf{I} . The Euclidean norm of vector \mathbf{x} is $\|\mathbf{x}\|^2 = \mathbf{x}^H \mathbf{x}$, while $|s|^2 = ss^*$ is the absolute square of scalar s .

For a complex variable x , its real and imaginary part are denoted as $\Re\{x\}$ and $\Im\{x\}$, respectively. The space of integer, real and complex numbers is given by \mathbb{N} , \mathbb{R} and \mathbb{C} , respectively. For the continuous time and frequency, letters t and f are used. For the discrete time index we use n , whereas k is used for the discrete frequency index. For a scalar time-domain function $s(n)$, its corresponding frequency-domain representation is $S(k) = \mathcal{F}\{s(n)\}$, where $\mathcal{F}\{\cdot\}$ denotes the discrete Fourier transform (DFT). The inverse discrete Fourier transform (IDFT) is denoted by $\mathcal{F}^{-1}\{\cdot\}$. For the continuous domain, the same symbols as for the discrete domain are used for the Fourier transform and its inverse, e.g. $S(f) = \mathcal{F}\{s(t)\}$.

Random variables and matrices

The expectation operator over all random variables is denoted by $\mathbb{E}\{\cdot\}$. If an subscript is used as $\mathbb{E}_x\{\cdot\}$, the expectation is considered only with respect to the random variable x . The conditional expectation given event A is denoted by $\mathbb{E}\{\cdot|A\}$.

A random variable $x \in \mathbb{R}$ following a Gaussian (normal) distribution with mean value μ and variance σ^2 is denoted as $\mathcal{N}(\mu, \sigma^2)$. Its probability distribution function (pdf) is given by

$$f(x)_{\text{Gaussian}} = \frac{1}{\sigma\sqrt{2\pi}} e^{-\frac{(x-\mu)^2}{2\sigma^2}}.$$

The distribution described by $\mathcal{N}(0, 1)$ is known as standard Gaussian distribution. The generalization of the one-dimensional normal distribution to higher dimensions is given by the multivariate normal distribution. For example, a random vector \mathbf{x} , where every linear combination of its components follows a normal distribution. The multivariate normal distribution is denoted by $\mathcal{N}(\mu, \mathbf{\Sigma})$, with mean vector $\mu = \mathbb{E}\{\mathbf{x}\}$ and covariance matrix $\mathbf{\Sigma} = \mathbb{E}\{[(\mathbf{x} - \mu)(\mathbf{x} - \mu)^T]\} = \mathbb{E}\{\mathbf{x}\mathbf{x}^T\} - \mu\mu^T$. The inverse covariance matrix is denoted by $\mathbf{\Sigma}^{-1}$.

A complex-valued random variable $z = x + j y$, which real and imaginary parts x and y are Gaussian distributed is characterized by the complex Gaussian (normal) distribution. It is noted that symbol j is used for $\sqrt{-1}$. For multivariate distributions, the corresponding matrix notation is $\mathbf{z} = \mathbf{x} + j \mathbf{y}$. In this work, we refer to the circularly symmetric complex normal distribution, which corresponds to the case of zero mean and zero relation matrix, i.e. $\mu = \mathbb{E} \{\mathbf{z}\} = 0$ and $\mathbf{C} = \mathbb{E} \{(\mathbf{z} - \mu)(\mathbf{z} - \mu)^T\} = \mathbb{E} \{\mathbf{z}\mathbf{z}^T\} = 0$. This special case is denoted by $\mathbf{z} \sim \mathcal{CN}(0, \mathbf{\Sigma})$, where $\mathbf{\Sigma}$ is the (complex-valued) covariance matrix, given by $\mathbf{\Sigma} = \mathbb{E} \{(\mathbf{z} - \mu)(\mathbf{z}^* - \mu)^T\} = \mathbb{E} \{\mathbf{z}\mathbf{z}^H\}$.

The Rayleigh fading channel

The Rayleigh distribution is defined as follows. Given a random complex number, which real and imaginary parts are independent and identically distributed (i.i.d.) Gaussian with zero mean and variance σ^2 , its absolute value will be Rayleigh distributed. The pdf of a Rayleigh distributed variable x is given by

$$f(x)_{\text{Rayleigh}} = \frac{x}{\sigma} e^{-\frac{x^2}{2\sigma^2}}, \quad x \geq 0.$$

Throughout this thesis, it will be often referred to the Rayleigh fading channel, especially during mathematical derivations. The model is defined as follows. In the time domain, the channel impulse response is modeled by complex Gaussian i.i.d. circularly symmetric multi-path components (channel taps). Optionally, an exponential power delay profile (PDP) can be included, while impulse responses are always assumed to be shorter than the OFDM cyclic prefix. If not mentioned differently, for the multi-user multi-cellular scenario, i.i.d. matrix entries are considered, based on the assumption that base stations and mobile users are located far enough from each other, so that their channels are uncorrelated. Furthermore, the mean channel channel power, denoted by σ_h^2 , will be assumed to be the same for all entries of the channel matrix. For simplicity, and as long as not affecting the generality of the results, $\sigma_h^2 = 1$ will be used.

2 CoMP with Impairments: A High-Level Model and Interference Analysis

On the way towards increasing spectral efficiency

Wireless communications have grown dramatically, a fact that has put large pressure on using the electromagnetic spectrum efficiently. Today, most wireless applications such as cellular communications and wireless networking operate in frequency bands allocated in the crowded spectrum between 800 MHz and 5.8 GHz. Using frequencies below that range would require antennas with an inconveniently large form factor, besides the fact that allocating the bandwidth would be problematic. On the other hand, frequencies above that range are commonly regarded less attractive due to increasing path loss and to a growing requirement of line-of-sight conditions for the communication. Furthermore, hardware components meeting the system requirements become more expensive at higher frequencies. Thus, frequencies that are at the same time available and commercially appealing for local and metropolitan area wireless applications are quite limited, making the radio spectrum a scarce resource. Maximizing the efficiency of spectrum usage is therefore a crucial and constant goal guiding the evolution of wireless communications.

The theoretical foundation of *spectral efficiency* lies in the concept of *channel capacity*, first established by C. E. Shannon in 1948 for the additive white Gaussian noise (AWGN) channel [33]. Since then, the concept has been extended with contributions from many researchers for a variety of transmission channels. In essence, the channel capacity of a given channel determines the maximum spectral efficiency that can be achieved. Unfortunately, knowing the theoretical capacity of a channel gives very few clues about how this can be attained in practice. Therefore, since the time of Shannon's work, scientists and engineers have been on an endless quest for approaching these maximal achievable spectral efficiencies by innovating in a vast variety of fields, including modulation techniques, power allocation, channel coding and design of signal waveforms.

Including some of those innovative techniques, the Global System for Mobile Communications (GSM) cellular standard was developed during the 1980's as the first cellular system with fully digital transmission. Moreover, it allowed simple frequency reuse in space and thereby a very robust integration of smaller cells to provide more throughput where more users are concentrated. Also termed 2G, this standard is based on a combination of Frequency Division Multiple Access (FDMA) and Time Division Multiple Access (TDMA) and achieved a huge commercial success, through which mobile telephony became part of

the every day life for a large part of the world population. In the 1990's, a family of 3G cellular standards such as Universal Mobile Telecommunication System (UMTS) and more recently Evolved High-Speed Packet Access (HSPA+) were developed, using Code Division Multiple Access (CDMA) as a channel access method. CDMA allows for transmitting data simultaneously to several mobile users on the same time and frequency resource, by using spread-spectrum techniques and special coding scheme. In this way, frequency is fully reused in each cell, which is more efficient but requires advanced signal processing for inter-cell interference mitigation. The use of CDMA promised a great advantage at the cell edge in case of fully frequency reuse, where macro-diversity effects can be exploited by serving the user from two base stations with the same code (soft hand-off). However, the number of jointly served users and the interference among them depends on orthogonality properties. Long cell-specific scrambling and coding sequences can quickly lead to highly-complex and non-practical detection schemes.

However, the practically achievable spectral efficiency over wireless channels with the above techniques seemed to run into a saturation level as approaching the Shannon AWGN bound for the point-to-point link. A fundamentally innovative technique revealed that using multiple antennas can yield a capacity growth proportional to number of antenna elements [34, 35].

In parallel, a new access scheme, named orthogonal frequency division multiple access (OFDMA), was used to enable spectrally efficient transmission in combination flexible scheduling schemes. Each user obtains its best resources in the time-frequency grid, while providing proportional fairness among the users. In this way, the fast fading can be exploited to maximize the spectral efficiency.

The most advanced form of multiple-input multiple-output (MIMO) communications has recently taken shape with the development of the mobile communications standard known as Long Term Evolution – Advanced (LTE-A) [36, 37]. Its key innovation is to use smart network coordination techniques in order to establish a MIMO network including geographically distributed base stations and several users. The scheme whereby a cluster of cooperating base stations is treated as a global distributed MIMO system is often referred to as *coordinated multi-point (CoMP)*. The dimension of a CoMP system is equal to the total number of transmit antennas jointly available to the entire cluster of base stations. Enabling the full-dimension of a cooperation cluster, and hence exploiting its full spectral efficiency, requires that all base stations cooperate by carrying out joint signal processing to precode the signals in the downlink and to jointly decode the signals received in the uplink. In this way, huge spectral efficiency gains become possible, stemming from the reduction of inter-cell and inter-user interference served on the same time and frequency resource. In fact, CoMP is the correct answer to achieve full frequency reuse in cellular networks.

2.1 Multiple antennas and coordinated transmission

This section gives an introduction to the fundamentals of multiple-antenna systems and coordinated multi-point transmission for wireless networks. Here, some background knowledge is provided, part of which is also included in the courses on MIMO systems, which are offered by the School IV - Electrical Engineering and Computer Science of the Technische Universität Berlin (TUB). Further material related to the course and more details on the MIMO fundamentals appears in [38].

2.1.1 Multiple-input multiple-output (MIMO) systems

It is important to mention that the idea of using multiple antennas to enhance the performance of wireless transmission has been originally investigated by Jack Winters [39, 40]. From those first works it became clear that multi-antenna concepts yield diversity and in addition, enable co-channel interference cancellation. The breakthrough contributions on spatial data multiplexing were provided by Foschini, who investigated the first coding schemes in [41] and by Telatar, who derived the first fundamental formulas for the capacity of the MIMO channel in [35].

The capacity of the MIMO channel

The motivation for using MIMO is that parallel data transmission is more spectrally efficient than serial transmission. It is known from [33] that for serial data transmission, the capacity C_{serial} over the AWGN channel is given by Shannon's formula

$$C_{\text{serial}} = BW \cdot \log_2(1 + \text{SNR}), \quad (2.1)$$

where the signal-to-noise ratio (SNR) used in (2.1) is measured at the receiver and BW denotes the bandwidth in Hz. Now, N_t parallel transmitters are considered, and for a fair comparison with serial transmission, the transmit power is divided among them yielding a per-stream SNR given by $\text{SNR}_i = \frac{\text{SNR}}{N_t}$. Then, the sum capacity for N_t parallel streams results into

$$C_{\text{parallel}} = N_t \cdot BW \cdot \log_2 \left(1 + \frac{\text{SNR}}{N_t} \right). \quad (2.2)$$

As seen by (2.2), the capacity scales with the number of transmitters, as N_t appears in front of the logarithm as well as inside of it. If N_t grows, the term in the logarithm decreases the capacity curve. But the linear factor N_t in front of the logarithm overcompensates this decreasing. Finally, increasing the number of parallel streams N_t leads to a steeper slope of the spectral efficiency curve ($\frac{C}{BW}$) over the SNR in dB, as illustrated in Figure 2.1. It becomes thus evident that the capacity of multi-stream transmission is significantly higher at any SNR. By doubling the SNR in a serial transmission in the high SNR regime, spectral efficiency increases by 1 bit/s/Hz, while the corresponding gain is N_t bit/s/Hz for parallel

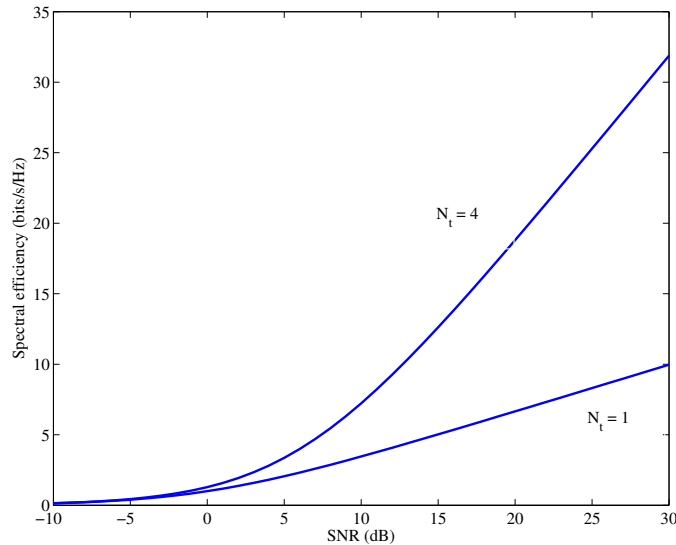


Figure 2.1: Spectral efficiency according to Shannon's formula for serial ($N_t = 1$ stream) and parallel ($N_t = 4$ streams) data transmission versus the SNR [38].

transmission of N_t streams. With parallel data transmission, the spectrum is reused in the *spatial* domain, which increases the spectral efficiency significantly.

Figure 2.2 shows how MIMO techniques can be realized in a radio link. First, data is split into multiple parallel streams, which are then transmitted over the wireless channel. There will be unavoidable cross-talk between the data streams, which needs to be eliminated by using e.g. multiple antennas at the receiver. In this way, the data streams can be separated by signal processing based on the knowledge of the complete MIMO channel matrix. Therefore, the channels between each antenna element at the transmitter and each antenna element at the receiver need to be estimated. In general, the way to realize MIMO gains is to use multiple antennas both at the transmitter or/and the receiver, in combination with signal processing for demultiplexing the parallel streams. In this way, spatial multiplexing of multiple streams increases the capacity of the wireless channel.

The influence of the wireless channel on the MIMO performance is of great interest. The most important tool for analyzing the structure of the MIMO channel is the singular value decomposition (SVD), which has been initially introduced by Eckart and Young in [42]. Using the SVD of the channel matrix enables a parallel transmission over a diagonalized MIMO channel. Following the analysis as provided in [38], it can be shown that the number of parallel data streams, which can be transmitted over a channel matrix with full rank, scales with $\min(N_t, N_r)$, where N_r denotes the number of receive antennas. It is also straightforward to show that the achievable SNR for the i^{th} data stream is related to the corresponding singular value by $\text{SNR}_i = \frac{\sigma_i^2}{\sigma_n^2}$ where σ_n^2 denotes the mean AWGN power

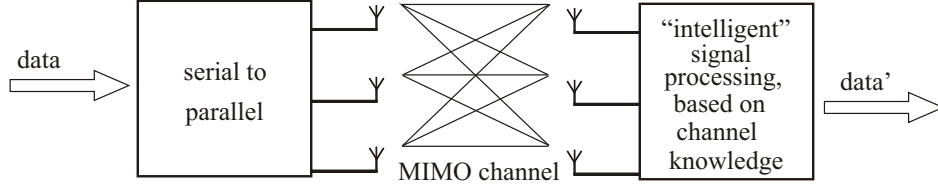


Figure 2.2: Principle of a parallel data transmission in a MIMO system. Here, signal processing at the receiver is used for separating the multiple data streams [38].

at the receiver. Note that these singular values σ_i^2 are equal to the square roots of the non-zero Eigenvalues λ_i , and that the channel matrix has at most $\min(N_t, N_r)$ singular values. As seen by the SNR expression, the SVD also provides a quality criterion for the data transmission on each of the parallel streams.

Fundamental research has been conducted for determining the achievable capacity in MIMO systems and how this depends on the channel properties by Foschini and Gans [34] and Telatar [35]. The general form of the capacity formula for a flat-fading MIMO channel has been derived in [35], which, however, includes the transmit covariance matrix as a parameter. In [34], it was shown that for the case that the transmitter is unaware of information about the channel state information, it is favorable to distribute the transmit power P_{Tx} equally across data streams. In this case, the transmit covariance matrix becomes equal to $\frac{P_{Tx}}{\sigma_n^2} \cdot \mathbf{I}$ and the capacity of the MIMO channel reaches

$$C_{\text{MIMO}} = \log_2 \left(\left| \mathbf{I} + \frac{P_{Tx}}{N_t \cdot \sigma_n^2} \mathbf{H} \mathbf{H}^H \right| \right). \quad (2.3)$$

This result is practically the same with the one derived in [34], except the channel normalization, which is described in what follows. First, the receive antennas are assumed to be placed in the same field, in order to have a fair comparison with single antenna links. This results into an equal mean SNR condition for all receivers. For a $N_r \times N_t$ channel matrix \mathbf{H} with mean path gain given by $\eta_{\mathbf{H}} = \frac{1}{N_r \cdot N_t} \cdot \text{tr}(\mathbf{H} \mathbf{H}^H)$, the following well-known MIMO capacity formula is then obtained

$$C_{\text{MIMO}} = \log_2 \left(\left| \mathbf{I} + \frac{\text{SNR}}{N_t \cdot \eta_{\mathbf{H}}} \mathbf{H} \mathbf{H}^H \right| \right). \quad (2.4)$$

Here, the SNR is measured at one of the receive antennas. Foschini and Gans originally assumed that the mean path gain is equal to one for all links, i.e. $\eta_{\mathbf{H}} = 1$. However, when different, e.g. for measured channels, the mean power of the entries of matrix $\mathbf{H} \mathbf{H}^H$ needs to be normalized to unity by dividing with $\eta_{\mathbf{H}}$, before (2.4) can be compared to theoretical results.

MIMO concepts

Here, some practical aspects on MIMO are given, related to the channel knowledge. A way to classify MIMO concepts is according to where channel state information (CSI) is available: at the receiver, at the transmitter and at both ends of the link. The main practical applications and corresponding enabling precoding and decoding techniques are briefly mentioned for each of the three schemes. Additional information on these techniques can be also found in [38].

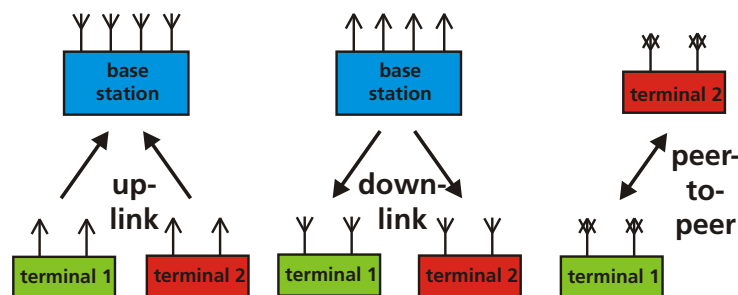


Figure 2.3: Application of MIMO concepts, as given in [38]: *Left*: CSI at the receiver is useful for the uplink. *Center*: CSI at the transmitter is useful in the downlink. *Right*: CSI at both ends is useful for peer-to-peer links.

CSI at the receiver: For MIMO with CSI at the receiver, applications can be found in any single-link MIMO system as well as in cellular uplink scenarios, where multiple users can be considered as a virtual MIMO array. Users are jointly detected at a multi-antenna base station, see Figure 2.3, left. There are simple linear processing schemes such as zero-forcing (ZF), minimum mean square error (MMSE) and maximum ratio combining (MRC), iterative schemes such as ordered successive interference cancellation, also known as Vertical Bell Labs Space-Time (V-BLAST) detection, which is also considered as a fair trade-off between performance and complexity [43]. Finally, maximum-likelihood (ML) detection is known as the most complex and best performing detector with CSI at the receiver.

CSI at the transmitter: Schemes with CSI at the transmitter are very important for the downlink in mobile networks, see Figure 2.3 center, which is typically carrying most of the traffic. Moreover, such schemes are important, because they apply to distributed MIMO architectures, where antennas of base stations can be considered as inputs and distributed mobile terminal antennas as outputs of a distributed MIMO system. Here, there are simple precoding schemes such as ZF and MMSE, as well as sophisticated schemes such as Tomlinson-Harashima precoding (THP) and lattice-based precoding [44]. According to theory, the optimal scheme is dirty paper coding [45], which all schemes mentioned before try to approximate. Meanwhile, there have been provided important results in

information theory and signal processing e.g. [46], where an optimal strategy for the two user case has been developed. Uplink and downlink duality has been elaborated in [47] and [48]. Practical techniques for mobile users with multiple antennas based on ZF and block-diagonalization have been considered in [49]. An interesting observation has been also made in [50], where, while multiple users are served in parallel, it is close-to-optimal to send not more than one data stream to each user.

CSI at both sides: For MIMO with CSI at both sides, applications can be found in peer-to-peer links such wireless local area networks (WLANs), see Figure 2.3, right. Such MIMO schemes can be realized by means of channel reciprocity or over a feedback link. In a single-user MIMO link, CSI at both sides enables the basic SVD-based MIMO transmission scheme. More SVD-based robust schemes can be also found in [51]. For multi-user MIMO, the situation is more complex and very similar to the case where CSI is available only at the transmitter. A major difference occurs when there are multiple antennas at the terminal side, as they can be used to remove residual intra-cell interference between multiple streams sent to a single terminal [49]. The use of receive antennas for interference reduction is also obvious. Spatial degrees of freedom at the terminal side, which are not used to detect the data streams, can be used to cancel inter-user interference caused e.g. by mismatched precoding or even out-of-cluster interference in the case of distributed MIMO with coordinated base stations.

2.1.2 Coordinated multi-point (CoMP)

As shown in Section 2.1.1, MIMO increases significantly the spectral efficiency in wireless networks, compared to traditional single-antenna techniques. While serving multiple users on the same time and frequency resource, considering multi-cellular networks, there will be still substantial interference between the cells limiting the overall performance.

Base station cooperation, also known as *Network MIMO* or *CoMP*, is envisioned as a promising technique for future cellular networks, where frequencies shall be fully reused. CoMP aims to reduce the interference between adjacent cells, to increase the spectral efficiency and to provide a more consistent performance, especially for users close to the cell edge.

CoMP is the most ambitious form of MIMO conceived so far. Here, antennas of multiple distributed base stations and those of multiple terminals served within those cells are considered as a distributed MIMO system [36, 52, 53]. Similar to non-distributed MIMO, CoMP relies on the fact that spatial multiplexing of multiple data streams is possible, if information about the MIMO channel is provided and used for joint signal processing, at least at one side of the MIMO link [54]. In the downlink, signal pre-processing at the base stations is used to eliminate the inter-cell interference and to enhance the system capacity. By synchronizing the base stations and enabling data and CSI exchange over the backhaul network, the multi-cellular network is able to transmit jointly to all users so that the interference between the cells is eliminated. Figure 2.4 shows a joint transmission (JT)

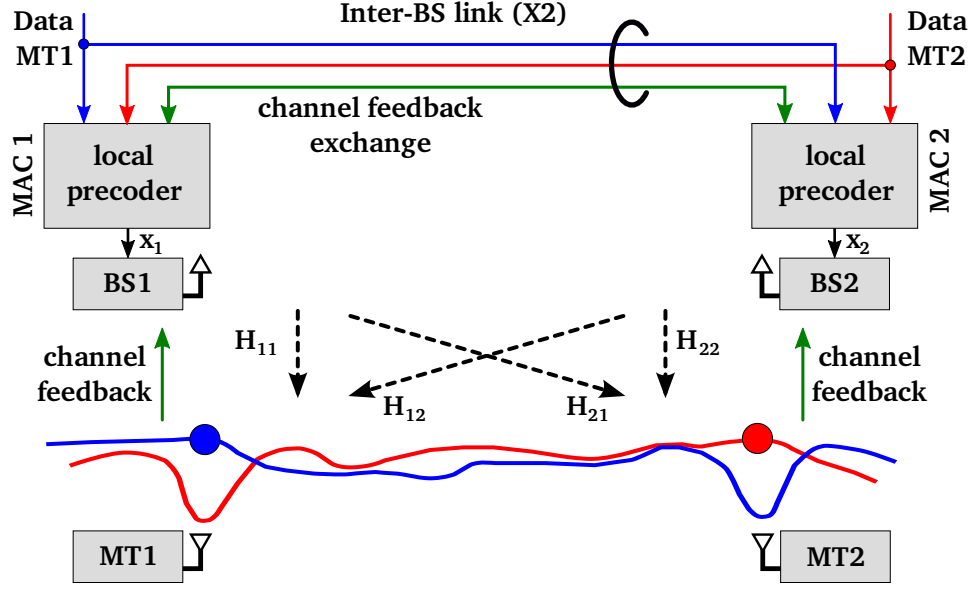


Figure 2.4: Distributed JT CoMP with two base stations and two terminals (FDD mode). Joint data precoding based on channel information feedback and synchronized base stations allow for inter-user interference-free data reception [38].

CoMP system with two base stations and two terminals, operating in the frequency division duplex (FDD) mode. Here, the network obtains channel information from the terminals over a feedback link, whereas CSI is also exchanged between distributed base stations over the backhaul network.

In the simplest case, data symbols are precoded with the pseudo-inverse of the MIMO channel matrix; this method is known as ZF precoding [49]. At the position of a mobile user, its own signal contributions received from multiple base stations overlap constructively, while signals dedicated to other users cancel. In this way, each user receives its own signal without interference from transmissions to other users. According to the results demonstrated in [55], in the high SNR regime, system performance becomes close to optimal when using ZF precoding.

We now consider a cellular network where N_b base stations (BSs) form a so-called *cooperation cluster* and serve jointly N_u mobile users on the same time and frequency resource, all equipped with single-antenna terminals. Through this work, N_u will denote the number of users that are served by a cooperation cluster on the same time and frequency resource and not the total number of users served in the cluster, when using multiple-access techniques. For distributed architectures, transmission is coordinated over a backhaul network, which enables fast data and CSI exchange between the BSs. Out-of-cluster transmission is not considered in our model and out-of-cluster interference is treated as noise.

The (narrow-band) channel matrix \mathbf{H} has size $N_u \times N_b$ and includes frequency-flat path loss and shadow fading as well as frequency-selective small-scale fading. For broad-

band orthogonal frequency division multiplexing (OFDM) transmission, \mathbf{H} denotes the frequency-domain representation of the MIMO channel matrix on a single subcarrier.

In the downlink of base-coordinated systems, also known as joint transmission coordinated multi-point (JT CoMP), data signals are precoded at the base stations. In the most simple case, known as ZF, the precoding matrix equals to the channel pseudo-inverse [56]. The $N_b \times N_u$ precoding matrix \mathbf{W} is calculated by the right-hand Moore-Penrose pseudo-inverse of the channel matrix \mathbf{H} , i.e. $\mathbf{W} = \mathbf{H}^H(\mathbf{H}\mathbf{H}^H)^{-1}$, which we assume that exists. The precoder is applied onto the $N_u \times 1$ data symbol vector \mathbf{s} and precoded data are transmitted jointly from all BSs over the MIMO channel. Considering AWGN \mathbf{n} with zero mean and variance σ_n^2 at the receivers, the downlink transmission can be described by

$$\mathbf{y} = \mathbf{H}\mathbf{W}\mathbf{s} + \mathbf{n} = \mathbf{s} + \mathbf{n}. \quad (2.5)$$

As observed by (2.6), transmission to multiple users is orthogonalized by ZF and each user receives its own signal, free of inter-user interference. It is known from [55] that in the high SNR regime, system performance becomes close to optimal, when using ZF precoding.

The number of users that can be served simultaneously by a so-called *cluster* of cooperating base stations without inter-user interference can be as high as the total number of transmit antennas that are available in the cluster. Of course, enabling the full-dimension of a CoMP cluster, and hence exploiting its full spectral efficiency, requires that all base stations cooperate by carrying out joint transmission (precoding) in the downlink and joint detection (decoding) in the uplink, of the signals to the group of jointly served users. Ideally, all interference is thereby removed and the performance is like in the absence of interference in an isolated cell [57].

Full cooperation is impractical because of the large amount of required feedback and signaling overhead. Note that overheads due to pilots required for multi-cell channel estimation, feedback information and information exchange over the backhaul scale roughly proportionally to the number of transmit antennas. For limiting the overhead, more practical methods consider interference as a spatially limited phenomenon, as it is mainly caused by the nearest base stations [58, 59] and apply therefore CoMP to a relatively small number of base stations. These observations lead intuitively to the concept of cooperative clusters, see e.g. [60–63].

Early field trials based on the Third Generation Partnership Project (3GPP) Long Term Evolution (LTE) have been conducted in several scenarios [37, 59, 64]. Recent progress on CoMP is reported in [65, 66]. In [67], concepts on JT CoMP deployment and recent field trials have been presented. An overview of cooperative communications can be also found in [68]. Due to its favorable features, CoMP has received considerable interest in recent research and has been already partly embodied in the LTE-A standard. In parallel, CoMP is discussed as a key technique for next generation (5G) cellular networks [87] and [69].

Although suitable for attaining high spectral efficiency, CoMP by itself is not enough for delivering the high data rates that modern mobile communications demand. The

MIMO technique has to be complemented with a modulation method that lends itself well for transmission over frequency selective channels. The preferred broadband modulation scheme today is OFDM. The technique divides the available bandwidth in a number of orthogonal subcarriers, where each of them observes frequency-flat fading and can be processed as a single-carrier transmission. The combination of spectrally efficient OFDM with MIMO and CoMP techniques is a successful concept for broadband cellular networks and has enabled significant increase of the system throughput compared to conventional narrowband single-input single-output (SISO) techniques [34,56]. OFDM is also a favorable scheme to manage the complexity of the required signal processing for MIMO and has been standardized in the 3GPP LTE [31].

2.2 Signal model for the impaired CoMP downlink

In this section, a multi-cellular multi-user signal model for the precoded downlink with impairments is presented. It is shown that impairments causing imperfect channel knowledge at the base stations and imperfect synchronization introduce a mismatch between the applied precoder and the channel faced by the downlink transmission, which generates interference among users. Here, general expressions are provided for the users' self-signal and the inter-user interference (IUI), which are valid for all categories of impairments investigated though the rest of this work.

In real-world systems, one has to cope with impairments that cause a mismatch between the precoder applied to the downlink signals and the radio channel over which the transmission is realized. A first category are the so-called *channel impairments*, which are generated as described in the following. In FDD systems, terminals estimate the channel and provide quantized CSI to the BSs, as shown in Figure 2.4. In time division duplex (TDD) systems, CSI used for downlink precoding is obtained by channel estimation performed at the BSs. In both cases, the base stations obtain channel estimates with thermal noise, interference and quantization contributing to their inaccuracy. In addition, there is a time delay, equal to the time interval from when the channel is observed until when the resulting estimate is used for precoding. This delay is mainly generated by the computational time, the transmission over the air and (for distributed architectures) by the CSI exchange between base stations over the backhaul network. These sources of delay add up to an overall delay, which will be from here on termed as *feedback delay*. Because of the channel time variance due to the users' mobility, the channel state information at the transmitter (CSIT) results to be outdated when used for the precoder calculation; this effect is also known as *channel aging*. This work considers a further category of impairments, called *synchronization impairments*. These are caused by the fact that distributed base stations and terminals within their cells are driven by their local oscillators and use their own references with individual carrier frequency offsets (CFOs) and sampling frequency offsets (SFOs). It is to be noted that experimental measurements obtained from our CoMP test network reveal

these critical weaknesses in practice. The outdoor test network has been developed at the Fraunhofer Heinrich Hertz Institute (HHI) in Berlin, Germany [59, 64] and supports CoMP transmission from three distributed sites, as also shown in Figure 2.5.

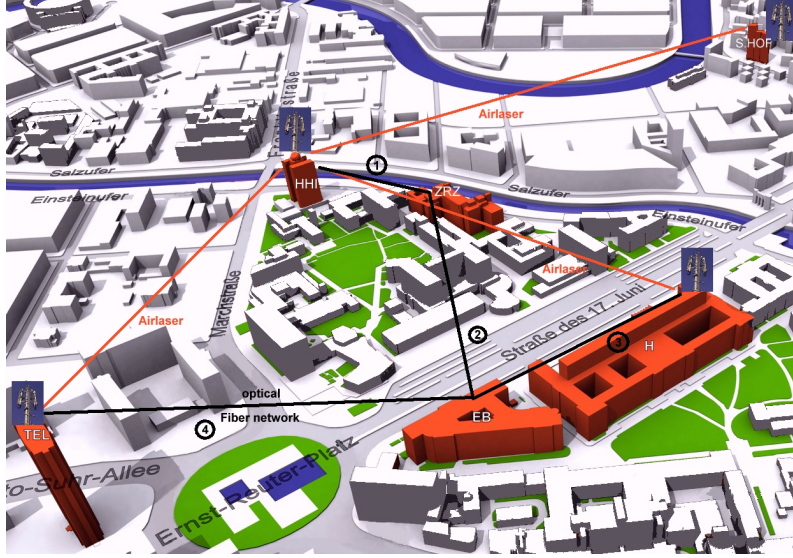


Figure 2.5: The multi-cell testbed of the Fraunhofer Heinrich Hertz Institute, located in the Technische Universität Berlin campus in the city center of Berlin, Germany.

Our next step is to include imperfect precoding due to impairments into the signal model given by (2.6). The channel and synchronization impairments responsible for imperfect CSIT are highlighted in Figure 2.6 for a point-to-point transmission in an FDD system. It can be assumed, and will be also shown in Chapter 4 and Chapter 5, that all impairments considered in this work can be modeled by an additive *equivalent channel error*. It is noted that receiver-side impairments are for now excluded from the model, as they do not have any additional effect in precoded transmission than in non-precoded transmission and do not cause IUI. Imperfect synchronization of mobile users and its influence on the performance of JT CoMP will be analyzed in Chapter 4.

Without loss of generality, we define $t = 0$ as the time instant when the channel is estimated and quantized. During the feedback delay, the mobile radio channel evolves and the CSIT becomes outdated for precoding the downlink transmission at a later time instant $t > 0$. During the same time, phase drifts due to oscillator misalignments are accumulating and affect the channel as seen by the precoded data, effect which can be mathematically described by an equivalent channel error. In a real system, the effect of channel time variance and imperfect synchronization takes place after the application of the precoder, which, however, is calculated based on channel estimates obtained at $t = 0$. From a signal modeling point of view, however, it is allowed and leads to a very similar result, to assume a perfectly matched precoder with the channel at time $t = 0$ and consider

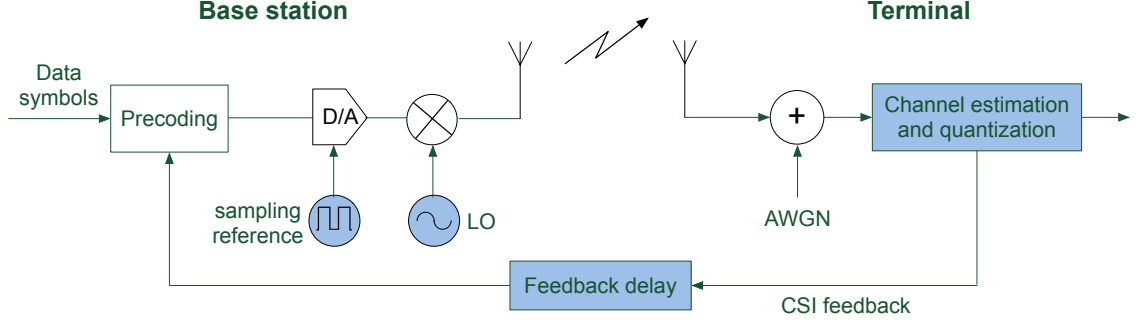


Figure 2.6: Sources of mismatched precoding in FDD systems: channel estimation at the terminal and CSI feedback quantization, channel aging during the feedback delay and imperfect sampling and carrier frequencies at the base station.

channel estimation and quantization errors, together with channel evolution, as part of the channel faced by data transmission at later time instants.

Considering all the above, the precoder mismatch is described by an equivalent channel error Δ , capturing the effect due to any of the impairments. In our model, the precoder \mathbf{W} is calculated from channel \mathbf{H} , while data are transmitted over channel $\tilde{\mathbf{H}} = \mathbf{H} + \Delta$. The downlink equation becomes

$$\mathbf{y} = \tilde{\mathbf{H}}\mathbf{W}\mathbf{s} + \mathbf{n} = \mathbf{s} + \Delta\mathbf{W}\mathbf{s} + \mathbf{n}, \quad (2.6)$$

indicating that matrix Δ breaks the inverse relation between the precoder and the channel and causes IUI among transmissions to multiple users. We now single out an arbitrary user j and separate its own signal (self-signal) from the signal of the other users. The self-signal contains the data transmitted to the particular user and can be detected if the channels reaching the user are estimated and equalized. Therefore, it will be considered as a useful signal though this work. In order that IUI is present in our model, at least two mobile users must be simultaneously served on a frequency resource, i.e. $N_u \geq 2$. Under those conditions, the user j receives

$$y_j = \underbrace{s_j \left(1 + \sum_{b=1}^{N_b} \delta_{jb} w_{bj} \right)}_{\text{self-signal}} + \underbrace{\sum_{\substack{u=1 \\ u \neq j}}^{N_u} s_u \sum_{b=1}^{N_b} \delta_{jb} w_{bu}}_{\text{inter-user interference}} + n_j, \quad j = 1, \dots, N_u. \quad (2.7)$$

Here, s_u , δ_{jb} , w_{bu} and n_j are entries of matrices \mathbf{s} , Δ , \mathbf{W} and \mathbf{n} , respectively.

Expression (2.7) provides a simple model, which allows for taking first insights into the role of impairments and system parameters on the signal and interference. In Chapter 4 and Chapter 5, the model will be further specialized and mathematical expressions will be provided for those terms for each single impairment.

2.3 Analysis of signal and interference power

In this section, we analyze the mean power of a user's self-signal and IUI, as provided by expression (2.7). For channel estimation and quantization errors, statistical independence between matrices $\mathbf{\Delta}$ and \mathbf{H} , and thus between $\mathbf{\Delta}$ and \mathbf{W} , is evident. For a time-varying channel, it is known from [70] that the channel referring to a later time instant can be analyzed into two additive terms, the one of which (channel error) is AWGN-like and statistically independent of the channel at the previous time instant \mathbf{H} . For time and frequency synchronization errors it is also shown in Section 4.5, that for relatively small carrier and sampling frequency offsets, $\mathbf{\Delta}$ can be very well approximated by a zero-mean term, which is also statistically independent of \mathbf{H} . Hence, it will be from now on assumed that entries of \mathbf{H} and $\mathbf{\Delta}$ are statistically independent of each other.

As the equivalent channel error has zero mean value $\mathbb{E}\{\delta_{jb}\} = 0$, we have $\mathbb{E}\{\delta_{jb}s_u^*\} = 0$ and $\mathbb{E}\{\delta_{jb}w_{bu}^*\} = 0$. As s_u are also zero-mean and statistically independent of the channel, it holds $\mathbb{E}\{s_u w_{bu}^*\} = 0$. The mean symbol energy equals to $\mathbb{E}\{|s_u|^2\} = E_s$. The mean power of the channel error δ_{jb} of mobile user j to all serving BSs is given by $\mathbb{E}\{|\delta_{jb}|^2\} = \sigma_{\delta,j}^2$. Considering all above, the mean power of self-user signal (\bar{s}_j) and IUI (\bar{s}_j) defined in (2.7) yield

$$\mathbb{E}\{|\bar{s}_j|^2\} = E_s \cdot \left(1 + \sigma_{\delta,j}^2 \cdot \sum_{b=1}^{N_b} \mathbb{E}\{|w_{bj}|^2\}\right) \quad (2.8)$$

$$\mathbb{E}\{|\bar{s}_j|^2\} = E_s \cdot \sigma_{\delta,j}^2 \cdot \sum_{\substack{u=1 \\ u \neq j}}^{N_u} \sum_{b=1}^{N_b} \mathbb{E}\{|w_{bu}|^2\} \quad (2.9)$$

The above expressions require that at least two mobile users are present, otherwise IUI is zero.

The sum-term appearing at the right-hand side of (2.8) and (2.9) can be written as

$$\sum_{b=1}^{N_b} \mathbb{E}\{|w_{bu}|^2\} = \mathbb{E}\{(\mathbf{W}^H \mathbf{W})_{uu}\} = \mathbb{E}\{\lambda_u^{-1}\}, \quad \forall u \in \{1, \dots, N_u\}, \quad (2.10)$$

where λ_u denotes the u^{th} eigenvalue of matrix $\mathbf{H}\mathbf{H}^H$ and $(\cdot)_{uu}$ denotes the on-diagonal element found in row u and column u of matrix $\mathbf{W}^H \mathbf{W}$. It is noted that the mean value of the inverse eigenvalue given in (2.10) does not depend on the particular index $u \in \{1, \dots, N_u\}$, as the eigenvalues are randomly sorted.

The average of the eigenvalue λ_u , as well as the average of its inverse, depend on the channel properties. We will first analyze (2.10) for a MIMO channel with complex Gaussian $\mathcal{CN}(0, \sigma_h^2)$ independent and identically distributed (i.i.d.) entries (Rayleigh fading channel). It has been shown in [71] that for $N_b > N_u$, the matrix $\mathbf{W}^H \mathbf{W} = (\mathbf{H}\mathbf{H}^H)^{-1}$ follows a complex inverse Wishart distribution ($\mathbf{H}\mathbf{H}^H$ is complex Wishart distributed) with N_b

degrees of freedom, denoted by

$$(\mathbf{H}\mathbf{H}^H)^{-1} \sim \mathbb{W}_{N_u}^{C^{-1}}(N_b, \mathbf{\Sigma}^{-1}), \quad N_b > N_u. \quad (2.11)$$

Here, $\mathbf{\Sigma}^{-1}$ denotes the inverse of covariance matrix $\mathbf{\Sigma}$ of the channel \mathbf{H} , which we assume that exists.

For the Rayleigh fading channel, which has been described in Appendix 1.4, the average of the eigenvalues as well as of their inverse, have been derived analytically in [72]. The proof using the channel eigenvalues is given in Appendix 7.1.1 and Appendix 7.1.2, see final expressions (7.8) and (7.13), respectively. There, it has been shown that

$$\mathbb{E} \left\{ \frac{1}{\lambda_u} \right\} = \frac{1}{\sigma_h^2(N_b - N_u)}, \quad N_b > N_u. \quad (2.12)$$

We note that a similar mathematical result can be found in [73].

Before reaching our first analytical result, we define the mean signal-to-interference ratio (SIR) of a user j as the ratio of mean power of useful signal to inter-user interference:

$$\text{SIR}_j = \frac{\mathbb{E} \{ |\check{s}_j|^2 \}}{\mathbb{E} \{ |\bar{s}_j|^2 \}}, \quad N_b > N_u \geq 2. \quad (2.13)$$

Imposing the inverse eigenvalue (2.12) into (2.10) and taking the ratio between (2.8) and (2.9) as in (2.13), we reach

$$\text{SIR}_{j,\text{Rayleigh}} = \frac{1}{\text{MSE}_j} \cdot \frac{N_b - N_u}{N_u - 1} + \frac{1}{N_u - 1}, \quad N_b > N_u \geq 2. \quad (2.14)$$

The ratio $\sigma_{\delta,j}^2/\sigma_h^2 = \text{MSE}_j$ is a measure of the imperfect knowledge which the BSs have about the multi-cell channel of user j , normalized to the mean channel power σ_h^2 . It is noted that in our model the mean power of the channel used for data transmission is $\sigma_{h,j}^2 = \sigma_h^2 + \sigma_{\delta,j}^2$. For an ideal case with perfect channel knowledge, i.e. $\text{MSE} \rightarrow 0$, a scenario with interference-free transmission and thus infinite mean SIR would be approached.

In the context of ZF precoding, a channel matrix with orthogonal rows (users' channel vectors) of equal power can be understood as a best case scenario and has been also investigated as such in [55]. We can write

$$\sum_{u=1}^{N_u} \lambda_u = \text{tr}(\mathbf{H}\mathbf{H}^H) = \sum_{u=1}^{N_u} \sum_{b=1}^{N_b} |h_{ub}|^2 = \sigma_h^2 N_u N_b. \quad (2.15)$$

As all eigenvalues are equal with each other, it is straightforward that

$$\lambda_u = \sigma_h^2 N_b, \quad \forall u \in \{1, \dots, N_u\}. \quad (2.16)$$

Using (2.16) in (2.10) and taking the ratio between (2.8) and (2.9), we reach

$$\text{SIR}_{j,\max} = \frac{1}{\text{MSE}_j} \cdot \frac{N_b}{N_u - 1} + \frac{1}{N_u - 1}, \quad N_u \geq 2. \quad (2.17)$$

Expressions (2.14) and (2.17) are important results. They reveal that the mean SIR, which a single-antenna terminal reaches with ZF precoding, is inversely proportional to the normalized mean square error (MSE) and further grows with the number of base stations and drops with the number of users. This rule holds for the Rayleigh fading channel as well as for the ZF upper bound.

More critically, for the Rayleigh fading channel the mean SIR is not defined if $N_u = N_b$, as it can be seen (2.12). In this specific case, which has also been studied in our experiments [64], the system performance becomes particularly sensitive against imperfect channel knowledge. The critical sensitivity against impairments is related to those particular cases in the channel statistics where the multi-user multi-cell channel matrix \mathbf{H} is close to singular, i.e. where the channel vectors are by accident almost parallel.

From a system design perspective, when using ZF precoding, a scheduler should combine the users in a cooperation cluster in sets whose channel vectors are nearly orthogonal, so that singularities of the channel matrix \mathbf{H} are avoided up front. It is known from information theory that in the high SNR regime, the multi-user multi-antenna system performance becomes close to optimal despite using the simple ZF precoder [55]. What we learn here in addition is that, in the same way, the system becomes more stable against imperfect channel knowledge.

We now refer again to the case where \mathbf{H} follows a complex Gaussian distribution, hence matrix $\mathbf{W}^H \mathbf{W} = (\mathbf{H} \mathbf{H}^H)^{-1}$ is complex inverse Wishart distributed. In [74], it is stated that the mean value of any of its on-diagonal elements is given by

$$\mathbb{E} \{ (\mathbf{W}^H \mathbf{W})_{uu} \} = \sum_{b=1}^{N_b} \mathbb{E} \{ |w_{bu}|^2 \} = \frac{1}{\sigma_h^2 (N_b - N_u)}, \quad N_b > N_u. \quad (2.18)$$

It is noted that using (2.18) in (2.10) leads to the same result for the mean useful signal and inter-user interference as (2.8) and (2.9).

The fact that the mean SIR is inversely proportional to the MSE, as observed by (2.14) and (2.17) motivates for analyzing further the MSE for each impairment separately, which is done in Chapter 4 and Chapter 5. There, analytical expressions including parameters such as the CFO and SFO variance, the feedback delay, the users' mobility, the channel estimation error power etc. are derived. Such MSE expressions are not only useful for analyzing the SIR in JT CoMP, but can be also used as interfaces for realistic link-layer abstraction as well as performance evaluation on system level. Figure 2.7 shows how MSE modeling can be integrated as an intermediate step between exact signal modeling and various system procedures.

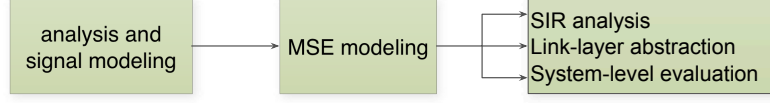


Figure 2.7: Based on analysis and signal modeling, impairments can be captured by their MSE, vital for SIR analysis, link-layer abstraction and system-level evaluation.

2.4 Transmit power in JT CoMP systems

The $N_b \times 1$ signal vector transmitted from all BSs to all mobile users is given by

$$\mathbf{x} = \mathbf{W}\mathbf{s}, \quad \text{with entries} \quad x_b = \sum_{u=1}^{N_u} w_{bu}s_u. \quad (2.19)$$

Considering the statistical independence between data symbols and precoder entries, the average of the total transmit power is given by

$$P_t = \mathbb{E} \left\{ \sum_{b=1}^{N_b} \sum_{u=1}^{N_u} |w_{bu}|^2 |s_u|^2 \right\} = E_s \cdot \mathbb{E} \left\{ \sum_{b=1}^{N_b} \sum_{u=1}^{N_u} |w_{bu}|^2 \right\}. \quad (2.20)$$

Using property (2.10), we can develop (2.20) as

$$P_t = E_s \cdot \sum_{u=1}^{N_u} \left(\sum_{b=1}^{N_b} \mathbb{E} \{ |w_{bu}|^2 \} \right) = E_s \cdot N_u \cdot \mathbb{E} \{ \lambda_u^{-1} \}, \quad \forall u \in \{1, \dots, N_u\}, \quad (2.21)$$

which shows that the mean total transmit power P_t is proportional to the mean of the inverse eigenvalues.

For a channel matrix with orthogonal rows, i.e. users' channel vectors, of equal power, the required transmit power is minimized. Using (2.16) in (2.21), we reach

$$P_{t,\min} = E_s \cdot \frac{N_u}{\sigma_h^2 N_b}. \quad (2.22)$$

For the Rayleigh fading channel we use (2.12) in (2.21) and obtain

$$P_{t,\text{Rayleigh}} = E_s \cdot \frac{N_u}{\sigma_h^2 (N_b - N_u)}, \quad N_b > N_u \geq 2. \quad (2.23)$$

From (2.23) we see that for $N_u \rightarrow N_b$ the mean transmit power approaches infinity asymptotically. Practically this means that, in order to serve all users through ZF, the BSs need to spend on average an infinite amount of power. This infinite value comes from the cases where the cooperation cluster includes users with nearly orthogonal channel vectors, which should be in a practical system avoided by a scheduler. To deal with these

problems, next to an efficient clustering mechanism, a power constraint per antenna and/or per mobile user should be considered for practical systems.

2.5 Evaluation of downlink SIR

We consider a ring of $N_b = 7$ BSs transmitting jointly to N_u terminals ($2 \leq N_u \leq 6$) with ZF precoding. An OFDM system spanning $N_s = 2048$ subcarriers is used, on which i.i.d. data symbols with mean energy of $E_s = 1$ are modulated. Figure 2.8 depicts the SIR, both analytically and numerically evaluated. The channel error on each subcarrier is modeled as i.i.d. complex Gaussian with zero mean and variance according to the MSE. The normalized MSE is set to -35 dB, -25 dB and -15 dB. The SIR is evaluated according to (2.14) and (2.17). For the case of Rayleigh fading channel, elements of the channel matrix \mathbf{H} on each OFDM subcarrier are modeled as i.i.d. complex Gaussian random variables with zero mean and variance $\sigma_h^2 = 1$. Numerical evaluation of the mean SIR is performed over 500 independent broadband Rayleigh channel realizations.

As observed, numerical evaluation (for the Rayleigh fading channel) fully agrees with our analytical results. Increasing the MSE by one order of magnitude decreases the SIR values by 10 dB. The distance between the maximum and the SIR in Rayleigh fading grows with the number of users, clarifying the value of user selection for systems with more users.

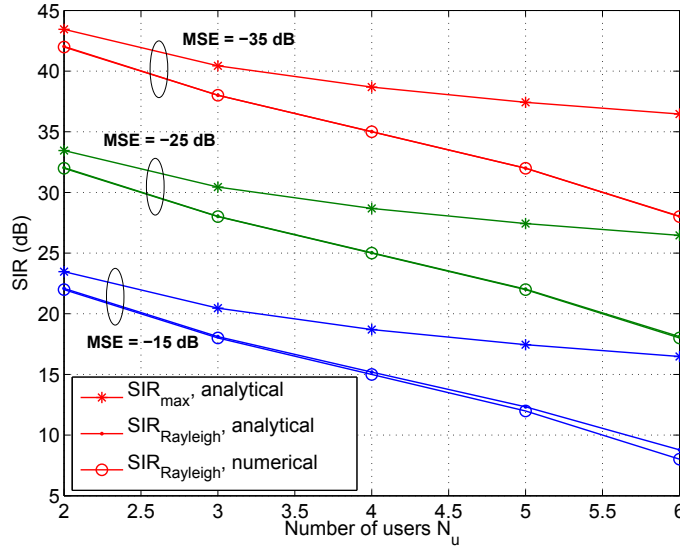


Figure 2.8: Mean SIR upper bound (2.17) (analytical) and for Rayleigh fading channel (2.14) (analytical and numerical). $N_b = 7$ BSs jointly serve N_u users with zero-forcing, normalized MSE is set to -35 dB, -25 dB and -15 dB.

In broadband OFDM systems, the short-term SIR (SIR per subcarrier) has an important role, as it affects the achievable bit error rate (BER) and also guides adaptive modulation and power allocation. Here, we consider the SIR at the receiver input, which is lower than the SNR after data detection. Figure 2.9 depicts the cumulative distribution function (CDF) of the short-term SIR for the Rayleigh fading channel, evaluated per OFDM subcarrier and channel realization for $N_b = 7$ BSs serving $N_u = \{3; 6\}$ terminals, for a normalized MSE of -35 dB, -25 dB and -15 dB. It can be observed that increasing the MSE by one order of magnitude decreases the SIR statistics by 10 dB. The dependence of the SIR on N_b and N_u is also clear. From Figure 2.9, we can say that (2.14) represents the behavior not only of the average SIR, but also of the distribution of the SIR per OFDM subcarrier.

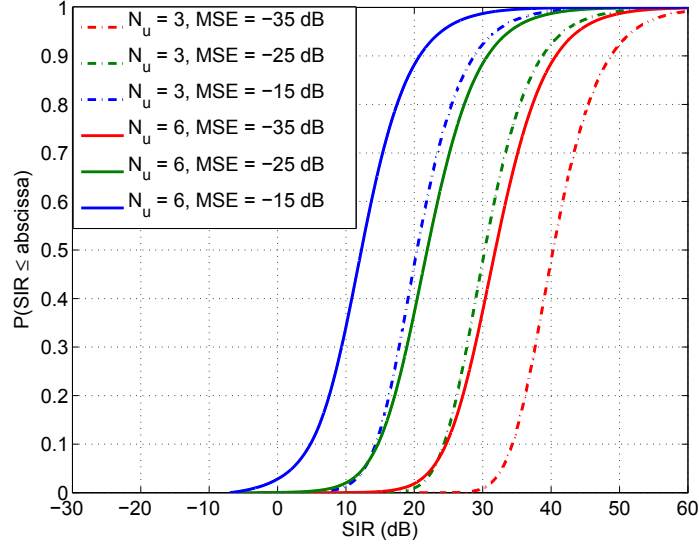


Figure 2.9: Statistics of SIR measured per OFDM subcarrier for $N_b = 7$ BSs serving $N_u = \{3; 6\}$ terminals in Rayleigh fading channel and for different MSE values.

2.6 Summary of Chapter 2

At the beginning of this chapter, background knowledge on MIMO, CoMP and OFDM was provided, which will be needed through the rest of this work. Afterwards, the JT CoMP system model was described and a signal model with an imperfect precoder was derived. The precoder mismatch with respect to the channel was captured by an additive equivalent channel error, which can be due to any of the impairments. Based on the signal model, the power of the users' self-signal and inter-user interference was analyzed and closed-form expressions were derived for the mean SIR, both for the Rayleigh fading channel as well

as for the SIR upper bound. It was shown that for zero-forcing precoding, the mean SIR is inversely proportional to the channel MSE, and that it grows with the number of base stations and drops with the number of jointly served users. Furthermore, it was shown that appropriate user selection can improve robustness against imperfect precoding and enhance the SIR. In practical systems, a scheduler should combine the users in a cooperation cluster in sets whose channel vectors are nearly orthogonal. In this way, transmission becomes more stable against impairments and performance becomes close to optimal despite for simple zero-forcing precoding. Clustering and using power constraints are also important, so that the total transmit power level remains practical.

3 Inter-site-distance limitations for CoMP

In this chapter, we investigate on the maximum allowed inter-site distance (ISD) for performing joint transmission coordinated multi-point (JT CoMP) between macro-cell base stations. As a key metric, we use the excess delay measured at the 95% point of the cumulative power delay profile (PDP) resulting from transmission of multiple base stations. As propagation distances in JT CoMP are typically larger than in single-cell transmission, distant-dependant channel modeling is essential. Therefore, we consider Greenstein's statistical propagation model [75], which we here extend for broadband multi-cell transmissions. We extract all model parameters from 2.65 GHz multi-cell measurements performed in outdoor field trial, parametrize the model at a fixed ISD and validate it by simulations. We also investigate the impact of antenna downtilt and find that when a larger downtilt is used, the root mean square (RMS) delay spread and 95% excess delay become smaller. Then, we consider larger ISDs and indicate how the delay parameters grow. It is found that, based on the extended Greenstein's model, the short cyclic prefix in Long Term Evolution – Advanced (LTE-A) is hardly violated for realistic ISD at 2.65 GHz.

Previous related work and objectives

The dependence of channel delay spread from the path gain and thus the propagation distance has been addressed in previous works on channel modeling. In [76], it has been found that in urban scenarios, the delay spread as well as its standard deviation increase with the distance and with deep shadow fading. An overview of the state of the art in cooperative multiple-input multiple-output (MIMO) channel modeling can be also found in [77].

In this chapter, we investigate the impact of base station (BS) cooperation on the overall delay statistics in a realistic deployment scenario. We seek an answer to the question what distance is allowed between cooperative base stations without violating a given cyclic prefix (CP). As a starting point, we use a distance-dependent statistical propagation model in [75], which describes also the correlation between path gain and delay spread. We parametrize this model based on coherent multi-cell channel measurements from the LTE-A field trial in Berlin, Germany [78–80]. Therefore, we extract the distance dependencies of path loss, shadow fading and delay spread as well as their correlation at a carrier frequency of 2.65 GHz in an urban macro-cell scenario.

We prove that Greenstein's model predicts the delay statistics properly at least at larger distances from the BS. Close to the BS, however, we observe 3D effects, leading to signif-

icant deviations from the predicted statistics if the downtilt is set so that the main beam touches the ground at 0.9 times the ISD. With a downtilt of 0.33 times the ISD, as recommended by Third Generation Partnership Project (3GPP) for LTE-A (see [81]), the overall delay statistics is mostly due to the overlap region covered jointly between adjacent sites, where Greenstein's model is more appropriate. Thus we can increase the ISD and predict the delay statistics by using our parametrized propagation model. Our results indicate that BS cooperation is feasible for distances up to 1.7 km between the sites at 2.65 GHz without violating the short CP in LTE-A.

The rest of this chapter is organized as follows. In Section 3.1, the problem of inter-symbol interference (ISI) in JT CoMP using orthogonal frequency division multiplexing (OFDM) is briefly described. Section 3.2 reviews Greenstein's model and extends it for broadband multi-cell transmissions. In Section 3.3, our measurement setup and the parameter extraction routines are described. Section 3.4 presents the extracted parameters and discusses the scope of the model by comparing prediction and measurement results. Furthermore, the parametrized model is used for predicting the delay statistics in larger cells. Finally, conclusions are discussed in Section 3.5.

3.1 Inter-symbol-interference in JT CoMP using OFDM

It is known that OFDM is well-suited for transmission over frequency-selective channels, as it divides the available bandwidth in a number of orthogonal sub-channels, where each of them observes frequency-flat channel fading and can be processed separately. However, the CP needed for subcarrier based equalization reduces the spectrum efficiency. It is therefore chosen longer than the largest multipath delay in the targeted propagation environment, in order to avoid ISI due to the channel echoes of the previously transmitted OFDM symbol. Figure 3.1 shows how the CP protects the transmission from ISI between consecutive OFDM symbols.

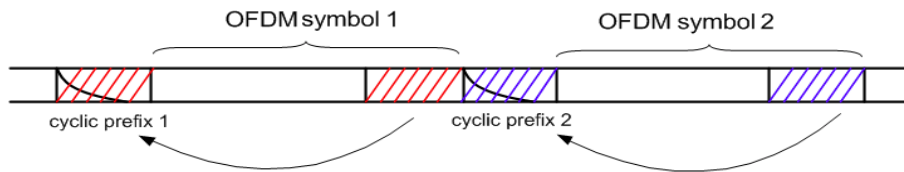


Figure 3.1: The cyclic prefix "absorbs" multipath echoes from the previous OFDM symbol and protects from inter-symbol interference. It also relaxes time synchronization requirements.

In practical systems, the beginning of the OFDM symbol is one of the first parameters a terminal needs to estimate in order to establish data exchange with a base station. Accurate time synchronization allows for removing correctly the CP and applying the fast

Fourier transform (FFT). For point-to-point OFDM systems, time synchronization has been studied thoroughly within the previous years. The mostly recognized, i.e. efficient and easily implementable methods suggest to transmit a periodic time-domain signal [82] or to exploit the periodicity of the cyclic prefix [83] and perform an autocorrelation of the received signal at the receiver. Then, a maximum in the estimator output points to the beginning of OFDM symbol. In order to allow for ISI-free transmission, the estimator needs to point into the CP part, which is free from the multi-path echoes of the previous OFDM symbol.

Considering now coordinated transmission from distributed base stations, there will be channel paths reaching a terminal from multiple transmission points that are less or more far away and thus with larger delays than in a point-to-point transmission. In a practical system, time synchronization and CP removal shall be performed with respect to the strongest received signal. However, the additional contributions to the overall delay statistics from multiple transmission points might violate the CP length and generate ISI between successive OFDM symbols. Vice versa, if the CP length would be increased, the spectral efficiency is reduced. It is thus evident that the existence of long multi-cell channel delay spreads imposes not only a tradeoff between the maximum allowed ISD and the required CP, but also reduces the margin for ISI-free data reception and establishes a challenge for time synchronization. The statistical properties of the multi-cell channel and the resulting ISD limitations for JT CoMP, from where also synchronization requirements are obtained, are investigated in what follows.

3.2 Modeling of the multi-cell broadband radio channel

Greenstein et. al in [75] state three fundamental conjectures about the channel delay spread of a single-link narrow-band channel:

- The RMS delay spread is log-normal at any distance
- It's median value increases with the distance
- The delay spread tends to grow in deep shadow fading

The last conjecture is very important as it suggests that dispersion is larger in case of deep shadow fading, i.e. when the signal-to-noise ratio (SNR) is usually low. In [75], physical arguments that support these conjectures are explained and confirmed by the existing literature referenced therein. Finally, a mathematical model for the joint statistics of average path gain and RMS delay spread is proposed. Parameters are specified for various environments in [75].

According to the model, the path gain is given by:

$$g = G_1 d^{-\gamma} x , \quad (3.1)$$

where d is distance in kilometers, G_1 is the median value of path gain g at a reference distance of $d = 1$ km, γ is the path loss exponent (usually between 2.5 and 4) and x is a log-normal variate at distance d . Specifically, $X = 10 \log_{10}(x)$ is a Gaussian random variable with zero mean and a standard deviation σ_x .

The median value of the RMS delay spread τ_{RMS} increases according to distance with an exponential factor ϵ . The RMS delay spread at distance d is given by

$$\tau_{\text{RMS}} = T_1 d^\epsilon y, \quad (3.2)$$

where T_1 is the median value of τ_{RMS} at a reference distance $d = 1$ km, the exponent ϵ lies between 0.5 and 1.0, and y is a log-normal variable. Specifically, $Y = 10 \log_{10}(y)$ is a Gaussian random variable at distance d , with zero mean and a standard deviation σ_y .

The delay spread is correlated by a negative correlation coefficient with the shadow fading gain. This means that, if strong channel paths, which usually arrive at early time instants, are blocked by large objects (negative shadowing gain), τ_{RMS} is expected to grow. The correlation between g and τ_{RMS} is described by

$$\mathbb{E}\{XY\} = \rho \sigma_x \sigma_y. \quad (3.3)$$

Here, ρ is the correlation coefficient between the two Gaussian variables X and Y . According to the model, large τ_{RMS} are associated with smaller g values, ρ should thus be negative; a value of $\rho = -0.75$ has been proposed in [75] for all types of environments.

Multi-cell broadband channel model

The channel model of Greenstein has been initially developed for narrow-band radio channels, where the sampling time is in the same order of magnitude or even larger than τ_{RMS} . This assumption is not valid for broadband systems, where the sampling time is significantly shorter. Therefore, we need to consider the channel PDP. Our assumption is that the PDP follows an exponential decay, which is well accepted for cellular radio channels [84]. Consequently, the received power p at distance d can be expressed by multiplying the path gain g (includes shadow fading) with a unitary PDP (p_u) according to

$$p(d, t) = g \cdot p_u(\tau_{\text{RMS}}, t) = \frac{g}{\tau_{\text{RMS}}} \cdot e^{-\frac{t}{\tau_{\text{RMS}}}}, \quad (3.4)$$

where g and τ_{RMS} are random variates that depend on the distance d and are given by (3.1) to (3.3) and t denotes the time-delay domain. The PDP of the received signals that are radiated from N_t distributed transmit antennas is then expressed by the sum of the PDP of the single links:

$$P(d, t) = \sum_{i=1}^{N_t} p_i(d_i, t - t_i) = \sum_{i=1}^{N_t} \frac{g_i}{\tau_{\text{RMS},i}} \cdot e^{-\frac{t-t_i}{\tau_{\text{RMS},i}}}. \quad (3.5)$$

Without loss of generality, it is assumed that the first channel path from the nearest base station reaches the terminal at $t = 0$. The PDP of the i^{th} base station is then shifted by t_i according to their geographic distance to the terminal, i.e. $t_i = d_i/c$ (c denotes the speed of light).

3.3 Parameter extraction from multi-cell channel measurements

Measurement setup

Measured channel data have been used from a multi-cell testbed with three multi-sector sites, located in the city center of Berlin, Germany. These BSs are placed on top of the Fraunhofer Heinrich Hertz Institute (HHI), the main building of the Technische Universität Berlin (TUB) and the Telekom Innovation Laboratories (T-Labs) building, as shown in Figure 2.5. Detailed information on this system are also available in our publications [64, 79, 85]. A precise time reference is available using an advanced Global Positioning System (GPS) receiver at each site and the whole radio network is synchronized to the pulse per second (PPS) signal. In conjunction with JT CoMP experiments, so called channel state information (CSI) reference signals were defined to identify the channels to each of the BSs. Each BS is identified by a pilot comb in frequency domain and a cyclic shift is applied along the frequency axis by an integer number of subcarriers where the shift identifies the cell, as illustrated in Figure 3.2. For identifying multiple antennas in each cell, four consecutive OFDM symbols have been used, where another orthogonal sequence is transmitted for each antenna [24]. In this way, a distributed but fully phase-coherent channel sounder has been realized for up to 6 cells.

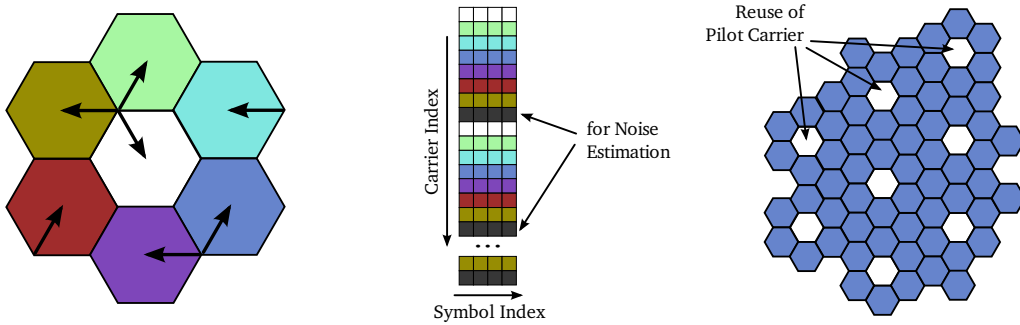


Figure 3.2: *Left*: Basic interference scenario. *Center*: Cells are identified using a frequency domain comb individually shifted in each cell. Antennas in the cell are identified by time-domain sequences. *Right*: Frequency reuse in cellular networks [38].

At the base stations, antennas from Kathrein with +18 dBi gain and two cross-polarized ports $\pm 45^\circ$ at the transmitter have been used. The downtilt for all BSs was first set such that the beam hits the ground at a distance of 450 m, which corresponds to 0.9 times the

ISD. In a second measurement, the downtilt was set so that the beam hit the ground at 0.33 times the ISD, as also explained at the beginning of Chapter 3. Additional measurement parameters are available in Table 3.1.

Table 3.1: Measurement parameters

Parameter	Value
Center frequency	2.68 GHz
Bandwidth	18.36 MHz
No. of pilots (N)	144
MIMO capabilities	2x2 per BS
No. of BSs	6 (up to 12x2 links)
CSI update interval	10 ms
Maximal speed	2.8 m/s \approx 10 km/h
Inter-site-distance	\approx 500 m
BS transmit power	36.5 dBm
Terminal's noise floor	-95 dBm

At the receiver side, our test terminal was used, which has been synchronized over the air. The terminal has been able to detect the CSI reference signals and convert them into an Ethernet packet stream, as described in [64]. This packet data stream is tapped at the terminal and recorded using a notebook computer. The terminal performs coarse timing adjustment with respect to the CP used in the OFDM system. As a result, the mean multi-cell delay is measured and the impulse response is placed according to the CP.

Estimation of channel model parameters

The import filter extracts a $2 \times 12 \times 144$ channel tensor for each 10 ms of the recorded packet stream. The dimensions correspond to the number of receive antennas, the number of transmit antennas and the number of pilots, respectively. The 144 channel coefficients of each Tx-Rx link can be seen as

$$Y_n = H_n + V_n, \quad n \in \{1, 2, \dots, 144\} \quad (3.6)$$

where Y is the measurement of the broadband radio channel H in frequency domain at N fixed pilot positions ν_n . These pilot positions are not exactly equidistant in our system. The estimation error is given by V_n , which is assumed to be additive white Gaussian noise (AWGN). The preprocessing technique described in [80, 86] has been used to extract the contributing multipath components. Essentially, the preprocessing calculates all parameters α and ϕ and τ which sum up to

$$\hat{H}_n = \sum_{l=1}^L \alpha_l \cdot e^{j\phi_l} \cdot e^{-2\pi j \cdot \tau_l \cdot B \cdot \nu_n} \quad (3.7)$$

where α_l is the amplitude, ϕ_l is the phase and τ_l is the delay of each multipath component, while B denotes the bandwidth, measured in Hz. These parameters are the input for all following evaluation steps. Due to the processing, \hat{H} has a SNR which is approximately 6 dB better than in Y since a significant part of the noise can be removed.

From the measured channel coefficients, the shadow fading is obtained according to T.S. Rappaport [84]. The instantaneous path gain is first estimated from the preprocessed data by averaging all signal components over all transmit and receive antennas of one sector

$$P = \frac{1}{N_t N_r} \cdot \sum_{t=1}^{N_t} \sum_{r=1}^{N_r} p_{r,t} \quad p_{r,t} = \sum_{l=1}^L \alpha_{l,r,t}^2 \quad (3.8)$$

where P is the total power of a PDP. Power values for the two sectors at each site are averaged. The resulting values are then additionally averaged over segments of 5 m length to remove small scale fading effects which results in a total of 692 measurement values per BS. The shadow fading (3.1) in logarithmic notation notes

$$g^{dB}(d) = G_1^{dB} + \gamma \cdot 10 \log_{10}(d) + X \quad (3.9)$$

The average path gain G_1^{dB} and path loss exponent γ have been calculated by linearly fitting the measured data to the linear slope and then calculating the remaining variance. The RMS delay spreads have been calculated by

$$\tau_{\text{RMS}} = \sqrt{\sum_{l=1}^L \frac{\alpha_l^2}{P_t} \cdot \tau_l^2 - \tau_m^2}, \quad \tau_m = \sum_{l=1}^L \frac{\alpha_l^2}{P_t} \cdot \tau_l \quad (3.10)$$

with τ_l as the delay and α_l^2 the power of the l^{th} channel tap. τ_m is the mean delay and P_t is the total power. Again, parameters T_1 and ϵ are calculated by transforming (3.2) into logarithmic domain and linear fitting.

3.4 Model validation and results

In this section, the channel model is validated by using data from channel measurements. The impact of antenna downtilt is studied and for the cases where the main beams hit the ground at 0.9 and 0.33 times the ISD. To this end, a multi-cellular simulation environment with an ISD of 500 m is used and terminals are placed on the same positions as in the testbed, which is shown in Figure 2.5. Independent channels are generated for the HHI, TUB and T-Labs links by using the channel model as in (3.1) to (3.3) and parameters listed in Table 3.2. Based on that synthetic channels, evaluation of the RMS delay spread by equation (3.10) and the 95% excess delay is performed over 5000 independent and identically distributed (i.i.d.) multi-cell channel realizations. Finally, the ISD is increased and the delay statistics are predicted by the model using the same parameters.

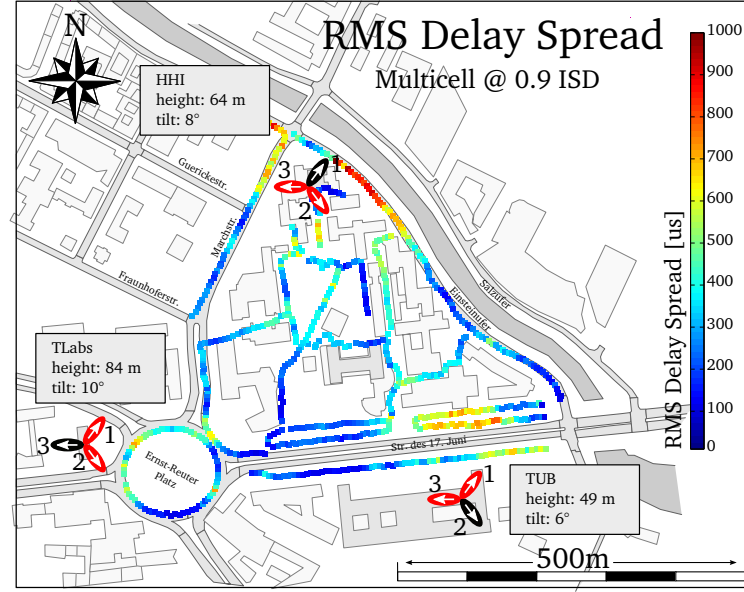


Figure 3.3: RMS delay spread measurements. The main beam of antennas meets the ground at a distance of 0.9 times the inter-site distance.

Table 3.2: Model parameters extracted from measurement

Model parameter	Estimated Values (HHI/TUB/TLabs)
Average path gain (G_1)	107.4 / 126.9 / 106.6 [dB]
Path loss exponent (γ)	2.0 / 6.3 / 3.0
Median of τ_{RMS} (T_1)	0.4 / 0.3 / 0.3 [μs]
Exponent ϵ	0.5 / 0.2 / 0.2
Variance σ_x	5.5 / 7.8 / 6.9 [dB]
Variance σ_y	1.7 / 1.8 / 1.5 [dB]
Correlation coefficient (ρ)	-0.7 / -0.3 / -0.6

All parameters estimated from measurements, which are needed in the channel model, are listed in Table 3.2. It is mentioned that measurements from positions closer than 210 m to the BS were excluded from the evaluation. At these positions, large propagation delays due to multiple reflexions on surrounding buildings were observed, while the direct signal was attenuated by the transmit antenna pattern. Such critical effects could only be captured by a 3D channel model and were thus excluded here.

In Figure 3.3, a geographic map including results for the RMS delay spread is shown for an antenna downtilt where the main beam hits the ground at 0.9 times ISD. Figure 3.4 and Figure 3.5 show the 95% excess delay for an antenna downtilt of 0.9 and 0.33 times ISD, respectively.

Figure 3.6 illustrates the cumulative distribution function (CDF) of the RMS delay spread (τ_{RMS}) for the multi-cell channel. The black curve shows the measured values for

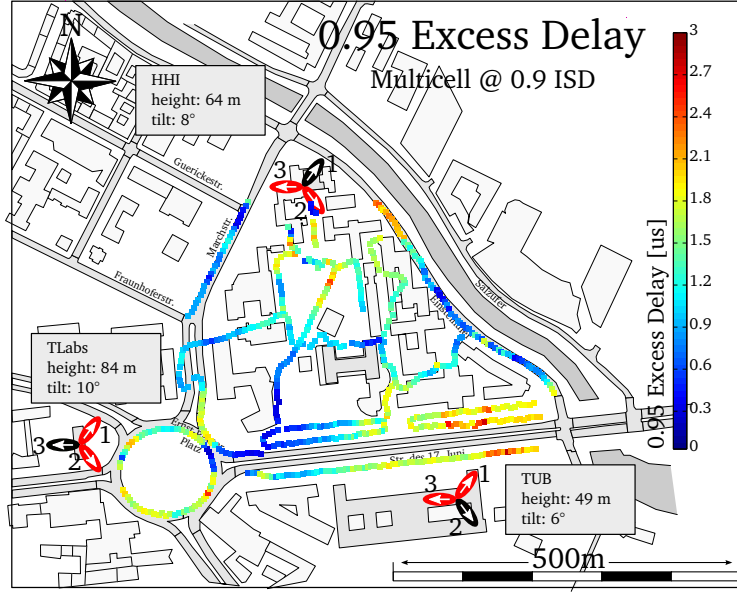


Figure 3.4: Multi-cell 95% excess delay measurements. The main beam of antennas meets the ground at a distance of 0.9 times the inter-site distance.

a 0.9 times ISD antenna downtilt, while the blue curve for 0.33 times ISD. These values have been taken from the route shown in Figure 3.3. It is observed that by tilting the antennas to smaller fractions of the ISD, significantly smaller RMS delay values can be realized. The illuminated region in the cell is then more close to the BS and scattered signals have less delay. The statistics shown by the dashed red line are for measurement points with a distance larger of 210 m to the base stations, and are mostly due to the overlap region covered jointly between the three sites in the central area of the campus. The numerical evaluation of the parameterized model leads to solid red line in Figure 3.6, which is actually not far from the measured (dashed) line in the same area. These results indicate that the parameterization of Greenstein's model is valid for the overlap region between the cells, where the most interference occurs.

Figure 3.7 illustrates the CDF of the 95% excess delay (τ_{95}), i.e. the 95-percentile of the cumulative PDP, which limits the signal-to-interference ratio (SIR) contribution of the ISI to 13 dB. These values refer to Figure 3.4 and Figure 3.5 for the two different down tilts. For the same measurement and simulation scenario as for the RMS delay spread evaluation, results yield similar observations. The model predicts the expected delay parameters quite precisely, only slightly more optimistic.

Finally, we use the (parameterized and validated) model for predicting the delay statistics for larger ISD. Channel parameters from Table 3.2 and uniform user allocation is assumed within the region defined by the three BSs. Figure 3.8 and Figure 3.9 illustrate the RMS delay spread and the 95% excess delay, respectively, for an ISD of 500, 1000 and 1732 m (maximum distance according to 3GPP [31]). It can be observed that even for the largest

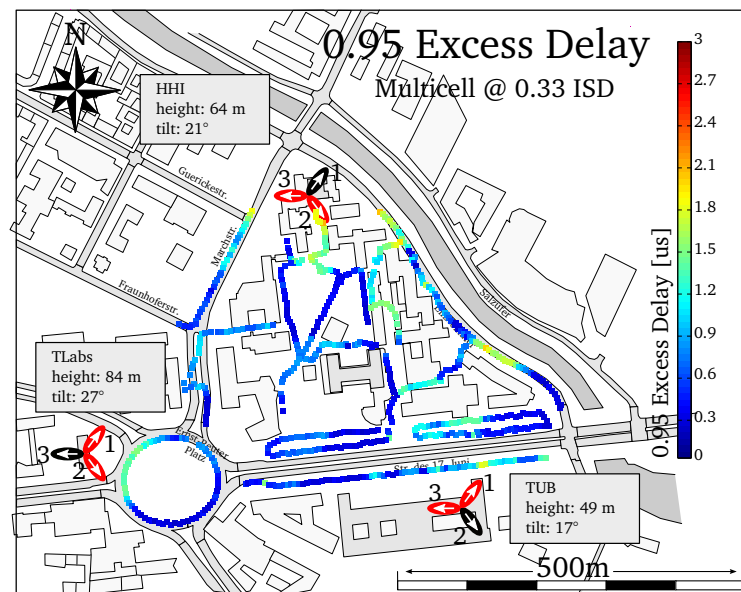


Figure 3.5: Multi-cell 95% excess delay measurements. The main beam of antennas meets the ground at a distance of 0.33 times the inter-site distance.

ISD used in LTE-A simulation assumptions, the 95% excess delay exceeds the short CP length of $4.7 \mu\text{s}$ in LTE-A in less than 5% of the cases.

3.5 Summary of Chapter 3

In this chapter, Greenstein’s statistical channel model was extended for covering broadband joint transmission from geographically distributed base stations. Data from multi-cellular channel measurements were used for verifying and parameterizing the model. The model was verified in terms of RMS delay spread and 95% excess delay. Despite of using a 2D model in a 3D setup, it predicts the channel delay parameters in the multi-cell case quite precisely at least at larger distances from the base stations. Close to the base stations, however, we observe deviations from the predicted statistics if the downtilt is set in a way that the main beam touches the ground at 0.9 times the inter-site-distance (small downtilt).

The impact of antenna downtilt on the channel delay statistics was studied and it was found that when using a larger downtilt, significantly smaller channel delay spreads can be realized. With a larger downtilt set to 0.33 times the ISD, the overall delay statistics is mostly due to the overlap region covered jointly between adjacent sites, where the model is more appropriate.

Finally, larger ISDs were considered and the delay statistics were predicted by using the developed model. Results indicated that base station cooperation in LTE-A is feasible for larger distances up to 1.7 km between the sites without violating the short cyclic prefix.

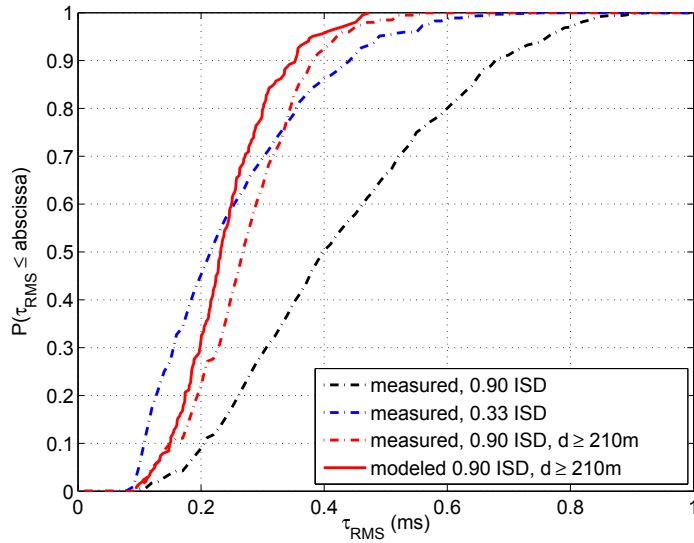


Figure 3.6: Multi-cell RMS delay spread (τ_{RMS}); main beam of antennas hits the ground at 0.9 or 0.33 times the inter-site-distance. Model is used for prediction at positions at least 210 m away from the base stations.

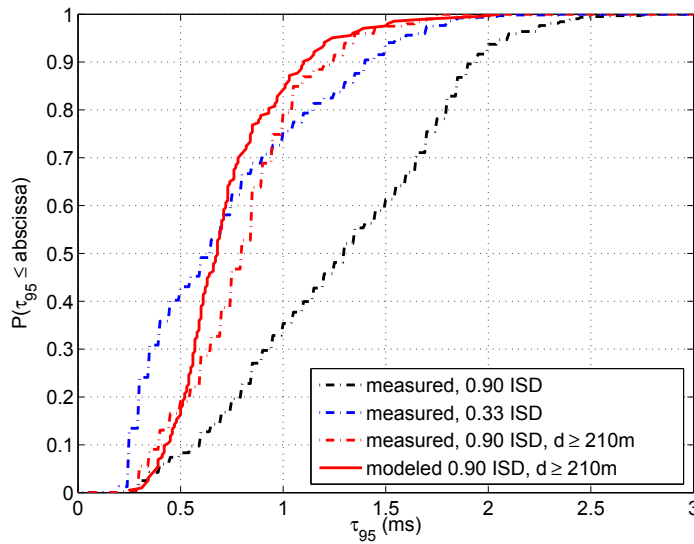


Figure 3.7: Multi-cell 95% excess delay (τ_{95}). The main beam of antennas hits the ground at 0.9 or 0.33 times the inter-site-distance. Model is used for prediction at positions at least 210 m away from the base stations.

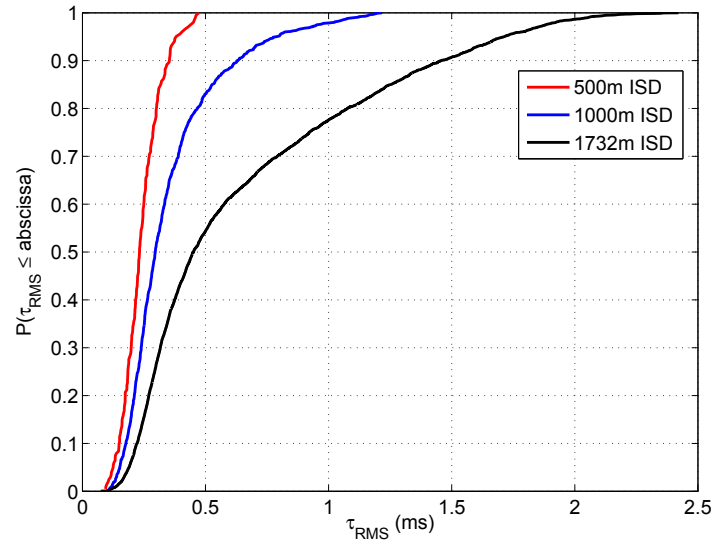


Figure 3.8: Predicted multi-cell RMS delay spread (τ_{RMS}) for larger inter-site-distances and uniform user allocation between the base stations.

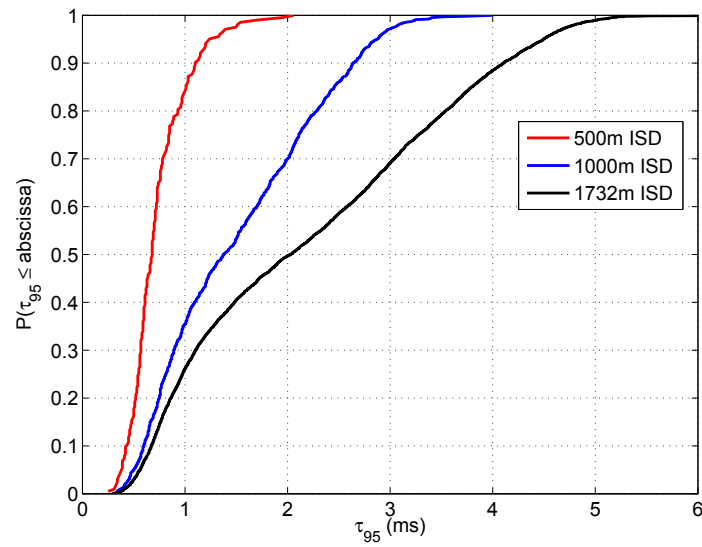


Figure 3.9: Predicted multi-cell 95% excess delay (τ_{95}) for larger inter-site-distances and uniform user allocation between the base stations.

4 Synchronization Impairments in OFDM-based CoMP

In this chapter, an exact signal model is established for multi-user multi-cellular cooperative networks that use orthogonal frequency division multiplexing (OFDM) for the air interface, describing the joint effect of multiple carrier and sampling frequency offsets. From there it is shown that the impact of the sampling offsets is negligible compared to the impact of the offsets in carrier frequency. The model is extended for studying the downlink of base-coordinated networks with zero-forcing precoding. Closed-form expressions are derived for the mean power of a mobile users' self-signal, inter-user and inter-carrier interferences, from which it is shown that inter-user interference is the main source of signal degradation. The resulting signal-to-interference ratio (SIR) is inverse to the frequency offsets' variance and to the square of time since the last precoder update, whereas it grows with the number of cooperating base stations and drops with the number of jointly served users. An SIR upper bound is also derived, which can be approached by appropriate user selection. It is further shown that the effect of synchronization impairments can be modeled by an equivalent channel error, for which analytical mean square error (MSE) expressions are derived.

Regarding the synchronization requirements of coordinated base stations, it is found that for a cluster of 7 base stations serving jointly 6 single-antenna terminals and attaining 10 ms after the latest precoder update an average SIR of 25 dB, high quality oven-controlled crystal oscillators (OCXOs) are needed. For attaining this required accuracy, system design recommendations are provided, such as using GPS and network-based synchronization solutions, which are described here.

Introduction

Base station cooperation, also known as coordinated multi-point (CoMP), is an ambitious multiple-antenna technique, where antennas of multiple distributed base stations and those of multiple terminals served within those cells are considered as a distributed multiple-input multiple-output (MIMO) system [36, 52, 53]. In the downlink, also known as joint transmission (JT) CoMP, signal pre-processing at the base stations is applied to eliminate the inter-cell interference and to enhance the spectral efficiency. In the simplest case, data symbols are precoded with the pseudo-inverse of the MIMO channel matrix; this method is known as zero-forcing (ZF) precoding [49]. Using ZF precoding, system performance becomes close to optimal in the high signal-to-noise ratio (SNR) regime, as shown in [55]. Deployment concepts for JT CoMP and field trial results have been reported in [67],

whereas recent progress can be found in [65] and [66]. The role of CoMP and integration aspects into next generation cellular systems are highlighted in [87]. Finally, an overview on cooperative communications can be found in [68].

The combination of MIMO techniques with OFDM has been a successful concept for broadband cellular networks and has enabled a significant increase of the spectral efficiency during the last years [34,56]. However, it quickly became clear that precise synchronization is vital for realizing the potential of MIMO-OFDM systems. It is known from [88] that the carrier frequency offset (CFO) causes inter-carrier interference (ICI) as well as a phase drift on all OFDM subcarriers, known as common phase error (CPE). The sampling frequency offset (SFO) is also a source of ICI, and implies a phase drift that grows linearly with frequency, thus affecting each subcarrier differently. Accurate maximum-likelihood (ML) tracking algorithms have been developed and optimized for single-user point-to-point MIMO-OFDM in [30], whereas synchronization for multi-user MIMO within one cell has been studied in [89]. For the OFDM-based multi-user uplink, a signal model and CFO compensation techniques have been developed in [90]. Analysis of the joint effect of the receivers' CFO and SFO in the multi-user MIMO downlink has been provided in [91], with the transmitter being perfectly synchronized.

Considering distributed JT CoMP, cooperative base stations are located at different sites, which implies that their frequency up- and down-converters are driven by their own local oscillators, while sampling frequencies also differ among them. Signal modeling of JT CoMP with individual offsets in carrier and sampling frequencies in [92] revealed that orthogonality between multiple users' data signals is misaligned and inter-user interference (IUI) arises. First insights into the performance degradation were obtained by numerical evaluation. In chapter 8 of [93], the sensitivity of CoMP to the CFO was analyzed for a scenario with two cooperating base stations. Similar observations have been reported in [94] and [95], whereas methods for estimating multiple CFOs based on training signals have been developed in [96]. The problem of non-synchronized cooperating base stations has been also investigated in [97–99], where, the focus has been on how to estimate and compensate the multiple CFOs. In [100], propagation delay differences were also included for transmissions from distributed base stations with multiple CFOs. In [101], a scheme for synchronizing base stations has been proposed, based on a time-slotted round-trip carrier synchronization protocol. The implementation of Global Positioning System (GPS)-based synchronization for distributed base stations in an outdoor testbed has been reported by the authors in [102]. More recently, an over-the-air synchronization protocol has been proposed in [103], which is also applicable for networks with a large number of access points. A survey on physical layer synchronization for distributed wireless networks can be found in [104].

A first objective of the present chapter is to investigate the synchronization requirements for base-coordinated multi-cellular MIMO networks. A major contribution of this work is the derivation of an *exact* signal model capturing the joint effect of multiple CFOs and

SFOs at transmitters and receivers in a MIMO-OFDM system and over the time. Based on this model, it is shown that the impact of the SFO is negligible compared to the one of the CFO. Application of the model to the distributed CoMP downlink with ZF precoding leads to analytical closed-form expressions for the mean power of the users' self-signal, inter-user and inter-carrier interferences. It is found that the inter-user interference is the dominant source of signal degradation and that synchronization requirements for cooperating base stations are very high, compared to the ones in single-cell transmission. The mean SIR is analyzed and is approximately found to degrade quadratically with time and to be inversely proportional to the variance of the base stations' CFO. The SIR further grows with the number of base stations and drops with the number of users. In addition to the SIR analysis for the Rayleigh fading channel, an SIR upper bound is derived, which can be approached by appropriate user selection. Finally, recommendations for practical synchronization of distributed wireless networks are given.

The rest of the chapter is organized as follows. In Section 4.1, a general signal model for a MIMO-OFDM communication system in the presence of multiple CFOs and SFOs is derived. In Section 4.2, the model is applied to the CoMP downlink and expressions are derived for mobile users' self-signal, inter-user and inter-carrier interferences. Analysis in Section 4.3 leads to closed-form expressions for the mean power of the above signals and the resulting SIR. The system performance is evaluated analytically and verified by means of simulations in Section 4.4. Synchronization requirements are established and practical methods to fulfill them are discussed in Section 4.6. Finally, conclusions are summarized in Section 6.1.

4.1 MIMO-OFDM signal model with carrier and sampling frequency offsets

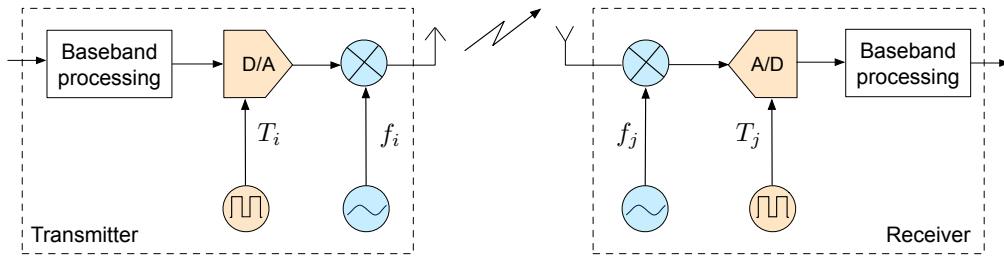


Figure 4.1: Single-link system where transmitter and receiver have individual sampling periods T_i and T_j for digital-to-analog and analog-to-digital conversion and individual carrier frequencies f_i and f_j for up- and down-conversion.

In the following, a distributed MIMO network is considered with an arbitrary number of antenna branches at every base station and at every user. The cellular network uses OFDM for the air interface, with N_s subcarriers, which are indexed with k in the range

$\{\frac{-N_s}{2}, \dots, \frac{N_s}{2} - 1\}$. An entire OFDM symbol is N_g samples long, equal to N_s samples plus the number of samples of the cyclic prefix. Integer n indexes successive OFDM symbols and is hence a measure of time.

Each base station and each mobile are assumed to have their own carrier and sampling frequency, within typical ranges. The total number of transmit branches is N_t . Each transmit branch (can be a base station in the downlink or a user in the uplink), denoted by subindex i , has its individual sampling period T_i , carrier frequency f_i and respective initial phase parameters τ_i and φ_i . In Figure 4.1, it is shown for a point-to-point transmission how sampling and carrier offsets misalign analog-to-digital and digital-to-analog conversion, as well as frequency conversion, respectively. The corresponding receiver parameters are denoted as T_j , f_j , τ_j and φ_j , while symbol j is used for $\sqrt{-1}$. The digital modulation of subcarrier k on transmit branch i is represented by the complex-valued symbol $X_i(k)$. Due to different sampling timings between transmit branches of different base stations (downlink) or among mobile users (uplink), the inter-carrier spacing is transmit-branch-specific and measures $\delta_i = (N_s T_i)^{-1}$ Hertz. The ideal carrier frequency is denoted by f_c and the ideal sampling period with T . For any transmitter or receiver, its CFO and SFO are defined as the deviation from the ideal carrier frequency and sampling period, respectively. The complex baseband-equivalent frequency response of the passband channel between transmitter i and receiver j at frequency f is denoted by $H_{ji}(f)$. It includes frequency-flat path loss and shadow fading as well as frequency-selective small-scale fading.

By following similar arguments as the ones leading to equation (8) in [30], and by considering the clarification in [105], i.e. corrections in magnitude in order to keep signal energies consistent, it is found that the spectrum of the OFDM signal observed at any given receive branch j has the form

$$Y_j(f) = U_j(f, k) + \bar{U}_j(f, k) + N_j(f), \quad (4.1)$$

where $U_j(f, k)$ represents the continuous-frequency spectrum of the received multi-user signal at receive antenna j for transmitted subcarrier k (on-carrier signal). It is noted that $\bar{U}_j(f, k)$ is the received spectrum of the multi-user signal of all other subcarriers $\nu \neq k$, i.e. the multi-user ICI (it is arbitrary which subcarrier is designated as k , but our analysis requires to single out one of them). The additive white Gaussian noise (AWGN) contributed by the front-end of receive antenna j is denoted by $N_j(f)$. The above terms are given by

$$\begin{aligned} U_j(f, k) = & T_j \sum_{i=1}^{N_t} e^{j(\varphi_j - \varphi_i)} \beta_{ji}(f, k) \\ & \cdot X_i(k) H_{ji}(k\delta_i + f_i - f_c), \end{aligned} \quad (4.2)$$

$$\begin{aligned} \bar{U}_j(f, k) &= T_j \sum_{\substack{\nu=-\frac{N_s}{2} \\ \nu \neq k}}^{\frac{N_s}{2}-1} \sum_{i=1}^{N_t} e^{j(\varphi_j - \varphi_i)} \beta_{ji}(f, \nu) \\ &\quad \cdot X_i(\nu) H_{ji}(\nu \delta_i + f_i - f_c), \end{aligned} \quad (4.3)$$

with

$$\begin{aligned} \beta_{ji}(f, k) &= e^{-j2\pi(f_j - f_i)(nN_g T_j + \tau_j)} \\ &\quad \cdot e^{-j2\pi k \delta_i (nN_g T_i + \tau_i - nN_g T_j - \tau_j)} \\ &\quad \cdot e^{-j\pi(f + f_j - f_i - k\delta_i)T_j(N_s - 1)} \\ &\quad \cdot \frac{\sin[\pi(f + f_j - f_i - k\delta_i)T_j N_s]}{\sin[\pi(f + f_j - f_i - k\delta_i)T_j]}. \end{aligned} \quad (4.4)$$

The exponential terms in (4.4) are phase shifts due to carrier and sampling frequency misalignment, while the fractional term describes the loss of orthogonality among OFDM subcarriers, causing a leakage of the signal transmitted on subcarrier k . Note that $H_{ji}(k\delta_i + f_i - f_c)$ expresses the channel at the frequency of subcarrier k plus a shift due to the transmitter's SFO and CFO.

The model given by (4.1) through (4.4) makes no assumption about the synchronization among branches and it is general for any MIMO-OFDM communication, also including cellular networks with base station cooperation. It describes how successive OFDM symbols are degraded under constant and uncompensated CFOs and SFOs as time goes by, i.e. OFDM symbol index n grows. The CFO must be smaller than half of a subcarrier spacing. For typical mobile receivers this implies that an earlier coarse frequency synchronization stage has been succeeded, which we assume henceforth. Regarding SFO, the expressions are valid well beyond the typical range specified for SFO in commercial OFDM systems. It is to be noted, however, that for a given SFO, the FFT window of each receiver branch does eventually drift away to a point at which inter-symbol interference (ISI) arises between OFDM symbols. From that point on, severe degradation ensues and the model stops being valid. It is also implicit in our model that OFDM symbol timing has been acquired in a prior stage. The result assumes that the time dispersion of all the MIMO channel impulse responses, also from distributed base stations and mobile users, is shorter than the OFDM cyclic prefix in use.

Returning to the model, it can be observed in (4.2) and (4.3) that the phase offsets due to τ_i , τ_j , φ_i and φ_j may be considered, without loss of generality, as part of the channel. It follows that we may choose $\tau_i = 0$, $\tau_j = 0$, $\varphi_i = 0$ and $\varphi_j = 0$. We also point out that in a practical implementation, for the j -th OFDM receiver branch, the output of its FFT corresponds to a sequence of samples of $Y_j(f)$ taken at frequencies $f = \frac{l}{N_s T_j} = l\delta_j$, where l is the subcarrier index ($-\frac{N_s}{2} \leq l \leq \frac{N_s}{2} - 1$) and δ_j is the receiver-side inter-carrier spacing. Note that l points to a slightly different frequency at each receive branch due to the different SFO, and generally also to a different frequency than pointed at by index k at the various

transmit branches i . Imposing the above conditions on (4.2) and (4.3), and focusing on an arbitrary received subcarrier $l = k$, we obtain the following discrete-frequency signal model:

$$Y_j(k) = U_j(k) + \bar{U}_j(k) + N_j(k), \quad (4.5)$$

with

$$U_j(k) = \sum_{i=1}^{N_t} \beta_{ji}(k, k) X_i(k) H_{ji}(k), \quad (4.6)$$

$$\bar{U}_j(k) = \sum_{\substack{\nu=-\frac{N_s}{2} \\ \nu \neq k}}^{\frac{N_s}{2}-1} \sum_{i=1}^{N_t} \beta_{ji}(k, \nu) X_i(\nu) H_{ji}(\nu), \quad (4.7)$$

$$\begin{aligned} \beta_{ji}(k, \nu) = & e^{-j2\pi n N_g T_j (f_j - f_i)} \\ & \cdot e^{-j2\pi n N_g \nu \delta_i (T_i - T_j)} \\ & \cdot e^{-j\pi \frac{N_s - 1}{N_s} \left[\left(k - \nu \frac{T_j}{T_i} \right) + (f_j - f_i) T_j N_s \right]} \\ & \cdot \frac{1}{N_s} \frac{\sin \left[\pi \left(k - \nu \frac{T_j}{T_i} \right) + \pi (f_j - f_i) T_j N_s \right]}{\sin \left[\frac{\pi}{N_s} \left(k - \nu \frac{T_j}{T_i} \right) + \pi (f_j - f_i) T_j \right]}, \end{aligned} \quad (4.8)$$

and with $N_j(k)$ the receiver-side AWGN, of power $N_0 \delta_j$. Note that in (4.6) and (4.7) we have approximated and defined $H_{ji}(k \delta_i + f_i - f_c) \approx H_{ji}(k \delta_i) \triangleq H_{ji}(k)$, because $|f_i - f_c|$ is assumed to be much smaller than the coherence bandwidth of the channel.

In practical system implementation, the carrier and sampling frequency clocks of a transmitter or receiver are derived from the same reference, i.e. from the same local oscillator. Thus, for the product of an arbitrary i^{th} carrier frequency and sampling period $f_i \cdot T_i \triangleq \kappa$, it holds that $\kappa \gg 1$, as the (ideal) carrier frequency f_c is two to three orders of magnitude larger than the (ideal) sampling frequency $1/T$. The constant κ depends only on the system and hardware design and is independent of i .

Considering this relationship in (4.8), it is straightforward to see that the exponent in the expression's second line, which captures the SFO effect on $\beta_{ji}(k, \nu)$ and which is maximized for $\nu = N_s$, still remains κ times smaller than the exponent in the first line capturing the CFO effect. Similar findings can be observed from comparing the influence of SFO with the one of the CFO onto the terms in the third and the fourth line of (4.8). Thus, it can be safely said that the impact of the SFO on $\beta_{ji}(k, \nu)$ is significantly weaker than the impact of the CFO, when using the same oscillator reference for both, at each individual transmitter and receiver.

The derivations up to here have been presented including both CFO and SFO for the sake of completeness, as well as for further reference. Expressions (4.5) through (4.9) provide the exact signal model, which characterizes the joint effect of multiple CFOs and SFOs over

consecutive OFDM symbols in MIMO transmissions and is one important contribution of this work. However, beyond signal modeling, this work further aims to identify the major degradation sources, analyze the performance degradation and determine from there the actual system requirements. To this end, in the following we focus on the CFO and neglect the SFO, by assuming ideal sampling for all transmitters and receivers. With $T_i = T_j = T$, (4.8) becomes

$$\begin{aligned} \beta_{ji}(k, \nu) = & e^{-j2\pi \left[(f_j - f_i)t_n + \frac{N_s - 1}{2N_s} (k - \nu) \right]} \\ & \cdot \frac{1}{N_s} \frac{\sin[\pi(k - \nu) + \pi(f_j - f_i)TN_s]}{\sin\left[\frac{\pi}{N_s}(k - \nu) + \pi(f_j - f_i)T\right]}, \end{aligned} \quad (4.9)$$

The discrete time variable $t_n \triangleq (nN_g + \frac{N_s - 1}{2})T$ has been defined for convenience and is measured in seconds.

Expressions (4.5) to (4.9) provide the discrete-frequency signal model for a MIMO-OFDM communication system in the presence of multiple CFOs and SFOs as a function of time, and will be used in the following section.

4.2 Precoded multi-cell downlink signal model

Now we specialize the model obtained in Section 4.1 to the CoMP downlink including joint precoding of the data signals. Here, the required channel state information (CSI) for the precoder calculation is estimated either at the base stations or at the terminals and fed back to the base stations, depending on whether time division duplex (TDD) or frequency division duplex (FDD) is used. For distributed base stations, coordination by means of a backhaul network is considered, which enables fast exchange of data and CSI.

It is to be noted that channel estimation errors and CSI delays due to the feedback and the backhaul network are not considered in this work. Their effect on JT CoMP is important and might even overwhelm the effects of imperfect synchronization, which we are analyzing here. A distinct analysis by the authors which includes the effect of imperfect channel knowledge and derives the resulting performance limitations can be found in [106]. We will therefore assume here that perfect knowledge of the downlink multi-cell multi-user MIMO channel matrix is available at the base stations and is used for real-time precoding of the downlink signals. As already mentioned in Section 4.1, residual phase terms due to CFOs and SFOs are also considered as part of the (perfectly estimated) channel. We consider N_u users, equipped with single-antenna terminals, which are jointly served by N_b coordinated antenna branches among all base stations forming the cooperation cluster. There is no exchange of information between mobile users and out-of-cluster transmission is not considered in our model.

Transmissions are precoded on each OFDM subcarrier k with the right-hand pseudo-inverse of the $N_u \times N_b$ downlink MIMO channel matrix $\mathbf{H}(k)$ for that subcarrier, given by

$$\mathbf{W}(k) = \mathbf{H}^H(k)[\mathbf{H}(k)\mathbf{H}^H(k)]^{-1}. \quad (4.10)$$

The inverse is of size $N_b \times N_u$ and we assume it exists for $N_b > N_u$. Note that this condition can be met in practice by appropriate user selection and clustering of base stations, which is thereby assumed.

Next, consider $\mathbf{S}(k)$ to be an $N_u \times 1$ vector that contains the complex-valued data symbols $s_u(k)$ to be transmitted to the N_u users on subcarrier k . Then, the $N_b \times 1$ vector $\mathbf{X}(k)$ of precoded symbols $X_b(k)$ to be transmitted on subcarrier k by the N_b base stations is $\mathbf{X}(k) = \mathbf{W}(k)\mathbf{S}(k)$, where elements are given by

$$X_b(k) = \sum_{u=1}^{N_u} w_{bu}(k)s_u(k), \quad (4.11)$$

and $w_{bu}(k)$ are the elements of $\mathbf{W}(k)$. Transmitter index i has been replaced with b to stress that from here on, transmitters are base stations. Imposing the expression of the precoded symbol (4.11) into $U_j(k)$ given by (4.6), we obtain the on-carrier signal on subcarrier k of user j , given by

$$U_j(k) = \check{s}_j(k) + \bar{s}_j(k), \quad (4.12)$$

with

$$\check{s}_j(k) = s_j(k) \sum_{b=1}^{N_b} \beta_{jb}(k, k) H_{jb}(k) w_{bj}(k) \quad (4.13)$$

and

$$\bar{s}_j(k) = \sum_{\substack{u=1 \\ u \neq j}}^{N_u} s_u(k) \sum_{b=1}^{N_b} \beta_{jb}(k, k) H_{jb}(k) w_{bu}(k). \quad (4.14)$$

Above, an arbitrary user j has been singled out in (4.13) from the remaining users. Thus, $\check{s}_j(k)$ represents the self-signal, while $\bar{s}_j(k)$ represents the IUI observed by user j , given by (4.14). This interference is due to the loss of orthogonality of the precoded transmission to multiple users, caused by synchronization impairments. Imposing (4.11) into $\bar{U}_j(k)$ in (4.7), we obtain the ICI on subcarrier k of user j , given by

$$\bar{U}_j(k) = \sum_{\substack{\nu=-\frac{N_s}{2} \\ \nu \neq k}}^{\frac{N_s}{2}-1} \sum_{u=1}^{N_u} s_u(\nu) \sum_{b=1}^{N_b} \beta_{jb}(k, \nu) H_{jb}(\nu) w_{bu}(\nu). \quad (4.15)$$

Our complete discrete-frequency CoMP downlink signal model is then

$$Y_j(k) = \check{s}_j(k) + \bar{s}_j(k) + \bar{U}_j(k) + N_j(k), \quad (4.16)$$

with $\check{s}_j(k)$, $\bar{s}_j(k)$ and $\bar{U}_j(k)$ given by (4.13), (4.14) and (4.15), respectively, and $N_j(k)$ the

AWGN of power $N_0\delta_j$. It is noted that the model of Section 4.2 is valid independently if using for $\beta_{ji}(k, \nu)$ the exact expression (4.8) or its simplification (4.9), where the SFO is neglected.

Signal model (4.16) can be expressed also in matrix notation as

$$Y_j(k) = \underbrace{\mathbf{H}_j(k)\mathbf{B}_j(k, k)\mathbf{W}(k)\mathbf{s}(k)}_{U_j(k)} + \underbrace{\sum_{\substack{\nu=-\frac{N_s}{2} \\ \nu \neq k}}^{\frac{N_s}{2}-1} \mathbf{H}_j(\nu)\mathbf{B}_j(k, \nu)\mathbf{W}(\nu)\mathbf{s}(\nu)}_{\bar{U}_j(k)} + N_j(k), \quad (4.17)$$

where the $N_b \times N_b$ diagonal matrix $\mathbf{B}_j(k, \nu) = \text{diag}(\beta_{j1}(k, \nu), \dots, \beta_{ji}(k, \nu), \dots, \beta_{jN_b}(k, \nu))$ captures the effect of imperfect synchronization between the observed user j and its N_b serving base stations. The $1 \times N_b$ channel vector is denoted by $\mathbf{H}_j(\nu)$. From (4.17) it is evident that for $\nu = k$, matrix $\mathbf{B}_j(k, k)$ violates the inverse relationship between the channel and the precoder, which is the origin of the inter-user interference.

4.3 Analysis of signal and interference powers

The following section contains an in-depth analysis of the impact of synchronization impairments onto the performance. It is organized as follows: first, we study the power of a user's self-signal (useful signal) and then the IUI and ICI. Next, we show that ICI is small compared to IUI and provide analytical expressions for the mean SIR. Finally, we highlight the value of user selection and show its impact onto the performance.

Conceptually, the rise of IUI and ICI due to imperfect synchronization can be understood as a dispersion of the energy allocated on a specific subcarrier of a specific user to other users (IUI) and to other subcarriers (ICI). This implies a drop of the self-signal power and a rise, on that user and that subcarrier, of the power of IUI and ICI from other users' and other subcarriers' losses. In what follows, we proceed under the assumption that data symbols are statistically independent between users and across subcarriers, i.e. $\mathbb{E}\{s_j(k)s_u^*(\nu)\} = E_s\delta_{ju}\delta_{k\nu}$, where $\mathbb{E}\{\cdot\}$ denotes the expectation operator, E_s the mean energy per data symbol and δ_{xy} the Kronecker delta between x and y .

4.3.1 Power of the user's self-signal

Since there is statistical independence between data symbols, channel coefficients and synchronization parameters, the mean power of the user's self-signal (4.13) is

$$\mathbb{E}\{|\check{s}_j|^2\} = E_s \sum_{b_1=1}^{N_b} \sum_{b_2=1}^{N_b} \mathbb{E}\{\beta_{jb_1}\beta_{jb_2}^*\} \mathbb{E}\{H_{jb_1}w_{b_1j}H_{jb_2}^*w_{b_2j}^*\}, \quad (4.18)$$

where subcarrier index k has been omitted for simplicity of notation and cross-terms equal to zero have been already disregarded.

In a first step, we analyze $\mathbb{E}\{\beta_{jb_1}\beta_{jb_2}^*\}$, which appears in (4.18). Using therefore $\nu = k$ in (4.9) and replacing transmitter index i with base station index b , we reach

$$\beta_{jb} = \frac{1}{N_s} \cdot e^{-j2\pi(f_j - f_b)t_n} \cdot \frac{\sin[\pi(f_j - f_b)TN_s]}{\sin[\pi(f_j - f_b)T]}, \quad (4.19)$$

which does not depend on the subcarrier index k . By noting that $|f_j - f_b| \ll \frac{1}{T}$, we can safely say that the argument $x = \pi(f_j - f_b)T$ of the $\sin(x)$ in the denominator of the fraction on the right-hand side of (4.19) is very small. The same term also appears in the exponential term, and both multiplicative terms in (4.19) are close to one. But, comparing the magnitude deviations from unity, we see that for typical synchronization parameters $\left|1 - \frac{1}{N_s} \frac{\sin(N_s x)}{\sin(x)}\right| \ll \left|1 - e^{-j(2.14n+1)N_s x}\right|$ (this results for $N_s \gg 1$ and a cyclic prefix equal to $0.07N_s$ [31]). In absolute terms, we can further use the first order Taylor series expansion $\frac{1}{N_s} \frac{\sin(N_s x)}{\sin(x)} \approx 1$ and reach

$$\beta_{jb_1}\beta_{jb_2}^* \approx e^{-j2\pi(f_j - f_{b_1})t_n} \cdot e^{j2\pi(f_j - f_{b_2})t_n} = e^{j2\pi(f_{b_1} - f_{b_2})t_n}. \quad (4.20)$$

It is interesting to observe that the power of the exponential term, as approximated in (4.20), depends on the difference between the base stations' carrier frequencies. The power loss effect of the symbol transmitted on subcarrier k , which is the generating factor of ICI, depends on both the CFOs of the base stations and of the mobile users. The effect has been neglected here due to its relatively small role compared to the one of the exponential term, will be however thoroughly analyzed in Section 4.3.2.

For transmission from one base station, i.e. for case $b_1 = b_2$, it is immediate that (4.20) equals one. For $b_1 \neq b_2$, it is reasonable to assume that different base stations' carrier frequencies f_{b_1} and f_{b_2} are statistically independent, which allows for expressing the expectation of (4.20) as a product of two terms, each depending on one base station's CFO:

$$\mathbb{E}\{\beta_{jb_1}\beta_{jb_2}^*\} = \mathbb{E}\left\{e^{j2\pi(f_{b_1} - f_c)t_n}\right\} \cdot \mathbb{E}\left\{e^{-j2\pi(f_{b_2} - f_c)t_n}\right\}. \quad (4.21)$$

By assuming further that the CFOs are identically distributed, the second term of the right-hand side in (4.21) is the complex-conjugate of the first one, hence (4.21) can be developed as

$$\mathbb{E}\{\beta_{jb_1}\beta_{jb_2}^*\} = \left|\mathbb{E}\left\{e^{-j2\pi(f_b - f_c)t_n}\right\}\right|^2 = \left|\int p_{(f_b - f_c)} e^{-j2\pi(f_b - f_c)t_n} d(f_b - f_c)\right|^2, \quad (4.22)$$

where $p_{(f_b - f_c)}$ denotes the probability distribution function (pdf) of the CFO $(f_b - f_c)$ and is independent on index b . It is to be noted that the integral in (4.22) is a Fourier

transform of the CFO's pdf. Hence, we can write

$$\mathbb{E} \{ \beta_{jb_1} \beta_{jb_2}^* \} = \begin{cases} 1, & b_1 = b_2 \\ |\mathcal{F}_p(t_n)|^2, & b_1 \neq b_2 \end{cases}, \quad (4.23)$$

where $\mathcal{F}_p(\cdot)$ denotes the Fourier transform of $p(f_b - f_c)$ and is here a function of time. For being a characteristic function, i.e. the Fourier transform of a pdf, it is guaranteed that $|\mathcal{F}_p(t_n)| \leq 1$ (see [107]), which means that the power of the user's self-signal (4.18) drops under imperfect carrier synchronization conditions.

Result (4.23) can be used for developing (4.18) further by separating the sum over b_2 into the cases $b_2 = b_1$ and $b_2 \neq b_1$:

$$\begin{aligned} \mathbb{E} \{ |\check{s}_j|^2 \} &= E_s \cdot \sum_{b=1}^{N_b} \mathbb{E} \{ |H_{jb} w_{bj}|^2 \} \\ &+ E_s \cdot |\mathcal{F}_p(t_n)|^2 \cdot \sum_{b_1=1}^{N_b} \sum_{\substack{b_2=1 \\ b_2 \neq b_1}}^{N_b} \mathbb{E} \{ H_{jb_1} H_{jb_2}^* w_{b_1j} w_{b_2j}^* \} \\ &= E_s \cdot (1 - |\mathcal{F}_p(t_n)|^2) \cdot \sum_{b=1}^{N_b} \mathbb{E} \{ |H_{jb} w_{bj}|^2 \} \\ &+ E_s \cdot |\mathcal{F}_p(t_n)|^2 \cdot \sum_{b_1=1}^{N_b} \sum_{b_2=1}^{N_b} \mathbb{E} \{ H_{jb_1} H_{jb_2}^* w_{b_1j} w_{b_2j}^* \}. \end{aligned} \quad (4.24)$$

The double sum in the last line in (4.24) can be formulated as

$$\sum_{b_1=1}^{N_b} \sum_{b_2=1}^{N_b} \mathbb{E} \{ H_{jb_1} H_{jb_2}^* w_{b_1j} w_{b_2j}^* \} = \sum_{b_1=1}^{N_b} \mathbb{E} \{ H_{jb_1} w_{b_1j} \} \cdot \sum_{b_2=1}^{N_b} \mathbb{E} \{ H_{jb_2}^* w_{b_2j}^* \},$$

which, by considering the ZF condition

$$\sum_{b=1}^{N_b} H_{jb} w_{bu} = \delta_{ju} \quad (4.25)$$

is found equal to 1. Thus, (4.24) can be written as

$$\mathbb{E} \{ |\check{s}_j|^2 \} = E_s \left[1 - (1 - |\mathcal{F}_p(t_n)|^2) K_U \right], \quad (4.26)$$

where we defined $K_U = 1 - \sum_{b=1}^{N_b} \mathbb{E} \{ |H_{jb} w_{bj}|^2 \}$. Note that (4.25) cannot be applied to the sum terms in the first and third line of (4.24) because of the power index. The constant K_U depends on the precoder and the channel statistical properties. As shown in Appendix 7.2.1 for ZF precoding, given a channel matrix with $N_b > N_u$ and complex

Gaussian independent and identically distributed (i.i.d.) entries (Rayleigh fading channel), with zero mean and variance σ_h^2 , K_U can be approximated as

$$K_U \approx 1 - \frac{1}{N_b - N_u}. \quad (4.27)$$

If we further consider the case in which the CFOs of the base stations are Gaussian i.i.d. with zero mean and variance σ_f^2 , the Fourier transform in (4.23) becomes

$$|\mathcal{F}_p(t_n)|^2 = e^{-4\pi^2\sigma_f^2 t_n^2} \approx 1 - 4\pi^2\sigma_f^2 t_n^2, \quad (4.28)$$

where the first order Taylor series expansion $e^{-x} \approx 1 - x$ has been used. It is to be noted that this approximation is accurate for typical values of σ_f and t_n . Using approximations (4.27) and (4.28), we can formulate the mean power of the user's self-signal (4.26) as

$$\mathbb{E} \{|\bar{s}_j|^2\} \approx E_s \left[1 - 4\pi^2\sigma_f^2 t_n^2 \cdot \left(1 - \frac{1}{N_b - N_u} \right) \right], \quad (4.29)$$

from where we see that it decreases linearly with the base stations' CFO variance and quadratically with time. Result (4.29) also shows that the mean power of the self-signal grows with the number of base stations and drops with the number of users. It is noteworthy that for $N_u = N_b - 1$, the mean power of the self-signal remains constant. However, this should not be used as a system design rule, as for determining the system performance, the degradation due to IUI and ICI must be considered as well.

4.3.2 Power of the inter-user interference

The derivation of the mean power of the IUI (4.14) follows similar steps as the ones in Section 4.3.1 above. Concretely:

$$\mathbb{E} \{|\bar{s}_j|^2\} = E_s \cdot \sum_{\substack{u=1 \\ u \neq j}}^{N_u} \sum_{b_1=1}^{N_b} \sum_{b_2=1}^{N_b} \mathbb{E} \{ \beta_{jb_1} \beta_{jb_2}^* \} \cdot \mathbb{E} \{ H_{jb_1} w_{b_1u} H_{jb_2}^* w_{b_2u}^* \}, \quad (4.30)$$

and noting that in this case always $j \neq u$ in (4.25), we find that

$$\mathbb{E} \{|\bar{s}_j|^2\} = E_s (1 - |\mathcal{F}_p(t_n)|^2) K_{\text{IUI}}, \quad (4.31)$$

where $K_{\text{IUI}} = \sum_{\substack{u=1 \\ u \neq j}}^{N_u} \sum_{b=1}^{N_b} \mathbb{E} \{ |H_{jb} w_{bu}|^2 \}$. If all users undergo identical channel statistics, K_{IUI} simplifies to $K_{\text{IUI}} = (N_u - 1) \cdot \sum_{b=1}^{N_b} \mathbb{E} \{ |H_{jb} w_{bu}|^2 \}$, whereas using the results of Appendix 7.2.1 for the Rayleigh fading channel and $N_b > N_u$, we find

$$K_{\text{IUI}} \approx \frac{N_u - 1}{N_b - N_u}. \quad (4.32)$$

Using (4.32) and (4.28) in (4.31), we obtain

$$\mathbb{E} \{ |\bar{s}_j|^2 \} \approx E_s \cdot 4\pi^2 \sigma_f^2 t_n^2 \cdot \frac{N_u - 1}{N_b - N_u}. \quad (4.33)$$

Result (4.33) reveals that the IUI power grows linearly with the base stations' CFO variance and quadratically with time. Using more base stations decreases the IUI power, while adding more users results in increasing it. Due to the approximation used in (4.20), it can be said that the impact of the mobile users' CFO onto the IUI power level is less significant than the impact of the base stations' CFOs.

4.3.3 Power of the inter-carrier interference

Following similar steps as before, now for (4.15), the mean power of the ICI is

$$\mathbb{E} \{ |\bar{U}_j(k)|^2 \} = E_s \cdot \sum_{\substack{\nu = -\frac{N_s}{2} \\ \nu \neq k}}^{\frac{N_s}{2}-1} \sum_{u=1}^{N_u} \sum_{b_1=1}^{N_b} \sum_{b_2=1}^{N_b} \mathbb{E} \{ \beta_{jb_1}(k, \nu) \beta_{jb_2}^*(k, \nu) \} \cdot \mathbb{E} \{ H_{jb_1}(\nu) w_{b_1u}(\nu) H_{jb_2}^*(\nu) w_{b_2u}^*(\nu) \}. \quad (4.34)$$

Assuming identical channel statistics for all subcarriers, the last term in (4.34) does not depend on subcarrier index ν and becomes $\mathbb{E} \{ H_{jb_1} w_{b_1u} H_{jb_2}^* w_{b_2u}^* \}$, already seen in Section 4.3.1 and Section 4.3.2. For convenience we define

$$\sum_{\substack{\nu = -\frac{N_s}{2} \\ \nu \neq k}}^{\frac{N_s}{2}-1} \mathbb{E} \{ \beta_{jb_1}(k, \nu) \beta_{jb_2}^*(k, \nu) \} \triangleq \begin{cases} B_1, & b_1 = b_2 \\ B_2, & b_1 \neq b_2 \end{cases}, \quad (4.35)$$

which is analyzed in Appendix 7.2.2. In (4.34), we separate the sum over b_2 into the cases $b_2 = b_1$ and $b_2 \neq b_1$ as in (4.24) and obtain:

$$\begin{aligned} \mathbb{E} \{ |\bar{U}_j(k)|^2 \} &= E_s \cdot B_1 \cdot \sum_{u=1}^{N_u} \sum_{b=1}^{N_b} \mathbb{E} \{ |H_{jb} w_{bu}|^2 \} \\ &+ E_s \cdot B_2 \cdot \sum_{u=1}^{N_u} \sum_{b_1=1}^{N_b} \sum_{\substack{b_2=1 \\ b_2 \neq b_1}}^{N_b} \mathbb{E} \{ H_{jb_1} w_{b_1u} H_{jb_2}^* w_{b_2u}^* \} \\ &= E_s \cdot (B_1 - B_2) \cdot \sum_{u=1}^{N_u} \sum_{b=1}^{N_b} \mathbb{E} \{ |H_{jb} w_{bu}|^2 \} \\ &+ E_s \cdot B_2 \cdot \sum_{u=1}^{N_u} \sum_{b_1=1}^{N_b} \sum_{b_2=1}^{N_b} \mathbb{E} \{ H_{jb_1} w_{b_1u} H_{jb_2}^* w_{b_2u}^* \}. \end{aligned} \quad (4.36)$$

We use the expressions for B_1 and B_2 in Appendix 7.2.2, which provide accurate approximations for Gaussian distributed CFOs for the base stations and the mobile user j with zero mean and variances σ_f^2 and $\sigma_{f,j}^2$, respectively, and reach

$$\mathbb{E} \{ |\bar{U}_j(k)|^2 \} \approx \frac{E_s \pi^2}{3\delta^2} \cdot (\sigma_f^2 \cdot K_{\text{ICI}} + \sigma_{f,j}^2). \quad (4.37)$$

Here, $K_{\text{ICI}} = \sum_{u=1}^{N_u} \sum_{b=1}^{N_b} \mathbb{E} \{ |H_{jb} w_{bu}|^2 \} = K_{\text{IUI}} - K_{\text{U}} + 1$ is a constant. For a Rayleigh fading MIMO channel, we use in (4.37) the expression provided by Appendix 7.2.1 for K_{ICI} and reach

$$\mathbb{E} \{ |\bar{U}_j(k)|^2 \} \approx \frac{E_s \pi^2}{3\delta^2} \cdot \left(\sigma_f^2 \cdot \frac{N_u}{N_b - N_u} + \sigma_{f,j}^2 \right). \quad (4.38)$$

Expression (4.38) shows that the mean power of the user's ICI can be split into two additive parts: a first part depending on the base stations' CFO variance, which is multiplied with a weighting factor K_{ICI} according to the cluster size, and a second part depending on the user's own CFO. Furthermore, (4.38) reveals that the power of the ICI does not vary with time and that it is inverse to the square of the OFDM subcarrier spacing.

4.3.4 ICI-to-IUI ratio and SIR

The relative magnitudes of the power terms derived so far in this section are analyzed next. A simple expression for the mean ICI-to-IUI power ratio of a user j (an interference-to-interference ratio, IIR) can be obtained from (4.33) and (4.38):

$$\text{IIR} = \frac{\mathbb{E} \{ |\bar{U}_j|^2 \}}{\mathbb{E} \{ |\bar{s}_j|^2 \}} \approx \frac{1}{12\delta^2 t_n^2} \cdot \left(\frac{N_u}{N_u - 1} + \xi^2 \frac{N_b - N_u}{N_u - 1} \right), \quad (4.39)$$

with $N_b > N_u \geq 2$ and $\xi = \sigma_{f,j}/\sigma_f$ defined as the ratio between the standard deviations of the user's and the base stations' CFOs. By replacing $\delta = (N_s T)^{-1}$ and discrete time $t_n = (1.07n + 0.5)N_s T$ (this results with $N_s \gg 1$ and a cyclic prefix equal to $0.07N_s$ [31]), relation (4.39) becomes

$$\text{IIR} \approx \frac{1}{12(1.07n + 0.5)^2} \cdot \left(\frac{N_u}{N_u - 1} + \xi^2 \frac{N_b - N_u}{N_u - 1} \right). \quad (4.40)$$

It is interesting to observe that in the approximation (4.40), the IIR does not depend on the OFDM system parameters, but only on the OFDM symbols index n .

Regarding the ratio ξ , it has been shown in [30] and [96] that mobile terminals attain a carrier frequency accuracy, which is at least one order of magnitude below the accuracy of typical base station oscillators used in Third Generation Partnership Project (3GPP) Long Term Evolution (LTE) [31]. Assuming for instance $\xi^2 \gg 1$, the first additive term in (4.40) becomes much smaller than the second term, indicating that the terminals' CFO is the main source of ICI. Using $\xi = 0$, one can evaluate the IIR including only the ICI part

due to the base stations' CFOs; in this case, the ratio does not depend on the base stations' CFOs at all. Using a more practical value of e.g. $\xi = 10$, the largest possible IIR after $n = 14$ OFDM symbols ($t_n \approx 1$ ms), which occurs with $N_u = 2$ users given $N_b = 7$, equals to -7.3 dB. The IIR drops quickly, down already to -27.3 dB for $n = 140$ ($t_n \approx 10$ ms). These quantitative results show that for typical JT CoMP scenarios, the IUI dominates over the ICI.

We will now neglect the ICI and define the mean SIR (self-user signal-to-IUI ratio) by the ratio between (4.26) and (4.31):

$$\text{SIR} = \frac{|\mathcal{F}_p(t_n)|^2}{(1 - |\mathcal{F}_p(t_n)|^2)K_{\text{IUI}}} - \frac{1}{N_u - 1}. \quad (4.41)$$

For a MIMO channel with i.i.d. Rayleigh fading entries (K_{IUI} given by (4.32)) and for i.i.d. Gaussian CFOs ($|\mathcal{F}_p(t_n)|^2$ given by (4.28)), expression (4.41) can be simplified as

$$\text{SIR} \approx \frac{1}{4\pi^2\sigma_f^2 t_n^2} \cdot \frac{N_b - N_u}{N_u - 1} - \frac{N_b - N_u + 1}{N_u - 1}. \quad (4.42)$$

Expressions (4.41) and (4.42) are valid for $N_b > N_u \geq 2$. Expression (4.42) reveals that for ZF precoding, the mean SIR is in an approximately inverse relation to the base stations' CFO variance and to the square of time. Furthermore, it is shown that the SIR grows with the number of base stations and drops with the number of jointly served users.

4.3.5 The value of user selection in JT CoMP and an SIR bound

It has been shown in [63] that the SNR gains in JT CoMP is increased if a scheduler selects the appropriate users to be jointly served on the same time and frequency resources. The selection criteria are based on the rule that all users gain from the cooperation in the cluster, compared to the case of non-coordinated transmission. Evaluated on a field scenario, the resulting singular value statistics after such user selection was found to be comparable to the one of a Rayleigh fading channel, fact that also relates to scenarios where users are located close to the cell edge, i.e. in which gains through coordination are particularly large.

Considering now an idealized scenario -from the precoding point of view- with orthogonal channel vectors of equal power among the users, scenario which has been analyzed in [34] and [55], an upper bound can be derived for the mean SIR using ZF precoding in JT CoMP. Using the expression for K_{IUI} as provided in Appendix 7.2.1 for $N_b > N_u \geq 2$, we obtain following expression:

$$\text{SIR}_{\max} \approx \frac{1}{4\pi^2\sigma_f^2 t_n^2} \cdot \frac{N_b}{N_u - 1} - \frac{N_b + 1}{N_u - 1}. \quad (4.43)$$

The distance between (4.42) and (4.43) reveals the potential for SIR enhancement, if the users' selection process considers the orthogonality among their channel vectors.

It should be clarified at this point, that expressions (4.42) and (4.43) do not consider any gains from resource allocation, the evaluation of which are not in the scope of this work. In an orthogonal frequency division multiple access (OFDMA) system, each user can be assigned a part of the spectrum in a way that his performance and the network performance can be optimized, as known from [108] and also shown in [109] for the multi-user downlink.

The signal model given in Section 4.2 for the impaired OFDM-based JT CoMP is valid for any OFDMA scheme. Using OFDMA in the downlink does not affect the signal structure of a user's received self-signal and the IUI. The ICI also has a same structure and statistical properties, as typically data are transmitted on all subcarriers, which is recommended for keeping frequency-flat distribution of the ICI power [88]. The degradation mechanisms due to multiple CFOs and SFOs, as described in our model, will be the same for any system using OFDM.

What indeed changes in OFDMA is the channel statistics for each user after resource allocation. Therefore, if intended to evaluate the overall performance of a coordinated multi-point system using OFDMA, the general mean power expressions (4.26), (4.31) and (4.37) would need to be evaluated for the actual users' channel statistics. This procedure practically implies a calculation of constants K_U , K_{IUI} and K_{ICI} .

In this section, the received power of a user was studied in relation to the interference from other users and other subcarriers, in a multi-cell multi-user downlink with cooperative base stations. Closed-form expressions and accurate approximations for all relevant terms were derived. Moreover, it was demonstrated that inter-user interference has the most relevant effect. Finally, the impact of the radio channel was investigated and analytical SIR expressions were derived for zero-forcing precoding.

4.4 Evaluation and numerical validation

In this section, analytical results of Section 4.3 are evaluated and verified by simulations. Based on those results, adequate requirements are determined for the base stations' oscillators in CoMP systems.

A JT CoMP scenario is considered, where a cooperation cluster of $N_b = 7$ base stations transmits jointly by using zero-forcing precoding to N_u terminals on the same time and frequency resource, with $N_b > N_u \geq 2$. Out-of-cluster interference is not considered.

At time instant $t = 0$, the base stations receive an update of the downlink channel matrix and compute a precoding matrix. This will be used during the following 10 ms, time at which a new channel update will be obtained and a new precoder will be calculated. This routine agrees with the current 3GPP LTE channel and precoder updating cycle [31]. As already mentioned in Section 4.2, it is assumed that the radio channel is perfectly estimated and available at the base stations at $t = 0$, whereas channel aging effects are not considered

either. Between updating instants, the phase of the local base stations' oscillators slowly drift away from each other because of the individual frequency offsets with respect to the ideal carrier frequency f_c . As a consequence, self-signal drops, IUI grows and overall the SIR drops with time. In a practical system, each user can use downlink pilot symbols to estimate and equalize its own CFO and avoid ICI enhancement. However, mobiles cannot stop the IUI from rising, because the degradation is caused jointly by all the misaligned base station oscillators.

The accuracy of an oscillator, Osc , typical specified in parts per million (ppm) or parts per billion (ppb), relates to the standard deviation of the resulting carrier frequency as $\sigma_f = \text{Osc} \cdot f_c$. The CFO variation over time is assumed to be slow enough to be considered static with respect to the OFDM signaling and precoder updating timescale. Here, Gaussian i.i.d. CFOs are randomly assigned to base stations and mobile users, all with zero mean and standard deviations given by σ_f and $\sigma_{f,j}$, respectively.

Typical 3GPP LTE parameters are used, specified in [31]. The broadband OFDM signal has $N_s = 2048$ subcarriers, separated by $\delta = 15$ kHz. The length of the cyclic prefix is 144 samples, resulting in OFDM symbols with a length of $N_g = 2192$ samples. The ideal carrier and sampling frequencies are $f_c = 2.65$ GHz and $\frac{1}{T} = 30.72$ MHz, respectively. The energy per data symbol is set to $E_s = 1$.

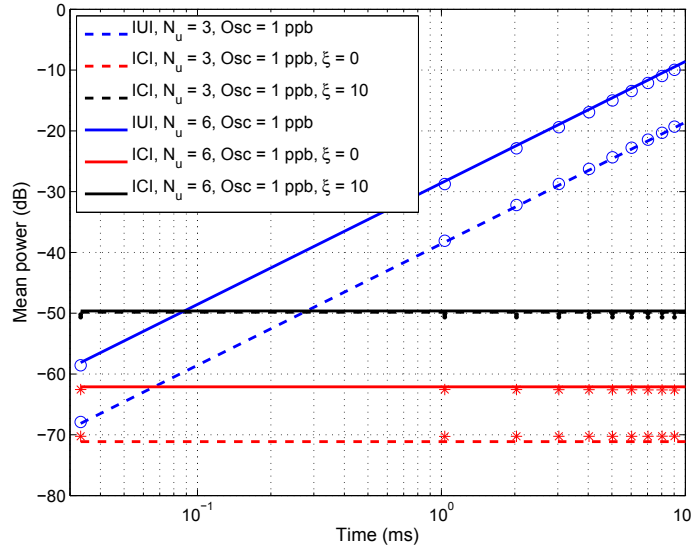


Figure 4.2: Mean power of inter-user and inter-carrier interferences in a Rayleigh fading channel. Here, 7 base stations serve 3 and 6 users, respectively. Analytical results (4.33) and (4.38) are shown by lines, while markers show respective numerical evaluations of (4.14) and (4.15).

Figure 4.2 depicts the mean power of the IUI and ICI over time passed from the last precoder update (in logarithmic scale), for 3 and 6 mobile users, a base station oscillator

accuracy of 1 ppb and Rayleigh fading channel conditions. The curves illustrate analytical results given by (4.33) and (4.38), whereas solid lines are used for depicting results for 3 users and dashed lines for 6 users, respectively. Markers show respective numerical evaluations of the mean power of (4.14) and (4.15) over 10^3 independent realizations of the MIMO channel matrix entries with $\sigma_h^2 = 1$ and of the bases' CFOs. Regarding the ICI, two scenarios are considered: a scenario with $\xi = 0$, i.e. perfectly synchronized mobile users in order to evaluate solely the ICI due to the base stations' CFOs (red) and a second scenario with unsynchronized mobiles, with a CFO accuracy of an order of magnitude lower than the one the base stations, i.e. $\xi = 10$ (black), where the total ICI is evaluated.

First of all, Figure 4.2 verifies the analytical expressions (including mathematical approximations) by numerical means. It is further observed that the IUI grows approximately with the square of time and that it increases with the number of users. Comparing the mean power levels of IUI (blue curves) with the ICI, both caused by the base stations' CFOs (red curves for $\xi = 0$), we see that independently of the number of users and for typical feedback delays between 2 ms and 10 ms, the IUI lies between 40 dB to 50 dB above the power of ICI. This clearly indicates that the IUI is significantly stronger than the ICI caused by the base stations' CFOs. Considering now the second scenario with non-perfectly synchronized mobile users ($\xi = 10$), it can be observed that the part of the ICI caused by the users' CFO overwhelms the ICI caused by the base stations' CFOs. According to (4.38), the (dominant) ICI due to a mobile user's CFO does not depend on the number of served users, which is reflected in the fact that the black curves in Figure 4.2 evaluating the total ICI for $\xi = 10$ almost overlap for the cases of 3 and 6 users. It is also interesting to observe that the IUI power level due to the cooperating base stations' CFOs is still around 20 dB to 30 dB (for 3 users) and 30 dB to 40 dB (for 6 users) higher than the total ICI power, considering typical feedback delays between 2 ms and 10 ms. These results clearly show that in the a cooperative network -even with typically non-perfectly synchronized mobile users- the main interference source lies in the base stations' CFOs.

Figure 4.3 and Figure 4.4 show the SIR over the time, as defined in (4.41), for $N_b = 7$ base stations serving jointly $N_u = 3$ and $N_u = 6$ mobile users, respectively, which is also the highest possible number for the Rayleigh fading channel. The influence of the base stations' oscillator accuracy is evaluated, and the corresponding ICI is neglected as it is significantly smaller than the IUI. Disregarding the ICI also means that the synchronicity level of the mobile users is not relevant, as it does not contribute the the IUI.

For the Rayleigh fading channel, the analytical expression (4.42) is compared with the ratio between the numerically evaluated mean power of (4.13) and (4.14) over 10^3 independent channel and CFO realizations, which validates our analysis including the accuracy of the mathematical approximations. Similarly, for the SIR upper bound expression, the analytical expression (4.43) is compared with results from numerical evaluation. From Figure 4.3 it is seen that a degradation of the base station oscillators' accuracy by one order of magnitude increases the IUI and thus decreases the SIR by around 20 dB. Furthermore,

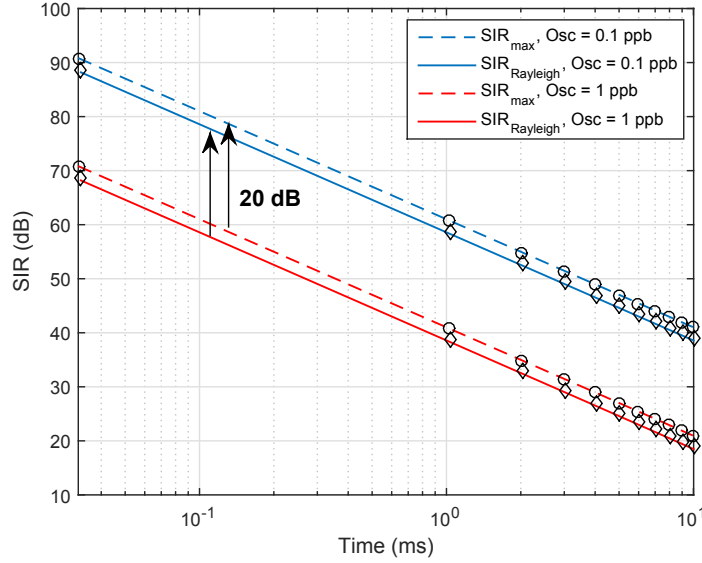


Figure 4.3: Mean SIR over time for Rayleigh fading channel and SIR upper bound. Here, 7 base stations using oscillators of accuracy given by Osc serve jointly 3 users. Analytical results are shown by lines, simulations by markers.

the SIR drops approximately quadratically with time, i.e. 20 dB per time decade. In terms of accuracy requirements, it is found that for reaching in average an SNR of 20 dB 10 ms after the precoder update, (free-running) oscillators of 1 ppb are needed.

Figure 4.5 illustrates the mean SIR as function of the number of users, which are served by 7 base stations at the same time and frequency resource, for a time instant of 10 ms after the most recent precoder update. Such a time delay is relatively large for a practical system and thus, these results should be interpreted more as a worst case rather than an average situation. Here, analytical results based on (4.41) for the Rayleigh fading channel and the SIR upper bound are verified by numerical simulations. It is observed that, given the same synchronization conditions, serving jointly more users results in a lower SIR compared to serving fewer users. It is also observed that, as the number of users grows, the distance between the SIR in Rayleigh fading and its upper bound becomes larger. Practically this means that, the more users are jointly served, the higher the potential benefits are if sets of jointly served users are appropriately formed, as already discussed in Section 4.3.5.

4.5 Model simplification and MSE analysis

As a starting point we consider the general model for the impaired joint transmission coordinated multi-point (JT CoMP) as given in Chapter 2, which is here specialized for the case of synchronization impairments among the distributed base stations. The model

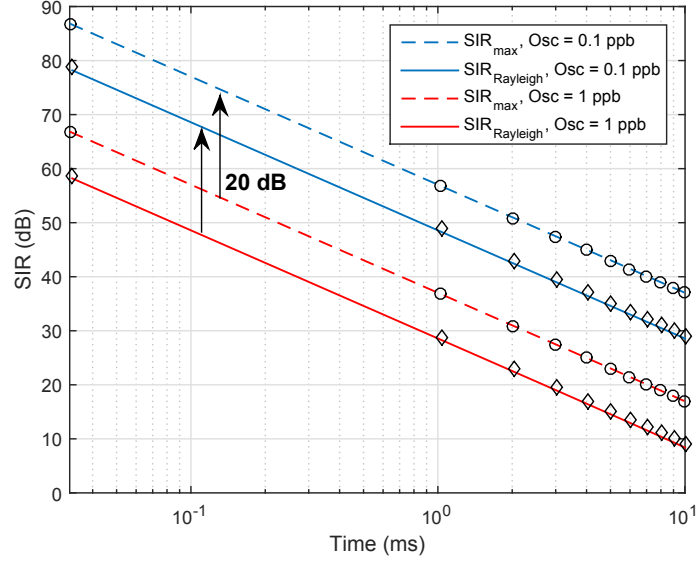


Figure 4.4: Mean SIR over time for Rayleigh fading channel and SIR upper bound. Here, 7 base stations using oscillators of accuracy given by Osc serve jointly 6 users. Analytical results are shown by lines, simulations by markers.

is used for derivation of expressions for the equivalent channel MSE, which are afterwards used for obtaining the mean SIR in the downlink. This simplified model provides within a certain range of validity, results very close to ones of the exact model of Section 4.2, as also verified by simulations.

It is known from [30] that in OFDM systems, the CFO cause a common phase error while the SFO a phase ramp on all subcarriers, which can be both estimated and compensated as part of the channel frequency response. Additionally, those impairments destroy orthogonality among the subcarriers and cause ICI, which is AWGN-like and is not easy to compensate [30]. It is also known that, when sampling and carrier frequency share the same reference, the impact of SFOs has been found to be very small compared to CFO and can be thus neglected. For JT CoMP using OFDM, the mechanisms generating ICI are similar to the ones for non-precoded transmission, therefore the above statements hold as well. However, as shown in Section 4.3, main limitations come from the IUI rather than from the ICI, which can be thus neglected. The main origin of this IUI lies in the CFOs of the distributed base stations, as mobile-side CFOs do not cause IUI.

We consider a distributed JT CoMP system where base stations use perfect channel knowledge for precoder calculation. Each base station is driven by its own local oscillator and has its own carrier frequency f_i and thus its own CFO ($f_i - f_c$), whereas the ideal carrier frequency is f_c . The CFO is modeled as a zero-mean random variable with the same variance σ_f^2 for all base stations (BSs). Focusing on the i^{th} transmitter, the frequency

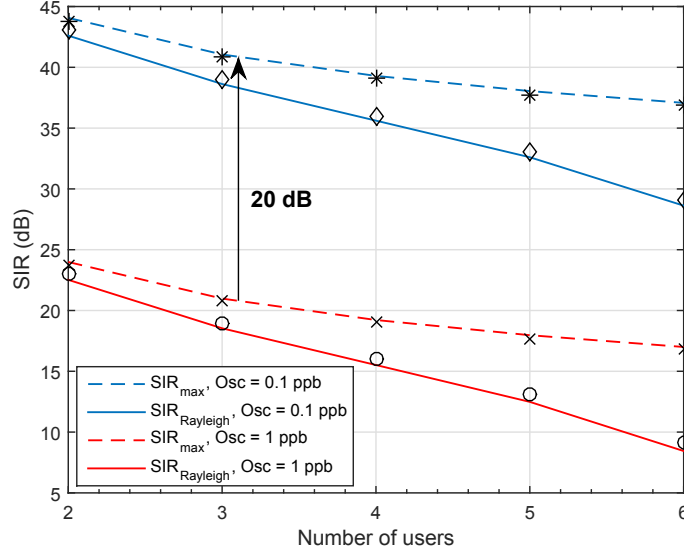


Figure 4.5: Mean users' SIR 10 ms after most recent precoder update, for the Rayleigh fading and upper bound. Here, 7 base stations serve jointly from 2 to 6 users. Analytical results are shown by lines, simulations by markers.

domain representation of its CFO is given by

$$\phi_i(t) = e^{j\theta_i(t)}, \text{ with } \theta_i(t) = 2\pi(f_i - f_c)t. \quad (4.44)$$

Expression (4.44) can be also obtained from (4.9) with $k = \nu$ and by using $\frac{1}{N_s} \frac{\sin(N_s x)}{\sin(x)} \approx 1$, which practically disregards the ICI. Perfect sampling is used, i.e. $T_i = T_j = T$, while mobile users are assumed to be perfectly synchronized with $f_j = f_c$. Note that base station index b has been here replaced with transmitter index i .

In the downlink of coordinated transmission, the phase drifts due to the CFOs apply to precoded data symbols before they are transmitted over the channel, as shown in Figure 4.1. We therefore introduce diagonal matrix $\Phi_t = \text{diag}(\phi_1(t), \dots, \phi_i(t), \dots, \phi_{N_b}(t))$ into the downlink equation and develop the main downlink equation as

$$\mathbf{y} = \mathbf{H}\Phi_t\mathbf{W}\mathbf{s} + \mathbf{n}. \quad (4.45)$$

Matrix Φ_t depends on the time instant t and is reset to zero with each precoder update. Residual phase terms can be considered as part of the channel and are captured by the following precoder calculation. Equation (4.45) is re-formulated as

$$\mathbf{y} = \mathbf{s} + \underbrace{\mathbf{H}(\Phi_t - \mathbf{I})}_{\triangleq \Delta_\Phi} \mathbf{W}\mathbf{s} + \mathbf{n} \quad (4.46)$$

where Δ_Φ can be interpreted as an *equivalent* channel error matrix due to the CFO. Matrix Φ_t is diagonal, thus the channel vector faced by transmission from the i^{th} base station (column i of \mathbf{H}) is multiplied with $\phi_i(t) - 1$. Entries of Δ_Φ are thus given by $\delta_{\phi,ji} = h_{ji}(\phi_i(t) - 1)$. Their mean power equals to $\mathbb{E}\{|\delta_{\phi,ji}|^2\} = \mathbb{E}\{|h_{ji}|^2\} \cdot \mathbb{E}\{|\phi_i(t) - 1|^2\}$, as h_{ji} and $\phi_i(t)$ are uncorrelated. The normalized MSE results into

$$\begin{aligned} \text{MSE}_\phi &= \mathbb{E}\{|\phi_i(t) - 1|^2\} \\ &= \mathbb{E}\{|\phi_i(t)|^2 - \phi_i(t) - \phi_i^*(t) + 1\} \\ &= \mathbb{E}\{2 - 2 \cdot \Re\{\phi_i(t)\}\} = \mathbb{E}\{2 - 2 \cdot \cos(\theta_i(t))\} = 2 - 2 \cdot \mathbb{E}\{\cos(\theta_i(t))\}. \end{aligned} \quad (4.47)$$

It has been used that $|\phi_i(t)|^2 = 1$. For small values of x , the second order Taylor series approximation $\cos(x) \approx 1 - \frac{x^2}{2}$ is accurate and yields

$$\text{MSE}_\phi \approx \mathbb{E}\{\theta^2(t)\}.$$

Considering expression (4.44), the MSE due to the CFO results into

$$\text{MSE}_\phi \approx 4\pi^2 \sigma_f^2 t^2, \quad \sigma_f t < 0.1. \quad (4.48)$$

Expression (4.48) reveals that the MSE is proportional to the CFO variance σ_f^2 and grows quadratic with time. The approximation error is desired to remain under 10 %, which means that for a feedback delay up to $t = 10$ ms, σ_f needs to be less than 10 Hz. This requires an oscillator accuracy of $\text{Oc} = \sigma_f / f_c = 4 \cdot 10^{-9}$, which is close to the 3GPP reference of $\text{Oc} = 5 \cdot 10^{-9}$. The resulting MSE is then around -17.5 dB.

Alternatively, we could also use the first order Taylor series approximation $e^{jx} \approx 1 + jx$ for $\phi_i(t)$ with

$$\phi_i(t) \approx 1 + j \theta_i(t) \quad \text{and} \quad \Phi_t \approx \mathbf{I} + j \Theta_t. \quad (4.49)$$

The diagonal matrix Θ_t is given by $\Theta_t = \text{diag}(\theta_1(t), \dots, \theta_i(t), \dots, \theta_{N_b}(t))$. Imposing matrix form of (4.49) into (4.45), the received signal becomes

$$\mathbf{y} \approx \mathbf{s} + j \mathbf{H} \Theta_t \mathbf{W} \mathbf{s} + \mathbf{n}. \quad (4.50)$$

The second term approximates the inter-user interference due to non-orthogonal transmission to different users, caused by imperfect synchronization among base stations. From (4.50) and (4.46) it is straightforward that $\Delta_\Phi \approx j \mathbf{H} \Theta_t$ and $\delta_{\phi,ji} \approx j h_{ji} \theta_i$. As h_{ji} and θ_i are uncorrelated and both zero-mean, we have $\mathbb{E}\{|\delta_{\phi,ji}|^2\} = \sigma_h^2 \sigma_\theta^2$. Finally, the normalized MSE reaches the same result as in (4.48).

Figure 4.6 evaluates MSE due to the base stations' CFOs, both by the exact expression (4.47) as well as by the approximation (4.48). The exact expression is numerically evaluated over 10^4 i.i.d. Gaussian-distributed CFOs with zero mean and a variance σ_f^2 equal to the

oscillators' root mean square (RMS) value, i.e. $\sigma_f = \text{Oc} \cdot f_c$, where Oc characterizes the oscillators' accuracy with respect to the carrier frequency. It can be observed that by reducing the oscillator accuracy by one order of magnitude, the MSE increases by 20 dB, while doubling the time increases the MSE by 6 dB.

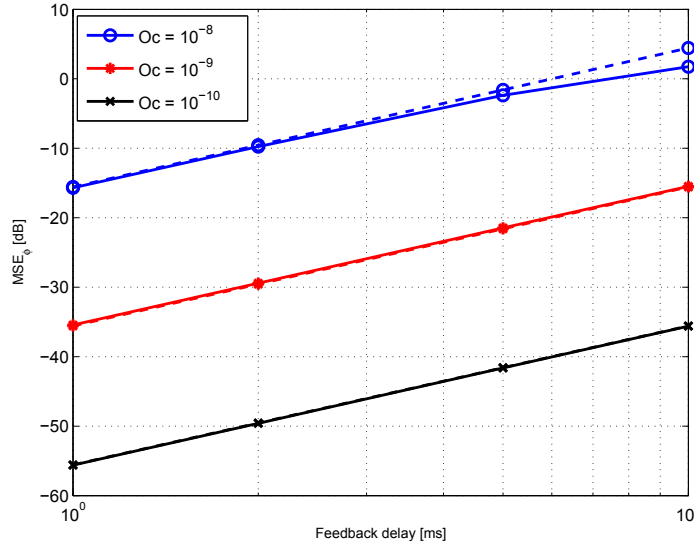


Figure 4.6: Equivalent channel MSE due to oscillator CFO. *solid*: numerical evaluation of exact expression (4.47); *dashed*: analytical approximation (4.48).

4.6 Recommendations for CoMP system design

In this section, synchronization requirements for OFDM-based JT CoMP and ways to meet them are discussed. It can be seen from Figure 4.5 that, if e.g. an average SIR of at least 25 dB shall be guaranteed at all times between precoder updates and for the maximum allowed number of users, then the accuracy of the base stations' oscillators needs to be 0.1 ppb. Note that base stations typically contain already sufficiently precise OCXOs, however, their frequencies need to be locked to a common reference, which can be e.g. provided by the GPS. The satellites of the GPS system are equipped with Rubidium or Cesium oscillators, thus providing a highly reliable reference below $1\mu s$ in terms of absolute time error [110]. At each base station, equipped with a GPS receiver, the local oscillator will be then phase-locked to the incoming time signal from the GPS and will also follow its carrier frequency. Practical synchronization of distributed base stations in a JT CoMP testbed is described in [102].

Other schemes -also for base stations with no GPS connection- suggest that base stations are connected via Ethernet to the backhaul network, over which and by using a network

synchronization protocol such as IEEE1588 [111], a common clock signal can be provided to them. This reference signal can be then used for time synchronization, as well as for recovering a carrier frequency reference at each site. However, the precision of such protocols could be probably not sufficient for JT CoMP. Therefore, additional over-the-air synchronization procedures can be deployed, such as the protocol proposed in [103]. Distributed base stations incorporate a suitable frequency estimator, e.g. the ML-based estimator described in [30], and additionally exchange pilots for enhancing the network synchronicity. The protocol can be also applied to networks with a large number of nodes and does not require expensive oscillators.

The analytical and numerical results provided up to here describe the signal distortion and evaluate the corresponding performance degradation of a JT CoMP system using OFDM. State-of-the art systems also consider OFDMA techniques, where frequency resources can be assigned in a flexible way to multiple users. It is well-known that sophisticated resource allocation schemes offer significant gains, as shown in [108] and references therein. What indeed changes in OFDMA is the channel statistics that users observe, which is now improved through efficient resource allocation. Therefore, the signal and interference power terms as analyzed in Section 4.3 should be for an OFDMA system only understood as a worst-case scenario performance, while for determining the actual performance, one would need to consider the channel statistics after deploying a specific resource allocation scheme.

4.7 Summary of Chapter 4

In this chapter, an exact signal model for multi-user multi-cell systems using OFDM was derived, if transmissions are impaired by individual carrier and sampling frequency offsets on every transmitter and receiver branch. From there it is shown that the impact of the sampling offsets is much smaller than the impact of the carrier frequency offsets. The model was specialized to the downlink of systems with cooperative base stations, where precoding with the inverse of the channel matrix was considered. It was analyzed how carrier frequency misalignments among the cooperative base stations decrease the power of the self-user's signal and cause inter-user and inter-carrier interference. Closed-form exact expressions and accurate approximations were derived for the mean power of the above signals and it was shown that for practical purposes, the inter-user interference dominates on the inter-carrier interference. Analytic expressions were also derived for the mean SIR, for Rayleigh fading channel conditions as well as an upper bound for cooperative systems. The mean SIR decreases quadratically with time and is inversely proportional to the variance of the base stations' frequency offsets. It also grows with the number of base stations and drops with the number of users jointly served by them on the same time and frequency resource. Furthermore, the model was simplified for the case of individual

carrier offsets at the distributed base stations and closed-form expressions were derived for the equivalent channel MSE.

From a practical perspective, when a high SIR is targeted, synchronization requirements can be fulfilled by using at the base stations OCXOs locked to either a precise GPS reference, or to a clock signal provided through the backhaul network.

5 Channel Impairments and Mitigation Techniques for CoMP

In this chapter, the signal model for the impaired coordinated multi-point (CoMP) downlink is developed for including channel aging, channel estimation and channel state information (CSI) feedback quantization and is used for deriving analytical signal-to-interference ratio (SIR) expressions. It is shown that even for low mobilities, the SIR drops quickly with the feedback delay time. A time-domain CSI feedback compression scheme is proposed for CoMP, which takes into account noise and interference. The number of bits required for feedback grows linearly with the signal-to-noise ratio (SNR) in dB, as also required by information theory. Evaluation of the feedback compression scheme using spatial channel model extended (SCME) as well as data from multi-cell channel measurements indicates that in a system with 20 MHz bandwidth, CSI from all relevant cells around a terminal can be provided using few kbits per reporting interval. A novel channel prediction method based on a Doppler-delay channel model and a high-resolution (HR) algorithm for extracting the major Doppler frequency components is further proposed. Evaluation over the SCME as well as with measured channel data shows that the channel mean square error (MSE) can be reduced by roughly 10 dB for typical feedback delays between 2 and 10 ms, which directly translates into SIR gains in CoMP. System-level simulations showed that an SIR enhancement around 10 dB can be achieved, also depending on the number of base stations and mobile users within the cooperation cluster.

5.1 Analysis of JT CoMP with channel impairments

As introduced in Chapter 2, there are unavoidable channel impairments in real-world systems, causing a systematic mismatch between the precoder applied to the downlink signals and the channel over which the transmission is realized. In frequency division duplex (FDD) systems, terminals estimate the channel and provide quantized CSI to the base stations (BSs), as illustrated in Figure 5.1. In time division duplex (TDD) systems, CSI for downlink precoding is obtained by channel estimation at the BSs in the reverse link, which is operated at earlier time. In both cases, the base stations have estimates of the channel rather than a perfect knowledge of it, with noise, interference and quantization contributing to uncertainty. In addition, there is a delay, equal to the time between when the channel is observed and when the resulting estimate is used for precoding. This delay is mainly generated by the transmission over the air, by CSI exchange between base stations over the

backhaul network and by the required computational time. These sources of delay add up to an overall delay, which will be from here on termed as *feedback delay*. In [64], the individual contributions to the feedback delay were evaluated in a multi-cellular experimental system. Results indicated that the main contribution to the delay is due to terminal-side procedures, mainly multi-cell channel estimation and CSI packet construction. The CSI reconstruction at the BSs is also a source of delay, while transmission of the compressed CSI over the air is in relative means a fast part of the loop. Considering channel time variance due to the users' mobility, the channel state information at the transmitter (CSIT) becomes outdated when used for precoder calculation, effect also known as *channel aging*.

In this section, the general model for impaired joint transmission coordinated multi-point (JT CoMP), which has been presented in Chapter 2, is specialized to include channel aging, channel estimation and CSI feedback quantization. Power analysis of the users' self-signal and inter-user interference (IUI) leads to closed-form SIR expressions. The downlink signal model is simplified by introducing MSE expressions, provided for each impairment separately. In this section, the effect of channel impairments is investigated separately, therefore the network will be assumed to be perfectly synchronized in terms of sampling and carrier frequency.

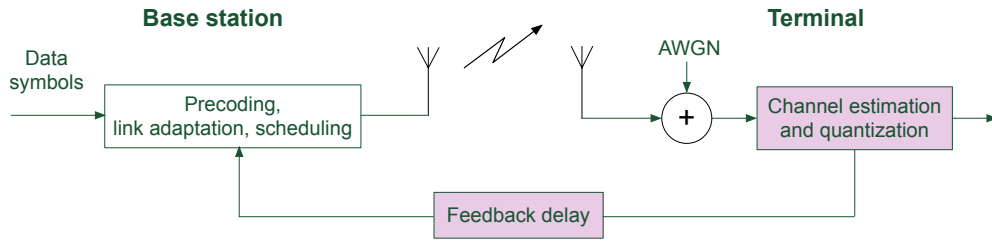


Figure 5.1: Sources of mismatched precoding in an FDD system: channel estimation, CSI quantization and channel aging during the feedback delay and CSI exchange delay over the backhaul network.

5.1.1 Signal model

In what follows, the effects of channel aging, channel estimation and CSI feedback quantization will be modeled separately, before they are integrated into a unifying JT CoMP signal model.

Channel aging

Considering mobile users and thus a time-variant radio channel, a channel observation at an arbitrary time instant $t = 0$ will be outdated if used at a later time for data precoding (or for link adaptation, resource allocation etc.). Any time-variant channel coefficient h_t at time t can be modeled as

$$h_t = h_0 + \delta_t, \quad (5.1)$$

where h_0 denotes the channel at a reference time instant $t = 0$ and δ_t the channel evolution since then. When observing the mobile radio channel for time intervals equal to the feedback delay, we can safely assume that large-scale parameters such as path loss and shadow fading will not change. Therefore, any channel variation will only be due to small-scale fading [84]. Considering large-scale parameters to be constant, we may assume, without loss of generality, that their effect appears through the SNR. Based on the analysis in [70], channel h_t can be modeled by

$$h_t = \rho_t h_0 + v_t, \quad (5.2)$$

where ρ_t is the autocorrelation function of the channel h_t . The complex Gaussian variable v_t has zero mean and variance $(1 - \rho_t^2)\sigma_h^2$ and is uncorrelated to the channel h_0 . Considering Jake's fading model we have $\rho_t = J_0(2\pi f_D t)$, where J_0 is the zero-order first kind Bessel function and $\rho_t \in [-1, 1]$. The maximum Doppler frequency f_D according to the terminals' velocity v and the radio frequency f_c is given by $f_D = f_c \cdot v/c$ (c denotes the speed of light). Combining (5.1) and (5.2), the channel deviation δ_t can be formulated as

$$\delta_t = h_t - h_0 = (\rho_t - 1)h_0 + v_t. \quad (5.3)$$

Extending the model to multiple-input multiple-output (MIMO) transmission and assuming the same maximum Doppler spread for all terminals, expressions (5.1), (5.2) and (5.3) can be formulated in matrix notation as follows:

$$\mathbf{H}_t = \mathbf{H}_0 + \mathbf{\Delta}_t, \quad (5.4)$$

$$\mathbf{H}_t = \rho_t \mathbf{H}_0 + \mathbf{V}_t, \quad (5.5)$$

and

$$\mathbf{\Delta}_t = (\rho_t - 1)\mathbf{H}_0 + \mathbf{V}_t. \quad (5.6)$$

Channel estimation and CSI quantization

Channel estimation and quantization are performed at time instant $t = 0$ and can be modeled as

$$\hat{\mathbf{H}}_0 = \mathbf{H}_0 + \mathbf{E} + \mathbf{Q}, \quad (5.7)$$

where \mathbf{E} and \mathbf{Q} are channel error matrices due to channel estimation and quantization, respectively. Their entries are modeled as independent and identically distributed (i.i.d.) zero-mean random variates with variance σ_e^2 and σ_q^2 , respectively. Entries of \mathbf{E} can be modeled as complex Gaussian distributed, while entries of \mathbf{Q} are uniformly distributed within the interval determined by the quantization step. The resulting (non-ideal) zero-

forcing (ZF) precoder is

$$\hat{\mathbf{W}}_0 = \hat{\mathbf{H}}_0^H (\hat{\mathbf{H}}_0 \hat{\mathbf{H}}_0^H)^{-1}, \quad (5.8)$$

while the ideal ZF precoder referring to noise-free and non-quantized channel estimates at time instant $t = 0$ is given by

$$\mathbf{W}_0 = \mathbf{H}_0^H (\mathbf{H}_0 \mathbf{H}_0^H)^{-1}. \quad (5.9)$$

Signal model for JT CoMP including all channel impairments

The downlink system equation as formulated in (2.6) of Chapter 2, in the presence of channel aging, channel estimation and quantization takes the form

$$\mathbf{y} = \mathbf{H}_t \hat{\mathbf{W}}_0 \mathbf{s} + \mathbf{n}. \quad (5.10)$$

By imposing (5.5) and (5.8) into (5.10) and considering the inverse relation between $\hat{\mathbf{H}}_0$ and $\hat{\mathbf{W}}_0$, the MIMO downlink equation becomes

$$\mathbf{y} = \rho_t \mathbf{s} + \mathbf{V}_t \hat{\mathbf{W}}_0 \mathbf{s} - \rho_t (\mathbf{E} + \mathbf{Q}) \hat{\mathbf{W}}_0 \mathbf{s} + \mathbf{n}. \quad (5.11)$$

Focusing on an arbitrary user j , its received signal is given by

$$y_j = s_j \underbrace{\left(\rho_t + \sum_{b=1}^{N_b} (v_{jb} - \rho_t(e_{jb} + q_{jb})) \hat{w}_{bj} \right)}_{\text{self-signal}} + \underbrace{\sum_{\substack{u=1 \\ u \neq j}}^{N_u} s_u \sum_{b=1}^{N_b} (v_{jb} - \rho_t(e_{jb} + q_{jb})) \hat{w}_{bu}}_{\text{inter-user interference}} + n_j. \quad (5.12)$$

The first term on the right-hand side of (5.12) describes the user's self-signal. If precoded user-specific pilot symbols are used, each user will be able to estimate and equalize the (precoded) channel and detect its self-signal components. The second term is IUI due to channel aging, channel estimation and quantization. It is to be noted that at least two mobile users must be simultaneously served on a frequency resource, i.e. $N_u \geq 2$, so that the second term in (5.12) becomes effective. All math can of course be applied also to a single user. The IUI term due to estimation and quantization errors is multiplied with the correlation factor ρ_t , which shows that its magnitude is maximized for $t = 0$, when $\rho_0 = 1$, and decreases with time.

Expression (5.12) is in line with the general expression (2.7). Here, channel error elements of user j are given by $\delta_{jb} = v_{jb} + \rho(e_{jb} + q_{jb})$, while ρ_t acts as a gain factor of the self-signal's first component. Note that imperfect precoding based on observations at $t = 0$ affects the precoder calculation in (5.12), while in the general model of Chapter 2, perfect precoding was assumed for $t = 0$ and the effect of channel estimation and quantization was modeled by the error of the channel used for transmission.

5.1.2 Power analysis of self-signal and inter-user interference

In the sequel, we calculate the mean power of self-signal and IUI, first due to each of the channel impairments separately, and provide expressions for the mean SIR for the Rayleigh fading channel as well as an upper bound for the mean SIR. Afterwards, we provide a SIR expression for the more general case, where channel aging, channel estimation and quantization are included and investigate the influence of parameters as mobility, feedback delay and channel estimation accuracy onto the SIR, as well as the resulting requirements for JT CoMP.

1. *Channel aging:* Focusing first on channel aging, we disregard channel estimation and quantization, i.e. use $e_{jb} = q_{jb} = 0$ and obtain $\hat{w}_{bj} = w_{bj}$. Hence, (5.12) becomes

$$y_j = s_j \left(\rho_t + \sum_{b=1}^{N_b} v_{jb} w_{bj} \right) + \sum_{\substack{u=1 \\ u \neq j}}^{N_u} s_u \sum_{b=1}^{N_b} v_{jb} w_{bu} + n_j. \quad (5.13)$$

Following the analysis of Section 2.3 for $N_u \geq 2$ users, the mean power of self-signal (\check{s}_j) and IUI (\bar{s}_j) is found equal to

$$\mathbb{E} \{ |\check{s}_j|^2 \} = E_s \cdot (\rho_t^2 + (1 - \rho_t^2) \cdot \sigma_h^2 \cdot \mathbb{E} \{ \lambda^{-1} \}) \quad (5.14)$$

and

$$\mathbb{E} \{ |\bar{s}_j|^2 \} = E_s \cdot (N_u - 1) \cdot (1 - \rho_t^2) \cdot \sigma_h^2 \cdot \mathbb{E} \{ \lambda^{-1} \}. \quad (5.15)$$

As the mean value of the inverse eigenvalues of matrix $\mathbf{H}\mathbf{H}^H$ is the same for each one of its eigenvalues if they are not sorted, notation $\mathbb{E} \{ \lambda^{-1} \}$ is here used for all eigenvalues $\lambda_u \forall u \in \{1, \dots, N_u\}$. For a Rayleigh fading channel it has been shown in Section 2.3 that

$$\mathbb{E} \{ \lambda^{-1} \} = \frac{1}{\sigma_h^2 (N_b - N_u)}, \quad N_b > N_u.$$

Using this result and building the quotient between (5.14) and (5.15), the mean SIR becomes

$$\text{SIR}_{j,\text{Rayleigh}} = \frac{\rho_t^2}{1 - \rho_t^2} \cdot \frac{N_b - N_u}{N_u - 1} + \frac{1}{N_u - 1}, \quad N_b > N_u \geq 2. \quad (5.16)$$

For a channel matrix with orthogonal channel user's vectors with equal power, it has been also shown in Section 2.3 that $\mathbb{E} \{ \lambda^{-1} \} = \frac{1}{\sigma_h^2 N_b}$, yielding an upper bound for the mean SIR:

$$\text{SIR}_{j,\text{max}} = \frac{\rho_t^2}{1 - \rho_t^2} \cdot \frac{N_b}{N_u - 1} + \frac{1}{N_u - 1}, \quad N_u \geq 2. \quad (5.17)$$

2. *Channel estimation and CSI quantization:* Secondly, we focus on time instant $t = 0$ and consider only channel estimation and quantization effects, i.e. $\rho_t = 1$ and $v_{jb} = 0$. The effect of channel estimation and quantization is then maximized, while for $t > 0$ the

IUI decreases because of $\rho_t < 1$. The j^{th} user then receives

$$y_j = s_j \left(1 - \sum_{b=1}^{N_b} (e_{jb} + q_{jb}) \hat{w}_{bj} \right) - \sum_{\substack{u=1 \\ u \neq j}}^{N_u} s_u \sum_{b=1}^{N_b} (e_{jb} + q_{jb}) \hat{w}_{bu} + n_j. \quad (5.18)$$

Following the same mathematical steps as in Section 2.3, the mean inverse eigenvalue is found equal to

$$\mathbb{E} \{ \lambda^{-1} \} = \frac{1}{(\sigma_h^2 + \sigma_e^2 + \sigma_q^2)(N_b - N_u)}, \quad N_b > N_u \geq 2 \quad (5.19)$$

for the Rayleigh fading channel and

$$\mathbb{E} \{ \lambda^{-1} \} = \frac{1}{(\sigma_h^2 + \sigma_e^2 + \sigma_q^2)N_b}, \quad N_u \geq 2 \quad (5.20)$$

for a channel with orthonormal user's vectors, respectively. If the mean power of the channel estimation and quantization errors is small enough compared to the mean channel power, which is targeted and typically fulfilled in practical systems, we can approximate

$$\sigma_h^2 + \sigma_e^2 + \sigma_q^2 \approx \sigma_h^2$$

and reformulate (5.19) as (5.20):

$$\mathbb{E} \{ \lambda^{-1} \} \approx \frac{1}{\sigma_h^2(N_b - N_u)} \quad \text{and} \quad \mathbb{E} \{ \lambda^{-1} \} \approx \frac{1}{\sigma_h^2 N_b}. \quad (5.21)$$

We use (5.21) for calculating the mean power of self-user signal and IUI, given in (5.18), and reach a mean SIR of

$$\text{SIR}_{j,\text{Rayleigh}} \approx \frac{\sigma_h^2}{\sigma_e^2 + \sigma_q^2} \cdot \frac{N_b - N_u}{N_u - 1} + \frac{1}{N_u - 1}, \quad N_b > N_u \geq 2 \quad (5.22)$$

and

$$\text{SIR}_{j,\text{max}} \approx \frac{\sigma_h^2}{\sigma_e^2 + \sigma_q^2} \cdot \frac{N_b}{N_u - 1} + \frac{1}{N_u - 1}, \quad N_u \geq 2. \quad (5.23)$$

3. Channel aging, estimation and CSI quantization: Finally, we provide an SIR expression including channel aging, channel estimation and feedback quantization effects. Starting from and using the same mathematical arguments as above, it is straightforward to reach following expressions for the mean SIR:

$$\text{SIR}_{j,\text{Rayleigh}} \approx \frac{1}{\frac{1-\rho_t^2}{\rho_t^2} + \frac{\sigma_e^2 + \sigma_q^2}{\sigma_h^2}} \cdot \frac{N_b - N_u}{N_u - 1} + \frac{1}{N_u - 1}, \quad N_b > N_u \geq 2. \quad (5.24)$$

$$\text{SIR}_{j,\max} \approx \frac{1}{\frac{1-\rho_t^2}{\rho_t^2} + \frac{\sigma_e^2 + \sigma_q^2}{\sigma_h^2}} \cdot \frac{N_b}{N_u - 1} + \frac{1}{N_u - 1}, \quad N_u \geq 2. \quad (5.25)$$

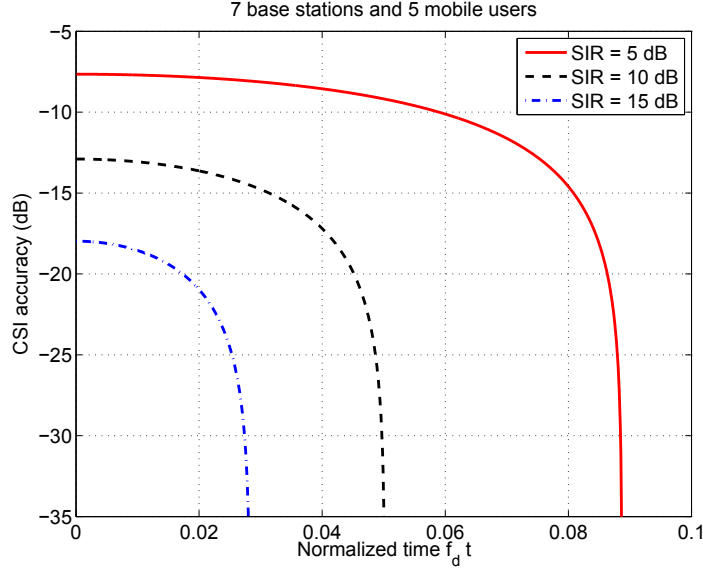


Figure 5.2: Required CSI accuracy after channel estimation/quantization vs. normalized feedback time, for attaining certain mean SIR levels in JT CoMP with 7 base stations and 5 users, in a Rayleigh fading channel, according to (5.24).

Figure 5.2 evaluates expression (5.24) for 7 base stations serving jointly 5 mobile users by ZF precoding over the Rayleigh fading channel. Here, the required CSI accuracy after channel estimation and quantization ($\frac{\sigma_e^2 + \sigma_q^2}{\sigma_h^2}$) is evaluated vs. the normalized feedback delay ($f_d t$). Each curve corresponds to a certain average SIR level at the receiver. For example, if the CSI accuracy lies at -20 dB, and in order to attain a final mean SIR of 15 dB, the normalized time must be under 0.02, which for a pedestrian speed of 3 km/h translates into 2.7 ms, which is challenging for a feedback delay time. The requirements as obtained from Figure 5.2 reveal that for supporting higher mobilities in CoMP, a mitigation mechanism will be needed for compensating the effect of channel outdated. The asymptotic behavior of the curves means that, given an error due to either estimation and quantization or channel aging, there will be a certain maximum SIR that can be achieved, even if the other impairment is zero. It is intuitive that for very short delays, the SIR is mainly determined by the channel estimation and quantization accuracy, while for larger delays the influence of the estimation and quantization error becomes smaller until it is minimized.

From further evaluation of expression (5.24) with respect to (w.r.t.) system parameters, practical requirements can be extracted for CoMP. For example, given a certain estimation and quantization accuracy, the maximum tolerable feedback delay, i.e. feedback reporting

frequency, can be obtained, also depending on the mobile users' mobility. The other way round, the required CSI accuracy, i.e. overhead for pilot symbols and quantization bits can be determined, if for a given feedback delay and users' mobility, a certain SIR is desired.

In [106], a simple system design methodology has been provided, which considers vital constraints in the specification of cellular systems with base station coordination. There, it is described how to use a variable orthogonal frequency division multiplexing (OFDM) pilot spacing according to the fastest user in a cluster, which shall also depend on the maximum tolerable feedback delay, so that a target SIR is still guaranteed.

5.1.3 Model simplification and MSE analysis

Here, the signal model of the previous section is simplified and the channel impairments' effect is captured and described by the normalized channel MSE. For channel errors due to aging, estimation and quantization, MSE expressions are provided.

Channel aging

Expression (2.14) provides the mean SIR that a user observes when served by ZF precoding under Rayleigh fading channel conditions and in the presence of impairments:

$$\text{SIR}_{j,\text{Rayleigh}} = \frac{1}{\text{MSE}_j} \cdot \frac{N_b - N_u}{N_u - 1} + \frac{1}{N_u - 1}, \quad N_b > N_u \geq 2.$$

Comparing this SIR expressions with (5.16), one can see that the MSE due to channel aging is given by

$$\text{MSE}_t = \frac{\mathbb{E}\{|v_t|^2\}}{\mathbb{E}\{|\rho_t h_0|^2\}} = \frac{1 - \rho_t^2}{\rho_t^2}. \quad (5.26)$$

The same result can be also obtained by comparing the SIR upper bound expressions (5.17) and (2.17).

In order to gain insight into how this MSE depends on essential parameters, we simplify the correlation coefficient ρ_t . It is known that the Bessel function can be defined by the Taylor series expansion [112]. For small arguments $x = 2\pi f_D t$, it can be very well approximated by the second-order polynomial $J_0(x) \approx 1 - 0.25x^2$, which is used in (5.26) and leads to

$$\text{MSE}_t(x) \approx 0.5x^2 \cdot \frac{1 - 0.125x^2}{(1 - 0.25x^2)^2}. \quad (5.27)$$

The second-order Taylor series expansion at $x = 0$

$$\frac{1 + \alpha x^2}{(1 - \beta x^2)^2} \approx 1 + (\alpha + 2\beta)x^2 \quad (5.28)$$

is applied to the fractional part at the right-hand side of (5.27) and the MSE reaches

$$\text{MSE}_t(x) \approx 0.5x^2 + 0.1875x^4. \quad (5.29)$$

For $x \ll 1$, the second term on the right-hand side of (5.29) is much smaller than the first term and can be thus neglected. If the maximum allowed error is set to 10 % with respect to the exact MSE expression (5.26), we can use

$$\text{MSE}_t \approx \begin{cases} 2\pi^2(f_D t)^2, & f_D t < 0.1 \\ 2\pi^2(f_D t)^2 + 3\pi^4(f_D t)^4, & 0.1 \leq f_D t < 0.2 \end{cases} \quad (5.30)$$

For the range of validity of (5.30) this means that, considering a maximum feedback delay of $t = 10$ ms, the second order approximation can be used for velocities up to $v = 3.7$ km/h (carrier frequency is $f_c = 2.65$ GHz) and the MSE is then around -18 dB. The fourth order approximation can be used for up to $v = 8$ km/h, while for larger velocities or feedback delays, higher order approximations are required.

Figure 5.3 evaluates the MSE due to channel aging according to the exact expression (5.26) (analytically and numerically) and approximation (5.30), for a terminal velocity of $v = 3, 6$ and 9 km/h and feedback delay up to 10 ms. For numerical evaluation, 10^4 i.i.d. Rayleigh channel initializations were used and time evolution was observed over the feedback delay time, and $\mathbb{E}\{|v_t|^2\}$ and ρ_t were statistically evaluated. As observed in Figure 5.3, doubling the feedback delay or velocity increases the MSE by around 6 dB.

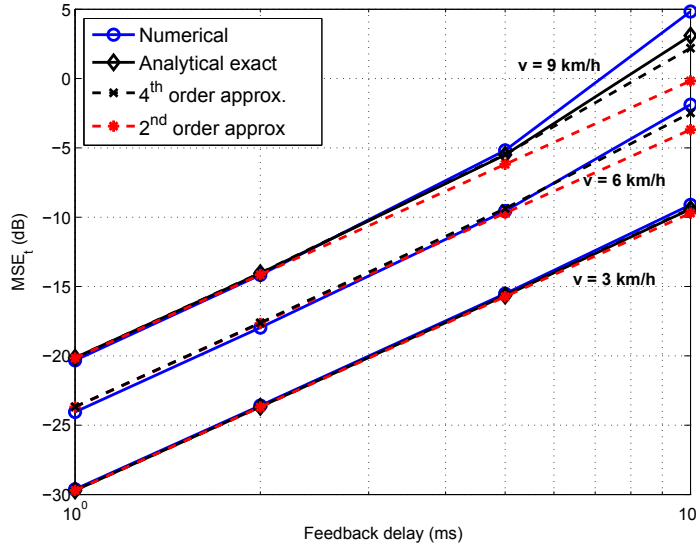


Figure 5.3: MSE due to channel aging according to numerical evaluation and exact analytic expression (5.26), second and fourth order approximation (5.30).

Channel estimation and CSI quantization

The MSE due to channel estimation at $t = 0$ can be defined from (5.22) as

$$\text{MSE}_e = \frac{\sigma_e^2}{\sigma_h^2}. \quad (5.31)$$

In OFDM systems the channel is typically estimated by interpolation over channel observations at pilot tones. The mean power of the channel estimation error σ_e^2 is equal to the mean additive white Gaussian noise (AWGN) power σ_n^2 , divided by the estimator gain G_{est} :

$$\sigma_e^2 = \frac{\sigma_n^2}{G_{\text{est}}}. \quad (5.32)$$

Using (5.32) in (5.31) results into

$$\text{MSE}_e = \frac{\text{SNR}}{G_{\text{est}}}. \quad (5.33)$$

In [113] it has been found that in a multi-path Rayleigh fading channel with L channel taps, when using OFDM with N_s subcarriers and separating pilots used for channel estimation by d subcarriers, the estimator gain G_{est} is given by:

$$G_{\text{est}} = \frac{N_s}{d \cdot L}. \quad (5.34)$$

Finally, as given in [114], for linear CSI quantization with B bits and with a quantization interval of $[-X_{\text{max}}; X_{\text{max}}]$, the mean power of the quantization error is

$$\sigma_q^2 = \frac{1}{3} \cdot X_{\text{max}}^2 \cdot 2^{-2B}. \quad (5.35)$$

Based on (5.22) and using (5.35), the MSE due to quantization is found

$$\text{MSE}_q = \frac{\sigma_q^2}{\sigma_h^2} = \frac{1}{3} \cdot \text{PAPR} \cdot 2^{-2B}. \quad (5.36)$$

The peak-to-average power ratio (PAPR) is defined as $\text{PAPR} = X_{\text{max}}^2 / \sigma_h^2$. As seen by (5.36), the MSE due to quantization depends on the number of bits used. Methods for adapting the quantization granularity and thus reducing the feedback overhead will be presented in the following section. A major objective is to minimize the overhead while maintaining the required precision of the CSI.

5.2 Feedback compression for JT CoMP

In this section, feedback requirements of JT CoMP systems and challenges in reducing the required feedback amount are discussed. A CSI feedback compression scheme is proposed for JT CoMP, which comprises of three steps: first, the strongest cells are clustered using a network-defined power threshold. Next, the strongest channel multi-path components to these base stations are selected after estimating the noise level and applying a corresponding threshold to the channel impulse responses (CIRs) in those cells. Adaptive quantization is used, so that the channel MSE remains sufficiently small. It is shown that in this way, the number of quantization bits grows linearly with the SNR in dB, as required by information theory. It is also shown that by considering the out-of-cluster interference level, the feedback overhead can be further reduced. Evaluation of the feedback compression mechanism using SCME as well as multi-cell channel measurements indicates that in a system with 20 MHz bandwidth, CSI from all relevant cells around a terminal can be provided using few kbits per reporting interval.

5.2.1 CSI feedback in multi-cellular JT CoMP systems

The potential of CoMP systems in eliminating the inter-cell interference and increasing the spectral efficiency is meanwhile well understood and has been proven by outdoor field trials [67]. However, some features of CoMP are not mature yet, such as the large amount of CSI feedback overhead, which also increases the backhaul traffic [115] and the overall feedback delay. The delay enhancement ensues from the fact that channel information has to be processed and organized into packets; the computational complexity and time of this process grows quadratically with the number of base stations to which CSI is reported [10]. Furthermore, CSI has to be transmitted over the air and over the backhaul network. The traffic and resulting delays have been studied in [10] for distributed architectures. It is evident that compressing efficiently the feedback information with a minimum cost of CSI accuracy is an essential goal for JT CoMP systems.

Implicit CSI is commonly used in frequency and space domains, for an overview of so-called *limited feedback* schemes, see [116]. By means of signal quality and channel rank, it characterizes an effective channel comprising of a fixed unitary precoder selected from a predefined codebook at the transmitter, the physical channel and an adaptive equalizer at the receiver. There is significant fluctuation of the mean power among the base station antennas in such a multi-cell multi-user channel unlike for single-cell MIMO. Unitary beamforming uses equal power for all links which is not appropriate for the multi-cell scenario. Thus, both amplitude and phase information are needed to maximize the desired signal and to minimize the interference.

It is intuitive that providing explicit CSI for multiple base stations increases the feedback overhead that mobile users need to report, compared to reporting implicit feedback. There are several ways to reduce multi-cell CSI feedback. Clearly, clustering reduces the feedback

since the CSI is limited to the most relevant cells. In [11], it has been demonstrated that BSs, for which the receive power at the terminal is below some threshold with respect to the strongest BS power, can be excluded from clustering and the terminals do not need to report CSI to them. However, close to the cluster edges, inter-cluster interference problems occur, replacing the former inter-cell interference problem. In [117] it has been shown that proper signal-to-leakage-and-noise ratio (SLNR)-based precoding techniques are able to deal with this cluster edge problems at the price of a small channel knowledge exchange between neighbor clusters. For mitigating this problem, a greedy dynamic clustering approach was introduced in [118], and it was found that it outperforms static clustering.

A further tool for reducing the amount of feedback is to compress efficiently the CSI. Towards this goal, the research community has mainly focused on codebooks for narrow-band channels [116], whereas in [119] Karhunen-Lo  ve transform (KLT) are suggested in order to remove the redundancy in frequency domain OFDM channel transfer functions. It was shown in [119] that time-domain transformations perform almost as well as KLT and are also more practical. It is noted that in OFDM, the channel estimated on pilot tones contains correlation among adjacent subcarriers. Therefore, it can be also described more compactly in the time domain by using discrete Fourier transform (DFT)-based algorithms [120].

Adaptive quantization of channel taps in the time domain, according to a desired operating point on the rate-distortion (RD) curve, is a further enabling technique for feedback reduction, according to [121]. A fundamental requirement in information theory is that the number of bits required for explicit CSI feedback grows linearly with the SNR in dB, in order to enable the full spatial multiplexing gain, as shown in [122]. In [123], a time-domain based feedback scheme has been proposed, which is in line with the information-theoretic results in [119]. The method focuses on the dominant multi-path propagation components, while it splits the feedback in long-term and short-term components to enhance redundancy removal. This approach also exploits the sparse nature of the multi-path propagation channel. Finally, in [124], further algorithms for the time-domain compression have been provided, refining the results of [123] with algorithms for detection of multiple path components, waterfilling-based bit loading across multiple channel taps and methods for combating the channel aging effects of the feedback by using channel prediction techniques.

5.2.2 A feedback compression scheme for JT CoMP

In the sequel, we present an adaptive feedback compression technique for the multi-cell scenario, which consists of following three steps, as shown in Figure 5.4: clustering, channel tap selection and adaptive quantization. According to the scheme, first the strongest cells are identified. For each cell, the CIR is obtained using a specific inverse discrete Fourier transform (IDFT). Afterwards, the noise level is estimated and weak taps are discarded by applying a threshold. Finally, adaptive quantization is used, based on the estimated

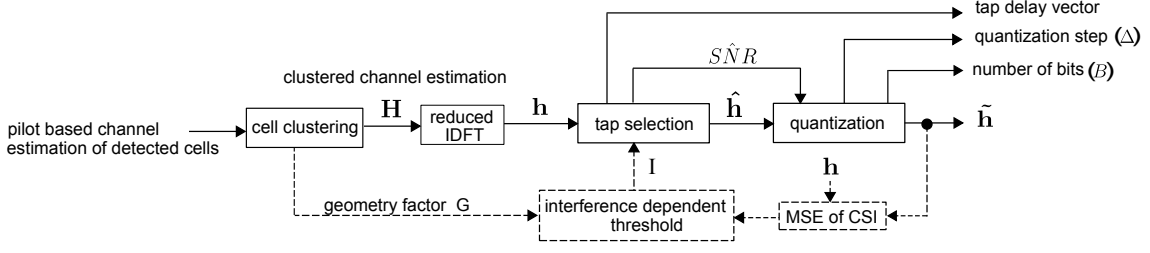


Figure 5.4: System model of the CSI feedback compression scheme. Solid lines connect the blocks for noise-based feedback compression; dashed lines connect the blocks for interference-aware compression.

SNR. It is ensured that the final channel MSE remains under a level related to AWGN and, eventually, out-of-cluster interference, as shown in blocks connected by dashed lines in Figure 5.4. Allowing a certain imperfection in CSI causes some IUI, which is of minor importance, as long as it remains lower than the existent out-of-cluster interference. In this way, by controlling the number of estimated channel taps and tolerating a certain channel error, the feedback is minimized. In what follows, it is shown that essential theoretical requirements can be met [122], while the compression of the proposed mechanism is quantified by using SCME [125] and field channel measurements. The methods and results presented here have been published in [7] and [11], where also a real-time implementation of the scheme has been demonstrated.

Clustering

First, we identify the strongest cells from a set of \mathcal{M} cells. The power β_p of the selected cells in the cluster \mathcal{M}' lies in a window, which is defined by the power β_m of the strongest cell and the clustering power threshold κ :

$$p \in \mathcal{M}' : \beta_m \geq \beta_p > \frac{\beta_m}{\kappa}. \quad (5.37)$$

In this way, feedback is limited to the most relevant cells. Assuming an ideal scenario, where interference is fully eliminated within the cluster, the resulting inter-cluster geometry \mathcal{G} due to the remaining out-of-cluster interference I_{out} is given by

$$\mathcal{G} = \frac{\beta_m}{I_{\text{out}}} = \frac{\beta_m}{\sum_{p \in \{\mathcal{M} \setminus \mathcal{M}'\}} \beta_p}. \quad (5.38)$$

Selection of strongest channel taps by AWGN removal

Figure 5.5 shows the procedure of estimating the most significant channel taps from the channel frequency response (CFR) and providing the (quantized) CIR. Considering an

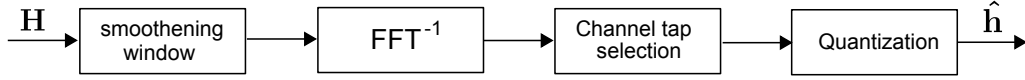


Figure 5.5: Channel tap estimation from frequency domain pilots: smoothing window, reduced IDFT matrix, channel tap selection by AWGN estimation and removal and adaptive quantization.

OFDM system with N_s subcarriers, terminals measure the $N_p \times 1$ CFR on N_p predefined pilot tones, denoted by \mathbf{H} . The corresponding time-domain representation by the $N_t \times 1$ vector \mathbf{h} is obtained by

$$\mathbf{h} = \mathbf{F}^{-1} \cdot \mathbf{H}. \quad (5.39)$$

Here, \mathbf{F}^{-1} denotes the $N_t \times N_p$ pseudo-inverse of the reduced IDFT matrix derived from the $N_s \times N_s$ DFT matrix \mathbf{F} by using only the elements in rows and columns corresponding to pilot and tap indexes, respectively, and computing the pseudo-inverse afterwards.

Applying a rectangular window in frequency domain, as this is typical for OFDM-based channel estimation, imposes a well-known signal spreading effect in the time domain, which affects each channel tap and increases the number of estimated non-zero channel taps. In order to reduce this undesired effect, before applying (5.39), we multiply the CFR with a so-called smoothing window, e.g. a *Hann* window, given by

$$w(p) = \frac{1}{2} \left(1 - \cos \left(\frac{2\pi(p-1)}{N_p} \right) \right), \quad p = 1, \dots, N_p.$$

Next, an iterative algorithm estimates the noise power σ_n^2 and selects the most relevant channel taps, as initially described in [126]. Channel taps are selected from \mathbf{h} , in which taps below a threshold ε , depending on the estimated noise power $\hat{\sigma}_n^2$, are discarded. The estimated noise power

$$\hat{\sigma}_n^2 = \mathbb{E} \{ |h_l|^2 \}, \quad \forall |h_l|^2 \leq \varepsilon \quad \text{and} \quad l = 1, \dots, N_t \quad (5.40)$$

is calculated by the values that lie under the threshold ε as

$$\hat{\sigma}_n^2 = \frac{1}{L} \sum_{l=1}^{N_t} |h_l|^2. \quad (5.41)$$

The tap index is denoted by l ; L is the number of taps above the threshold. In the first iteration, the noise power $\hat{\sigma}_n^2$ is calculated from all values. In the next step we update the threshold as

$$\varepsilon = \alpha \cdot \hat{\sigma}_n^2 \quad (5.42)$$

and discard all taps below it. It is suggested to set $4 \leq \alpha \leq 9$. Both steps are repeated until the estimation of $\hat{\sigma}_n^2$ converges, which happens after 4 to 5 iterations. Any tap $|h_l|^2$

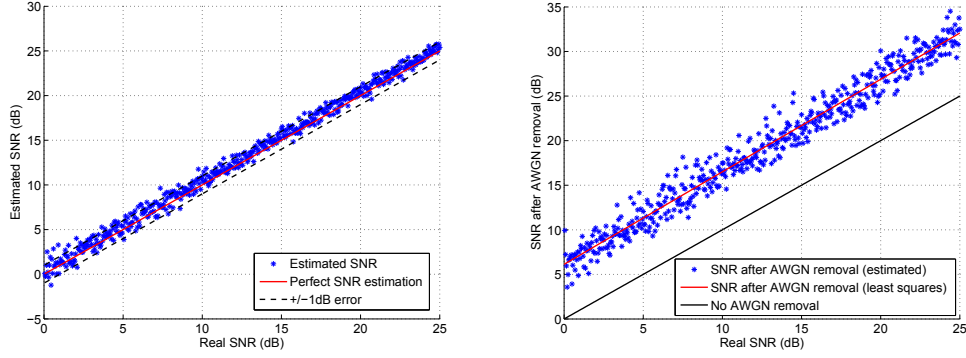


Figure 5.6: Left: Estimated SNR vs. real SNR after four iterations and by using $\alpha = 4$ for threshold calculation in (5.42). Right: An SNR gain of around 7 dB is observed after noise removal.

above ε is now a significant tap from a total of N_t taps, with

$$\hat{h}_l = \begin{cases} h_l & \text{for } |h_l|^2 > \varepsilon \\ 0 & \text{else} \end{cases} \quad (5.43)$$

The power of L selected taps and $N_t - L$ discarded taps is

$$P_{\text{sel}} = \sum_{l=1}^{N_t} |\hat{h}_l|^2 \quad (5.44)$$

and

$$P_{\text{dis}} = \sum_{l=1}^{N_t} |\hat{h}_l - h_l|^2 \quad (5.45)$$

respectively. As the L selected taps are superimposed by AWGN, a power term equal to $L/N_t \cdot P_{\text{dis}}$ is subtracted from P_{sel} and added to P_{dis} to estimate the SNR after channel tap selection properly

$$\hat{\text{SNR}} = 10 \cdot \log_{10} \left(\frac{P_{\text{sel}} - \frac{L}{N_t} \cdot P_{\text{dis}}}{1 + \frac{L}{N_t} \cdot P_{\text{dis}}} \right). \quad (5.46)$$

In (5.46), the numerator expresses the mean channel power and the denominator the mean noise power after channel tap selection, respectively.

Figure 5.6 (left) illustrates the estimated versus real SNR after four iterations using $\alpha = 4$. Most SNR values are estimated with an accuracy of ± 1 dB. On the right part of Figure 5.6, an SNR gain of around 7 dB after noise removal can be observed. The number of estimated taps L is depicted in Figure 5.7 for the SCME. It grows linearly with the SNR and runs into a floor, equal to the number of truly existing taps, which is 18 in the example channel considered here.

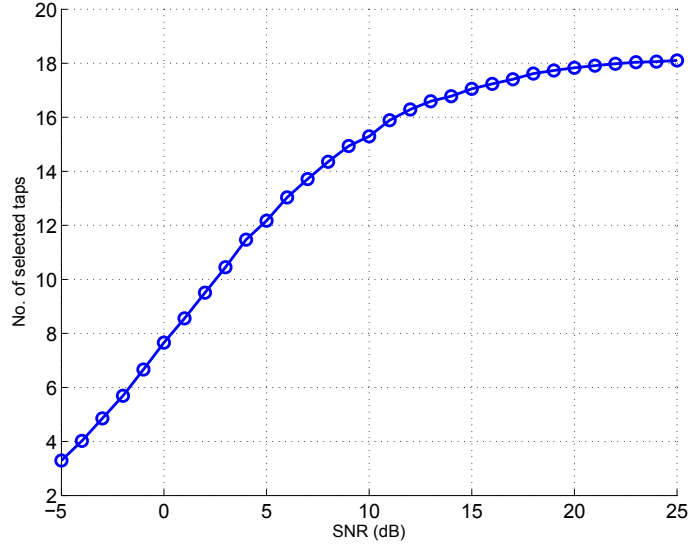


Figure 5.7: The number of estimated taps grows linearly with the SNR before reaching a ceiling at the level given by the number of actual taps, which is here 18.

Adaptive quantization based on the SNR

It is known that the RD-function provides the minimum distortion of a signal as a function of the data rate B_{RD} , i.e. the number of quantization bits per symbol [114]. The distortion D can be considered as a lower bound for the quantization error. For a memoryless Gaussian source with mean signal power σ_h^2 , the distortion $D(B_{\text{RD}})$ is given by

$$D(B_{\text{RD}}) = 2^{-2B_{\text{RD}}} \cdot \sigma_h^2. \quad (5.47)$$

Now we consider the quantization of the channel taps selected after application of the threshold. Here, the quantizer input will be already distorted, with respect to the ideal CIR, because of noise and tap selection, and will be given by (5.43). The SNR characterizing the input signal is estimated by (5.46). Logically, the distortion after quantization cannot be lower than the distortion before it, which is here modeled as AWGN with mean power σ_n^2 . Considering this optimistic scenario, we choose the corresponding operating point on the RD curve by setting $D(B_{\text{RD}}) = \sigma_n^2$ in (5.47), and the data rate becomes

$$B_{\text{RD}} \approx 0.17 \cdot \text{SNR}_{\text{dB}}. \quad (5.48)$$

Above, we used $\text{SNR}_{\text{dB}} = 10 \log_{10} (\sigma_h^2 / \sigma_n^2)$, measured in dB. As seen, the RD function requires that the number of quantization bits grows linearly with the input SNR in dB. Expression (5.48) provides the minimum required data rate, but no information about the quantization scheme in order to obtain the signal distortion given by (5.47).

A practical approach for reducing the number of quantization bits is to adapt the number of quantization bits B in a way that the MSE caused by quantization, denoted by MSE_q , is less or equal to the MSE of the signal at the quantizer's input, i.e. after tap selection, denoted by $\hat{\text{MSE}}$. It is known that $\text{SNR} = 1/\hat{\text{MSE}}$, which characterizes the quantizer's input and is given by (5.46). It is noted that MSE_q does not express the final MSE of the quantized noisy signal. The above condition can be written as

$$\text{MSE}_q \leq \hat{\text{MSE}}, \quad (5.49)$$

which results a post-quantization MSE bounded as

$$\hat{\text{MSE}} < \text{MSE} \leq \hat{\text{MSE}} + 3 \text{ dB}. \quad (5.50)$$

The rule given by (5.49) can be used with linear quantization of the real and imaginary part of $\hat{\mathbf{h}}$, i.e. the pre-selected channel taps with mean power σ_h^2 . According to [114] and as provided by (5.36), we write

$$\text{MSE}_q = \frac{\sigma_q^2}{\sigma_h^2} = \frac{1}{3} \cdot \text{PAPR} \cdot 2^{-2B}, \quad (5.51)$$

where the $\text{PAPR} = X_{\max}^2/\sigma_h^2$ is determined for each quantization interval over the real and imaginary part of all selected taps. The quantization step Δ is given by

$$\Delta = \frac{X_{\max}}{2^{B-1}}. \quad (5.52)$$

By imposing now (5.51) into (5.49), the number of required quantization bits becomes

$$B \geq 0.17 \cdot (\hat{\text{SNR}}_{\text{dB}} + \text{PAPR}_{\text{dB}} - 4.77 \text{ dB}), \quad (5.53)$$

Expression (5.53) indicates that the number of bits B grows linearly with the SNR in dB, similarly to the rate required by the RD function in (5.48). Together with the result in Figure 5.7, which shows that the number of estimated channel taps also grows linearly with the SNR, this is fully in line with a fundamental requirement in information theory [122].

According to expression (5.53), more bits/symbol are required than by the RD expression (5.48), as $B > B_{\text{RD}}$. The PAPR lies typically between 7 and 17 dB, as evaluated per CIR for the SCME, see Figure 5.8. For practical purposes, we may further introduce a tuning parameter $\vartheta \geq 0$ dB, so that the number of bits/symbol is given by integer

$$B(\vartheta) = \left\lceil 0.17 \cdot (\hat{\text{SNR}}_{\text{dB}} + \text{PAPR}_{\text{dB}} - 4.77 \text{ dB} + \vartheta) \right\rceil. \quad (5.54)$$

Figure 5.9 depicts the number of quantization bits B , as evaluated over a sufficient number of SCME realizations according to (5.54) using $\vartheta = 0$ dB and according to the RD

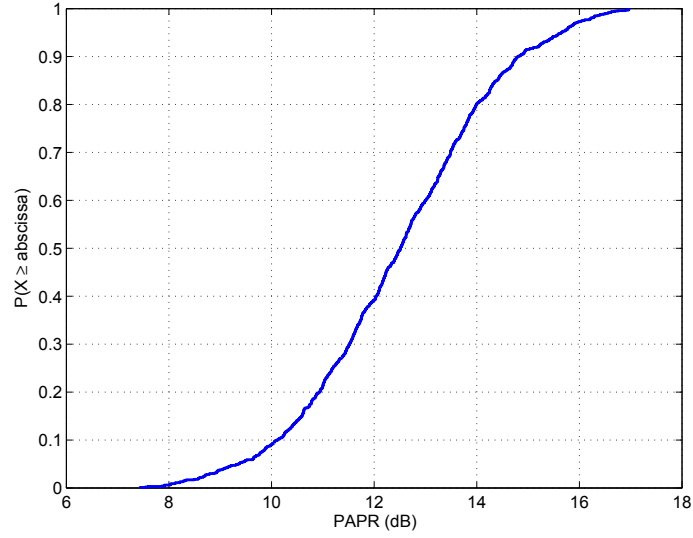


Figure 5.8: The PAPR lies between 7 and 17 dB for the SCME channel.

expression (5.48). In order to illustrate the potential of adaptive vs. fixed quantization, we have evaluated the average number of bits per tap for SNR values from 0 to 25 dB as 3.4 bits. Compared to fixed quantization using for example $B = 6$ bits/tap, adaptive quantization reduces the number of bits by 43%, on average.

We evaluate the quantization error in OFDM systems, therefore define the normalized channel square error nSE_p , which is calculated on each pilot subcarrier p , as

$$\text{nSE}_p = 10 \log_{10} \left(\frac{|\hat{H}_p - H_p|^2}{\frac{1}{N_p} \sum_{p=1}^{N_p} |H_p|^2} \right). \quad (5.55)$$

Here, \hat{H}_p and H_p are the frequency domain representations of estimated/quantized and true channels on pilot subcarrier p , respectively. Figure 5.10 illustrates the CSI degradation as given by (5.55) at several stages in the whole processing chain. A gain of 7 dB due to tap selection and a loss of 2 dB due to quantization can be observed. In order to avoid the quantization loss, the optional variable ϑ is introduced in (5.53) to obtain a more conservative decision. By setting $\vartheta = 6$ dB in (5.53), quantization uses one more bit and the MSE degradation becomes very small.

Interference-aware feedback reduction

So far, we have discussed feedback compression limited by AWGN. Since cellular networks are mostly limited by interference, we expect that noise-limited compression more feedback than necessary in practice. Owing to the clustering concept, even with perfect channel

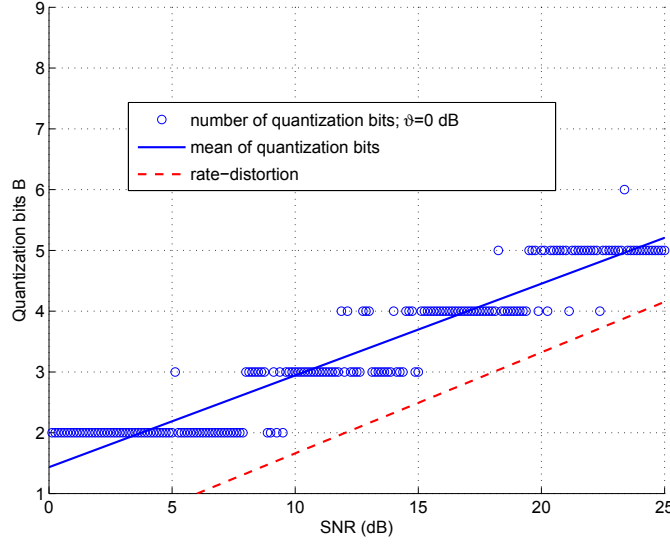


Figure 5.9: Number of quantization bits according to (5.54) with $\vartheta = 0$ dB, evaluated over a large number of channel realizations. The red dashed line corresponds to the rate-distortion function, which can be regarded as lower bound.

knowledge, some cells are not in the cluster and the performance is limited by out-of-cluster interference (I_{out}) in addition to the noise. Therefore, we aim to keep on average the inter-user interference I_u due to imperfect CSI to be less or equal to the out-of-cluster interference:

$$I_u \leq I_{\text{out}}. \quad (5.56)$$

We can say that even under the presence of impairments, the mean receive power a mobile user will be approximately equal to the mean data symbol energy E_s , as using ZF precoding. We can thus use $\beta_m \approx E_s$ in (5.38), where the inter-cluster geometry factor \mathcal{G} is defined. The out-of-cluster interference becomes

$$I_{\text{out}} \approx \frac{E_s}{\mathcal{G}}. \quad (5.57)$$

Considering Rayleigh fading channel conditions, and following the analysis of Section 2.3 for ZF precoding, the mean inter-user interference is found equal to

$$I_u \approx E_s \cdot \text{MSE} \cdot \frac{N_u}{N_b - N_u}. \quad (5.58)$$

The numbers of BSs and mobile users are denoted by N_b and N_u , respectively, with $N_b > N_u$. Regarding the channel model assumption, it is noted that a scheduling algorithm for joint transmission (JT) CoMP was developed in [63], which targets to maximize the

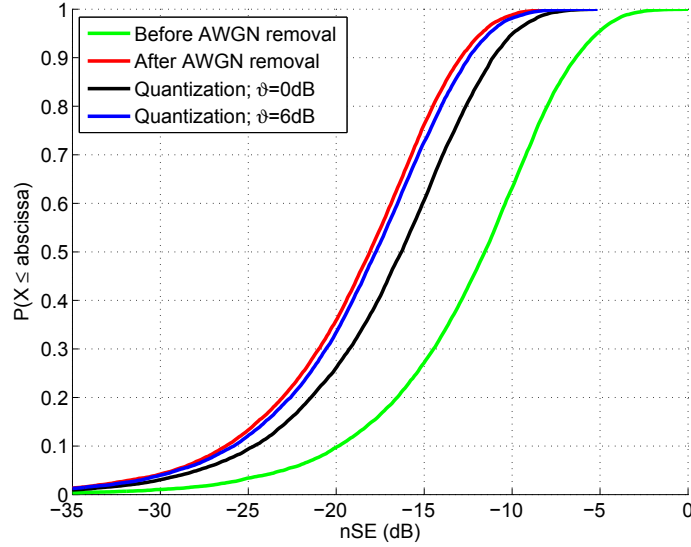


Figure 5.10: CDF of the normalized square error, evaluated for SCME on OFDM subcarriers as in (5.55): after IDFT (green), after tap selection (red) and after quantization with $\vartheta = 0$ dB and $\vartheta = 6$ dB (black and blue). The initial mean SNR is 10 dB.

system throughput. From outdoor channel measurements, the statistics of the eigenvalues characterizing the radio channel between the selected base stations and users were found close to the ones of a Rayleigh fading channel.

Unlike the signal model derived in Chapter 2, in (5.57) and (5.58), we have approximated that the user's self-signal power remains in average constant and its self-interference is considered as part of (5.58), which practically captures the overall intra-cluster interference. This approximation is valid for small MSE values, and allows for using the model also for one user, as also needed in Section 5.2.3.

By imposing now (5.57) and (5.58) into (5.56), we reach following condition for the channel MSE:

$$\text{MSE} \leq \frac{N_b - N_u}{N_u} \cdot \frac{1}{\mathcal{G}}. \quad (5.59)$$

Equation (5.59) indicates that the tolerable MSE is inversely proportional to the inter-cluster geometry \mathcal{G} . This means that accuracy requirements for CSI used for precoding get stricter as \mathcal{G} grows, i.e. as out-of-cluster interference I_{out} drops. For larger cooperation clusters, it is intuitive that I_{out} drops, which increases the required CSI feedback. It is also noted that the allowed MSE is proportional to a ratio involving N_b and N_u . For example, serving more mobile users within a cooperation cluster implies higher requirements to the MSE and thus, requires more precise feedback.

The inclusion of the interference-aware condition (5.59) into the feedback compression

scheme is shown in Figure 5.4 by dashed lines. There, the geometry factor \mathcal{G} is computed at the terminal during the clustering step and therefrom the desired MSE of the compressed CSI feedback as well, according to (5.59). The channel MSE can be controlled then either by adapting directly the number of quantization bits, or by slightly increasing the threshold level used for channel tap selection, as shown in Figure 5.4. As long as the final MSE fulfills (5.59), the number of channel taps can be reduced, which directly reduces the feedback overhead.

Feedback packet format

The format of a feedback packet is shown in Figure 5.11. It includes information of quantized complex-valued tap amplitudes plus a header with following information: cell index within the cluster (3 bits), MIMO link index within the cell (2 bits), number of quantization bits B (3 bits), quantization step size (12 bits) in case of adaptive quantization, and a final string according to the delay vector, with the length of maximum number of channel taps (144 bits), which has the value 1 at indexes with non-zero channel taps and the value 0 otherwise.

cell index	link index	step size	quant. bits	delay vector	taps
(3)	(2)	(12)	(3)	(144)	($B \cdot L \cdot 2$)

Figure 5.11: Feedback packet format for multi-cell CSI. The number of bits is given in brackets for each field.

5.2.3 Evaluation of feedback compression scheme

Channel model and field measurements

For evaluation the widely accepted SCME in the urban macro-cell scenario is used. 7 cells serving are one mobile user, who is randomly placed in the center cell. Channel impulse responses are modeled with 18 channel taps. Data obtained from channel measurements in our multi-cell testbed are also used, which is located within the campus of Technische Universität Berlin (TUB), Germany. As shown in Figure 2.5, 3 BS are placed on top of the Fraunhofer Heinrich Hertz Institute (HHI), the main building of TUB and the Telefunken tower, the inter-site distances (ISDs) are roughly 500 m. Antenna downtilt is set so that the main beam of the vertical antenna pattern hits the ground at 0.33 times ISD, approximately equal to a distance of 150 m. For a more detailed description of the setup see [80]. Parameters for SCME model and measurements are listed in Table 5.1.

The CSI is estimated from 144 pilots scattered over 1200 subcarriers of the OFDM symbol [85] for each antenna in each out of 6 cells. The estimated CSI is updated each 10 ms interval and the uncompressed results are recorded with 16-bit resolution for the real

Table 5.1: System and channel parameters

Parameter	SCME	Measurement
Carrier frequency	2.65 GHz	2.65 GHz
System bandwidth	20 MHz	18.36 MHz
Number of pilots	144 per antenna	144 per antenna
Channel taps	18	-
Number of cells	7	6
MIMO configuration	2x2 per cell	2x2 per cell
Inter-site distance (ISD)	500 m	\approx 500 m
Antenna downtilt	0.24 ISD	0.33 ISD
Tx power of base station	49 dBm	36.5 dBm
Noise figure	5 dB	-
Noise floor	-95 dBm	-95 dBm

Table 5.2: Frequency of cluster size appearance (%)

Cluster size \mathcal{M}'	1	2	3	4	5	6	7	\emptyset
Measurement $\kappa=6$ dB	51	31	10	7	1	1	-	1.7
Measurement $\kappa=12$ dB	26	30	16	21	3	4	-	2.6
Measurement $\kappa=18$ dB	8	21	14	31	10	16	-	3.7
SCME $\kappa=6$ dB	67	25	7	1	0	0	0	1.4
SCME $\kappa=12$ dB	38	30	22	7	2	1	0	2.1
SCME $\kappa=18$ dB	14	19	24	19	12	9	3	3.5

and imaginary parts of each estimated channel coefficient. Channel tap selection uses 4 iterations with parameter $\alpha = 4$ in (5.42). Adaptive quantization uses $\vartheta = 6$ dB in (5.54).

Cluster size and geometry factor

The cluster size for JT CoMP depends on the clustering threshold and the downtilt of antennas, as known from [115]. Table 5.2 shows the percentage of each cluster size \mathcal{M}' for thresholds $\kappa = 6, 12$ and 18 dB, both for measured data and SCME. For instance, the results of the measurements indicate that the mean number of cells is 2.6 for $\kappa = 12$ dB. The visualization of the results for channel measurements in a form of histogram is illustrated in Figure 5.12.

The achievable geometry from (5.38) is plotted for different clustering thresholds in Figure 5.13. Clearly, (5.38) is an optimistic estimation not yet achieved by realistic JT CoMP algorithms. But we can use it to minimize the feedback, as described above. In general, we observe that the mean geometry is a little larger than the clustering threshold, e.g. a threshold of 12 dB results in a mean inter-cluster geometry of 13 dB using the SCME.

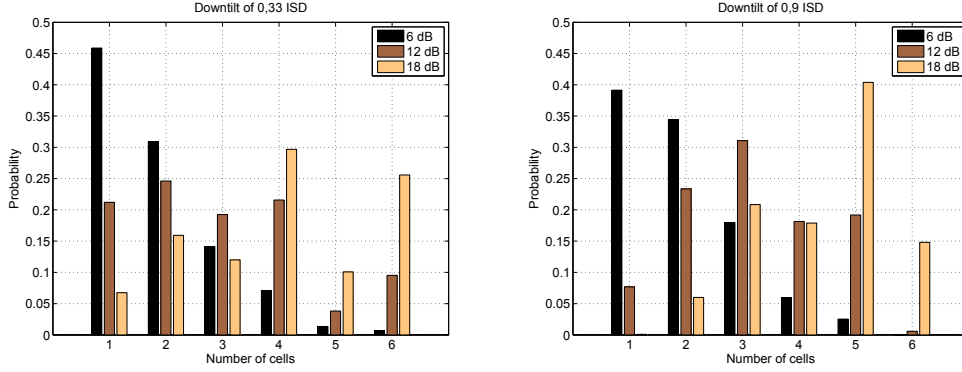


Figure 5.12: Frequency of cluster size appearance according to the threshold κ , set to 6, 12 and 18 dB; *Left*: downtilt of 0.33 ISD; *Right*: downtilt of 0.9 ISD.

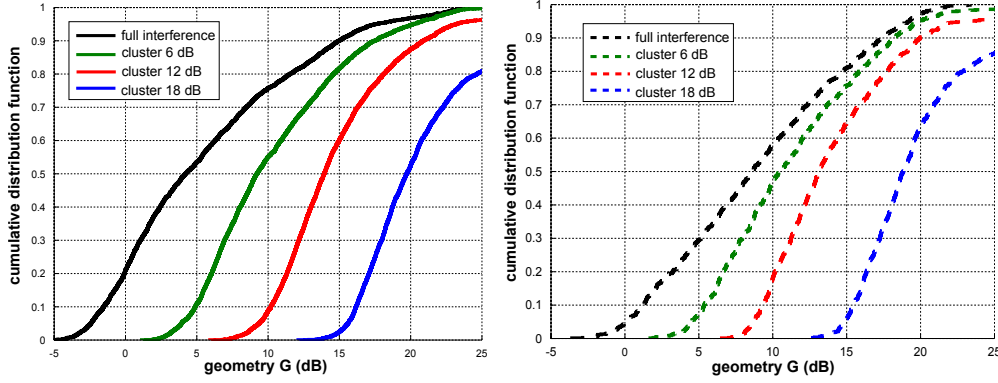


Figure 5.13: Inter-cluster geometry factor \mathcal{G} in dB, according to (5.38), without clustering and for a cluster threshold κ of 6, 12 and 18 dB; *Left*: measurement with downtilt of 0.33 ISD; *Right*: SCME channel model.

Feedback compression performance

Figure 5.14 (top) shows the CDF of the feedback required for one user to all its serving base stations within the cluster, for noise-limited compression. Results based on measured channels are shown with solid lines, while the SCME model results are shown with dashed lines. A stepped characteristics is observed when the cluster size changes.

Feedback compression has a clear benefit. Without it, we would need to feed back CSI for 6 base stations for 144 pilots with 2 times 16 bit resolution for real and imaginary component for 2 antennas in our 2x2 MIMO configuration using 55 kbit per reporting interval. Note that the underlying pilot grid already contains the minimum number of pilots needed to identify the multi-path channel (i.e. the number of pilots is equal to the length of the cyclic prefix). After interference-aware compression, only 3% of the original information is needed on average and at most 10%. By introducing interference-limited

compression, i.e. considering optional blocks connected with dashed lines in Figure 5.4, the feedback can be further reduced, as shown in Figure 5.14 (bottom), for both measurement and SCME. For example, for a clustering threshold of $\kappa = 12$ dB, we can on average reduce the feedback rate from 3.5 kbit to 2.5 kbit per reporting interval in the measurement. Compared to the uncompressed feedback this is a reduction by a factor between 16 to 22.

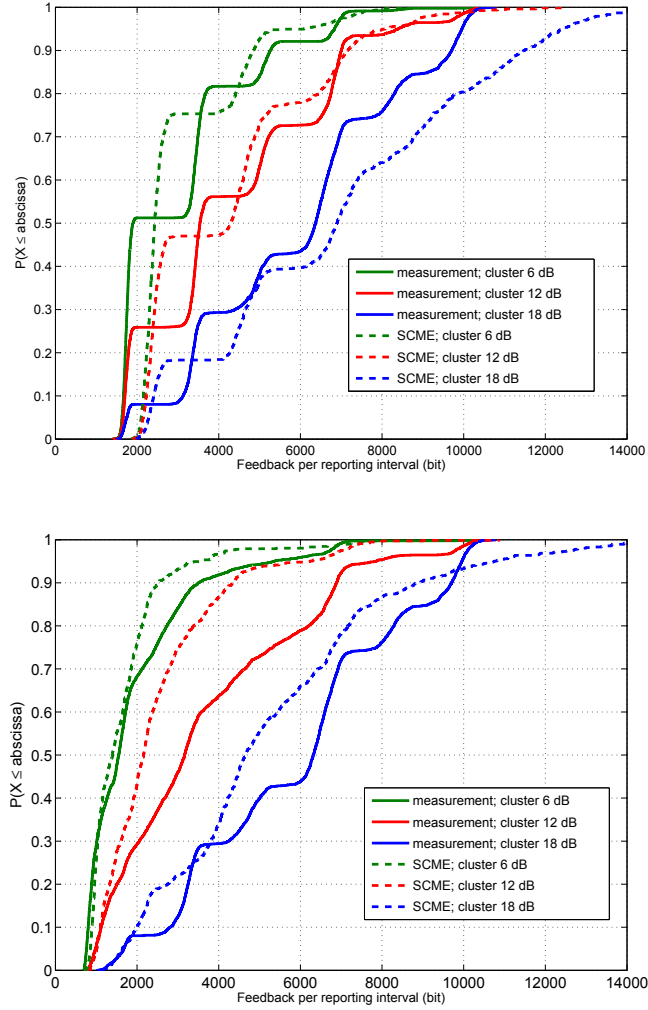


Figure 5.14: CDF of feedback per reporting interval for different clustering thresholds κ . *Left*: noise-aware, *Right*: interference-aware feedback compression. *Solid lines*: measurement track shown in Figure 5.15. *Dashed lines*: SCME with 7 cells and one user in the middle cell.

Figure 5.15 and Figure 5.16 illustrate the required feedback at measurement positions for a clustering threshold $\kappa = 12$ dB and using interference-aware CSI compression for an antenna downtilt of 0.33 ISD and 0.9 ISD, respectively. At positions with blue color,

the required feedback is related to one or two cells only. In these areas, one sector has often a free line-of-sight (LOS). More feedback (red color) is needed at positions shaded simultaneously from all base stations. In the center of the testbed where the cluster size is high, the non-line-of-sight (NLOS) type of channels implies a larger number of taps.

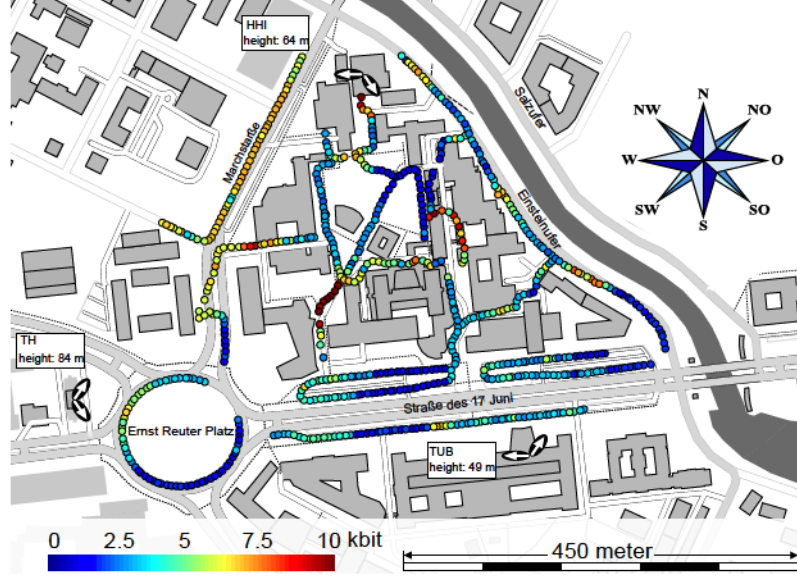


Figure 5.15: CDF of feedback per reporting interval for all clustered cells after interference-aware compression. An antenna downtilt of 0.33 ISD is used and the clustering threshold set to $\kappa = 12$ dB. Transmit directions are shown by arrows.

5.3 Compensation by channel prediction

In this section, channel prediction is investigated as a technique for compensating the effect of outdated CSI. A novel channel prediction method is presented, which is based on a Doppler-delay model of the time-variant radio channel. The proposed scheme consists of three steps: in a first step, the most significant channel taps are extracted in the delay domain, like in the above section. In a second step, a novel HR algorithm is used for extracting the major Doppler frequency components for each channel tap. In this way, a shorter observation history of the channel is needed, compared to the standard DFT technique. Prediction is performed by imposing the estimated parameters into the channel model and extrapolating in time direction. Evaluation over the SCME as well as with measured channel data shows that the channel MSE can be reduced by roughly 10 dB for typical feedback delays between 2 and 10 ms, which translates directly into SIR gains in JT CoMP. Finally, it is shown that, even if the Doppler frequencies are extracted from realistic quantized and noisy estimates of CSI feedback, the channel predictor is able to

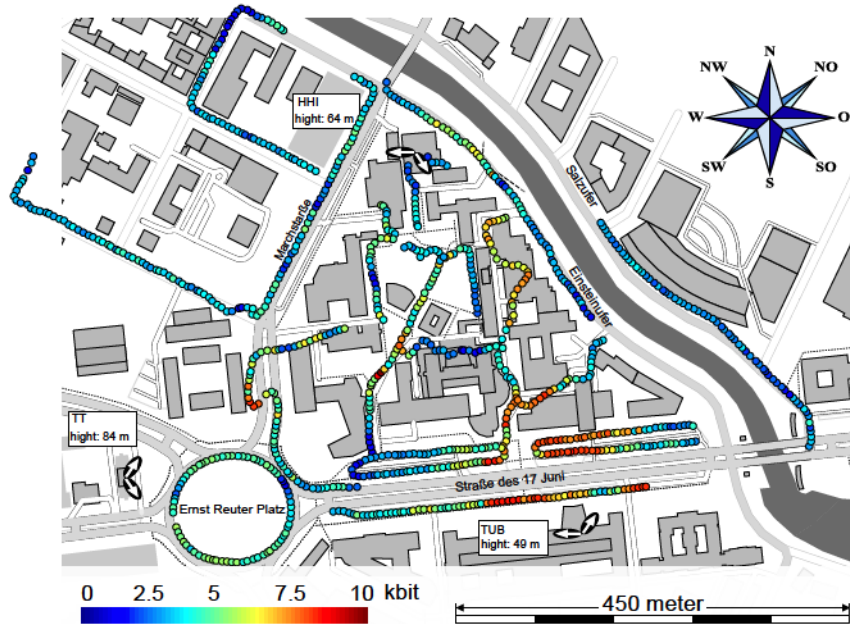


Figure 5.16: CDF of feedback per reporting interval for all clustered cells after interference-aware compression. An antenna downtilt of 0.9 ISD is used and the clustering threshold set to $\kappa = 12$ dB. Transmit directions are shown by arrows.

achieve a similar performance as when Doppler frequencies are estimated from perfect channel knowledge.

Prior art on channel prediction

A lot of research has been conducted during the last years on channel prediction of mobile radio channels, and its value for base-coordinated cellular networks has become clear. The requirements on channel knowledge at the BSs performing MIMO have been already shown in [127]. Meanwhile, it is known that JT CoMP systems become more robust when linear channel prediction techniques such as Kalman and Wiener filtering are used [128]. Channel prediction by frequency-domain filtering and gains for JT CoMP have been evaluated in [129]. For achieving robust operation at higher mobilities, it has been shown that it is important to adapt the precoder to different reliabilities of the predicted channels [130]. Kalman filters provide such information intrinsically, which can be reported semi-statically from the terminals [131]. In [132] it has been shown that prediction in the time-domain outperforms frequency-domain methods. Channel prediction in the time-domain has been investigated in [123], and a scheme for compensating channel aging effects and enhancing JT CoMP has been proposed. Finally, the authors in [133] have presented three time-domain filtering-based methods for narrow-band channel prediction, based on the directions of wave arrival, which can be estimated by using carefully calibrated antenna arrays.

5.3.1 Doppler-delay based channel prediction

Doppler-delay based channel prediction is a non-linear method, which has been initially introduced by the author in [7]. It is a parameter-based approach, where specific channel features are estimated from channel observations and are then inserted into a channel model, which is used for prediction by extrapolation in time. The overall procedure consists of parameter extraction, CSI feedback construction and channel prediction, which can be split as modules between terminals and base stations. This allows for flexible system design, in order to meet requirements related to feedback overhead and computationally complexity at the terminals. Figure 5.17 shows the block diagram of such parameter-based procedures in a multi-cellular multi-user system, in which channel parameters are estimated at

channel predi

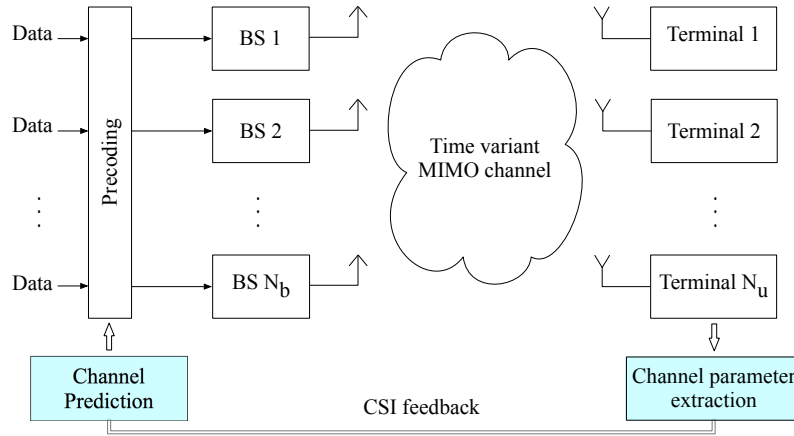


Figure 5.17: Multi-cellular multi-user channel prediction scheme: channel parameter extraction, CSI feedback and channel prediction can be split as modules between terminals and base stations. Data precoding uses the predicted channel.

The Doppler-delay method consists of three steps, which are shown in Figure 5.18. In the first step, significant channel taps are extracted in the delay domain. For this, the procedure for channel tap detection, which is described in Section 5.2 is used. In case the mobile users report this CSI feedback to the base stations, adaptive quantization can be also included, as described in Section 5.2.

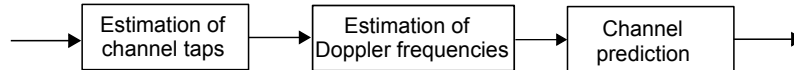


Figure 5.18: Blocks of the Doppler-delay channel prediction: channel tap identification, Doppler frequency estimation per tap and channel prediction by extrapolation.

The second step of the procedure is based on some assumptions regarding the channel model, which are described in what follows. When observing the mobile radio channel for time intervals equal to the feedback delay, we can safely say that large-scale parameters such as path loss and shadow fading do not change and any variation is only related to small-scale fading [84]. Assuming thus wide-sense stationary uncorrelated scattering (WSSUS), we can model each channel tap as a sum of discrete reflections (called sub taps) of the transmitted waveform at obstacles in the nearby physical environment, which arrive within one sample duration. Since each of those sub taps arrives from a different direction, it is characterized by its individual Doppler frequency weighted with a complex-valued factor, according to the velocity and the angle of wave arrival.

In order to estimate the Doppler frequencies for a channel tap, it is required to obtain a frequency-domain representation of its time evolution. Therefore, the evolution (history) of each estimated tap is recorded for a short observation time. As a first approach, a DFT is applied to the channel history and it is searched for peaks in the Doppler spectrum, from which the main Doppler frequencies can be estimated. This method is simple but has the drawback that it needs a long observation time in order to achieve a sufficient Doppler frequency resolution. During this time, the large-scale propagation parameters can change and the model stops from being valid.

Therefore, a HR algorithm has been developed, which is able to extract the major discrete Doppler frequency components and provide their complex-valued weights for each channel tap, by using a significantly shorter history. A first version of this HR algorithm was developed in [86], in order to estimate channel taps from frequency domain pilots. Here, the algorithm has been adjusted in a way that it can estimate Doppler frequencies from a channel tap history, whereas its computational complexity has been also reduced. By using the HR estimator, a shorter history of the channel is needed, compared to the standard DFT technique. The channel parameters are extracted for each sub tap, until a metric measuring the residual deviation between the recorded and the reconstructed channel history is fulfilled. A detailed description of the HR algorithm can be found in Appendix 7.3.1. The SNR characterizing the reconstructed channel history is calculated as described in Appendix 7.3.1 and is typically over 30 dB, as also shown in [86].

In the third step, channel prediction is performed by imposing the estimated parameters into the channel model and extrapolating in time direction, based on the estimated channel tap and Doppler frequency parameters. The predicted value of a channel tap $\tilde{h}_l(t)$ for a future time instant t is calculated by the superposition of S extrapolated sub taps, i.e. sinusoids with individual frequencies, given by the estimated Doppler frequencies and complex-valued weights:

$$\tilde{h}_l(t) = \sum_{s=1}^S \alpha_{l,s} \cdot e^{j\phi_s} \cdot e^{j2\pi f_{l,s} \frac{q(t)}{Q}}. \quad (5.60)$$

The Doppler frequency and complex-valued weight characterizing the s^{th} sub tap of the l^{th}

channel tap are denoted by $f_{l,s}$ and $\alpha_{l,s} \cdot e^{j\phi_{l,s}}$, respectively. The prediction horizon is $q(t)$, measured in seconds, and the number of recorded time samples of a channel tap is Q .

Figure 5.19 illustrates two examples for channel tap history reconstruction for an observation time of 32 ms and prediction for 20 ms. Here, the 5 strongest sub taps are considered. The MSE for channel reconstruction lies typically around -40 to -30 dB [86], which is very satisfactory. However, in some cases the predicted channel diverges from the actual one. This happens for weak channel taps and is explained by the way the channel taps are estimated. Even when using a smoothening window, as described in Section 5.2, there is still cross-talk between the estimated taps in addition to AWGN. These small taps are not present in the physical channel as they are generated from the application of IDFT in the limited system bandwidth. As a consequence, the HR algorithm output does not represent the truly existing Doppler frequencies, which would enable for predicting the future tap evolution with a high accuracy. Therefore, accurate channel tap and delay estimation in the first stage is of high importance. A further case in which prediction may suffer, is when more than one Doppler frequencies lie very close to each other, which is typical for two wave reflections reaching the mobile user from a similar direction. In this case, a small estimation error in their Doppler frequencies may cause that the predicted channel diverges from the actual one.

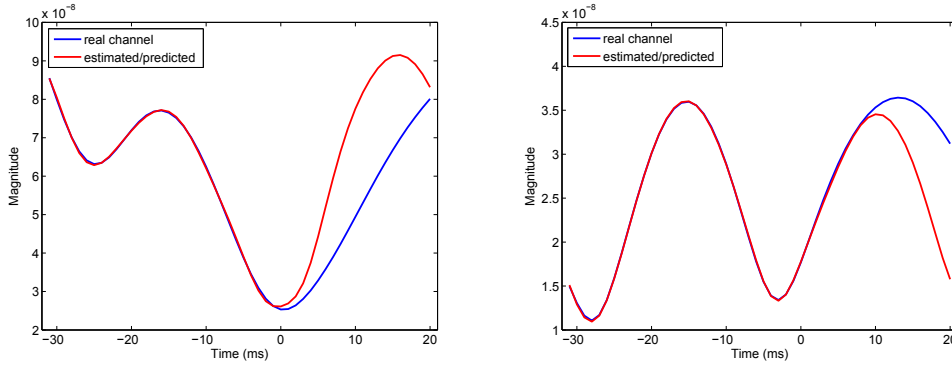


Figure 5.19: Examples of accurate channel tap reconstruction for observation time $[-31, 0]$ ms. Prediction for $[1; 20]$ ms may diverge from the actual channel. Here, the 5 strongest out of 20 existent sub taps are used in the SCME.

It is noted that unlike other state-of-the-art techniques based on the estimation of angle of arrivals, the method presented here uses only a single antenna at the terminal. The HR algorithm detects directly the discrete Doppler frequencies and does not require the information of the angle of arrival, which is related to the Doppler frequency. Finally, the proposed approach does not use any filter for channel prediction, which is instead realized by a simple extrapolation of our channel model in the time domain.

5.3.2 Evaluation of the channel MSE

Here, the performance of the Doppler-delay based channel predictor is evaluated in terms of the MSE, which is a function of time t , defined as

$$\text{MSE}(t) = \frac{\mathbb{E}_H \left\{ |\tilde{H}_p(t) - H_p(t)|^2 \right\}}{\sigma_h^2}. \quad (5.61)$$

Above, $\tilde{H}_p(t)$ and $H_p(t)$ denote the predicted and actual channel on OFDM pilot subcarrier p at time instant t , while the expectation operator is applied over all N_p subcarriers and channel realizations, as well as the mean channel power. In addition to the MSE, the so-called normalized square error (nSE) is evaluated:

$$\text{nSE}_p(t) = \frac{|\tilde{H}_p(t) - H_p(t)|^2}{\sigma_h^2}, \quad p = 1, \dots, N_p. \quad (5.62)$$

For a given time instant, expression (5.62) provides the full statistics of the channel square error, measured on all OFDM pilot subcarriers and will be illustrated as a CDF. It is obvious that $\text{MSE}(t) = \mathbb{E}_H \{ \text{nSE}_p(t) \}$.

In what follows, the role of system and algorithm parameters is studied, and guidelines for practical implementation are given. For evaluation the SCME is used, as well as channel data taken from outdoor measurements. The system parameters follow the current Third Generation Partnership Project (3GPP) Long Term Evolution (LTE) specification [31].

Table 5.3: 3GPP LTE system parameters

Parameter	Value
Carrier frequency	2.65 GHz
System bandwidth	20 MHz
Sampling frequency	30.72 MHz
No. of OFDM subcarriers	2048
No. of subcarriers with data	1200
No. of pilots in frequency	200

Considering an OFDM system, the channel is measured on pilots in the frequency domain. From these observations, the CIR is observed by a inverse fast Fourier transform (IFFT), as described in Section 5.2, with a maximum length of 144 channel taps, which corresponds to $4.7 \mu\text{s}$, as no channel taps are expected with larger delays. The search interval of the HR algorithm is limited to the maximum Doppler frequency according to the user's mobility, in order to avoid incorrect estimates due to noise. Finally, channel taps, which are identified for less than half of the observation time are not passed to the predictor and are set to zero. Evaluation is performed over 50 independent channel initializations, whereas for each of them, a channel history of 400 ms with one channel real-

ization (snapshot) every 1 ms is observed, which is sufficiently longer than typical feedback delay times. Channel taps and Doppler frequencies are estimated up to every 1 ms.

Evaluation over the SCME channel model

As a first evaluation scenario of the channel prediction mechanism, an implementation of the complete procedure at the terminal is considered, where non-quantized channel information on pilot frequencies is provided, as shown in Figure 5.20. The influence of the individual parameters is investigated by using the SCME with main parameters listed in Table 5.4.

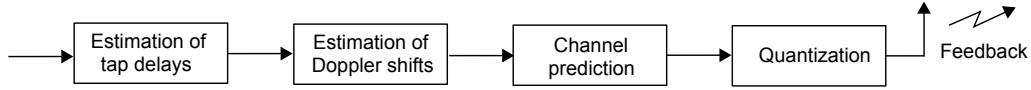


Figure 5.20: Implementation of the total channel prediction procedure at the terminal.

Table 5.4: SCME channel parameters

Parameter	Value
Channel type	urban macro, LOS/NLOS
Terminal velocity	30 km/h
No. of channel taps	18
No. of sub taps per tap	20

One of the first results is that for the SCME, where each channel tap is built from 20 discrete sub taps, a channel observation time of 32 ms reaches almost the maximum accuracy in Doppler frequency estimation. In general, it is known from [86] a ratio between input and output samples of at least $3/2$ is required for the HR estimator. It is noted that for the fast Fourier transform (FFT)-based Doppler estimation, a much longer time interval would be needed in order to achieve a comparable resolution. It is also intuitive that, as long as large-scale channel propagation parameters remain constant, longer observation times can only improve the Doppler estimation accuracy. For mobile outdoor scenarios, however, it usually happens that the WSSUS model assumption stops being valid and that sub taps or even channel taps disappear or new ones appear. For the evaluation frameworks using the SCME, an observation time of 32 ms will be used as a typical setting, while the influence of this parameter will be investigated in what follows, by using channel data from outdoor measurements.

Figure 5.21 depicts the MSE, which has been evaluated over a large number of SCME realizations. Channel prediction has been performed for different numbers of sub taps per channel tap, which have been estimated from an observation time of 32 ms. CSI is provided every 1 ms and is assumed to be perfectly known on the pilot subcarriers. From Figure 5.21 it can be observed that for typical delays between 2 ms and 10 ms, the MSE is reduced by

8 to 10 dB, compared to the MSE of the outdated channel. If not using any prediction, the MSE raises already after 5 ms to a level of around 3 dB, which leads to an SNR level below 0 dB according to (2.14) and (2.17) and is thus not practical for data precoding. Results also indicate that estimating and using for prediction more than 3 Doppler frequencies, reduces the MSE only for feedback delays that are shorter than 5 ms. For larger delays, i.e. longer prediction horizons, one can observe that the unavoidable (small) errors of the Doppler estimation accumulate and therefore the MSE runs into a floor, which is here at about -2 dB. This shows that for long prediction times, the predictor yields reasonable results for the large-scale fading, but possibly no longer for the small-scale fading.

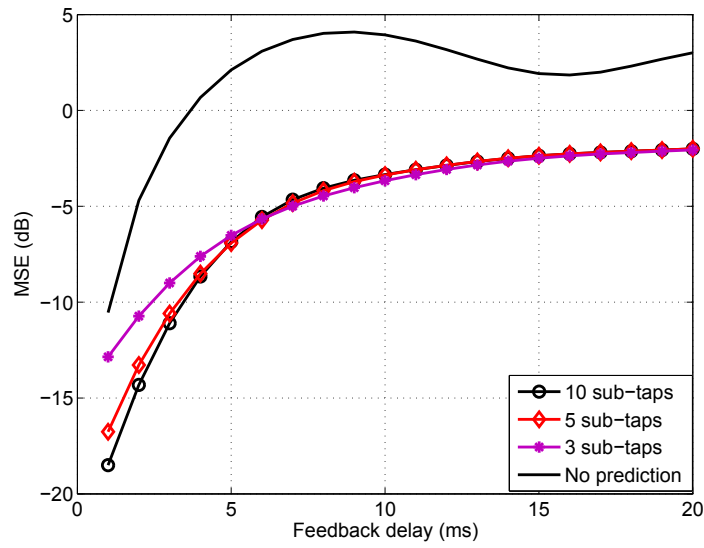


Figure 5.21: Channel MSE after Doppler-delay based prediction, using perfect CSI as an input. For feedback delays above 4 ms, estimating more than 3 Doppler frequencies does not offer additional MSE gains.

Next, the influence of AWGN on pilot subcarriers was investigated and it was found that the HR algorithm is very robust to noisy inputs. Figure 5.22 evaluates the MSE for different noise levels at the receiver. As observed, significant prediction gains are still feasible for low SNR values. The reason for this robustness against AWGN lies in the de-noising procedure performed by the HR algorithm, which offers an SNR gain of roughly 6 dB [86]. For larger prediction horizons, the MSE converge to a level, which does not depend on the SNR and is determined by the accuracy of the Doppler frequency estimation. Here, non-quantized CSI is provided every 1 ms.

As a next implementation we consider a scheme where channel tap estimation and quantization are performed at the terminal, while Doppler frequency estimation and channel prediction at the BS, as shown in Figure 5.23. Compared to the terminal implementation, this module split has the advantage that the computationally demanding HR algorithm is

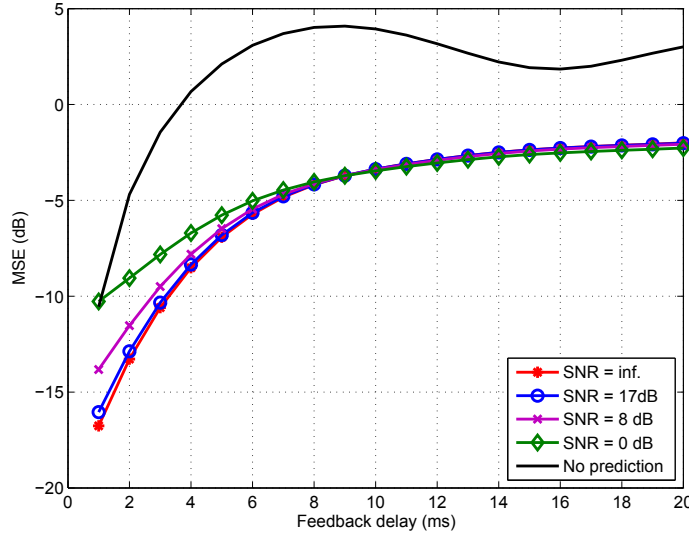


Figure 5.22: Channel MSE for Doppler frequency estimation at different SNR levels. The high-resolution estimator performs stable with noisy inputs.

performed at the base station, where computational power is more easily to be provided. A further difference is that the Doppler frequency estimator uses quantized CSI as an input. Figure 5.24 evaluates the impact of the number of quantization bits (B) per channel tap onto the channel prediction MSE. CSI feedback is provided every 1 ms, observation time is 32 ms and the mean receiver SNR is set to 20 dB. Results indicate that Doppler frequency estimation is robust against quantized inputs and 6 bits/tap are sufficient. Figure 5.25 depicts the CDF of the the nSE for the same parameters and feedback delays of 5 and 10 ms. Both the nSE statistics as well as its mean value (MSE) are reduced by around 10 dB.

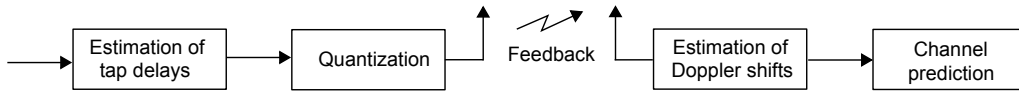


Figure 5.23: Channel taps are estimated and quantized at the terminal (left) and fed back to the base station (right), where Doppler frequency estimation and channel prediction are performed.

In what follows, the role of the feedback reporting interval, i.e. how often CSI feedback is provided to the base stations, is investigated. Figure 5.26 depicts the MSE for feedback reporting intervals of 1 and 5 ms. CSI is estimated from channel observations measured in an SNR environment of 20 dB and quantized with 6 bits per real and imaginary part. During the observation time of 32 ms, feedback is thus provided 32 and 6 times, depending

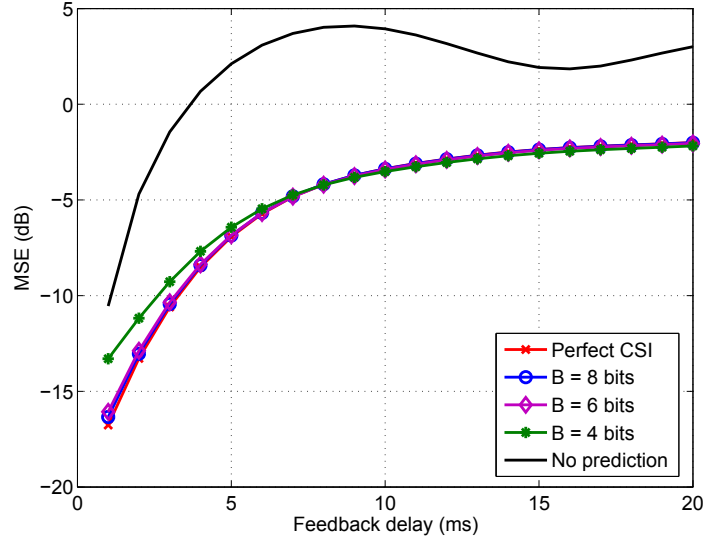


Figure 5.24: Normalized MSE for Doppler-delay based channel prediction at the base station for an observation history of 32 ms, using as input quantized CSI, available every 1 ms. SCME with 30 km/h is used, while SNR is equal to 20 dB.

on the reporting interval. It can be observed that when providing feedback every 5 ms and using it for subtap estimation, the post-prediction MSE is at the same level as when providing feedback every 1 ms. This is enabled due to the high resolution of the subtap estimator, which is able to perform accurately even with a small input value density. It is though recommended that ratio between input and output samples is larger or equal to $3/2$.

An important observation from all MSE curves provided up to here, is that parameters such as the input SNR, the number of bits used for channel tap quantization, the CSI updating interval and the number of estimated Doppler frequencies affect mainly the performance for short prediction horizons between 2 and 5 ms. If the expected feedback delay lies within this range, an adjustment of these parameters is recommended. For larger prediction horizons, all MSE curves approach a level of roughly -2 dB, which is independent from the above parameters. This value is less important for practical systems, as the feedback delays are not expected to be so large. However, it is interesting to see that the prediction performance is practically determined by the estimation accuracy of the Doppler frequencies by the HR algorithm, which is robust against impairments at its input, such as noise and quantization effects and provides a high resolution even for sparse inputs.

Finally, an implementation split in which channel tap and Doppler frequency estimation are performed at the terminal, and channel prediction at the base station has been considered, as shown in Figure 5.27. It has been found that channel prediction is very sensitive

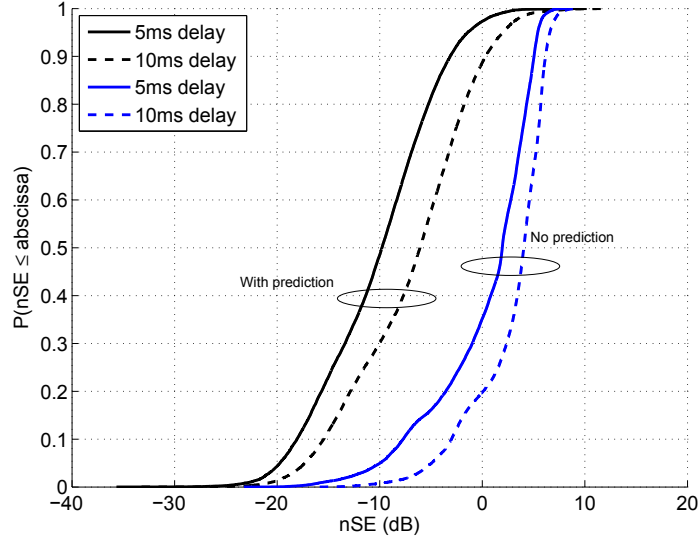


Figure 5.25: For typical feedback delays, channel prediction reduces the normalized channel square error (nSE) by around 10 dB. Here, 6 bits/tap quantization is used.

to quantization of the subtaps, i.e. of the HR algorithm output. Results indicated that for Doppler frequency quantization, at least 8 bits/subtap would be required in order to avoid significant MSE enhancement, compared to the previous implementations. In addition, the terminal would need to perform the computationally complex HR algorithm. Regarding the feedback overhead, counting e.g. with 4-5 subtaps/tap, it would be also much higher than for the other schemes shown in Figure 5.20 and Figure 5.23. Hence, the original split to perform IDFT at the terminal and to feed back quantized channel tapes is recommended.

Evaluation using channel data from outdoor measurements

In order to validate the Doppler-delay channel predictor under real-world conditions, we used channel data taken from outdoor measurements conducted by Ericsson Research in Stockholm, Sweden. A detailed description of the measurement campaign and all technical details can be found in [134], while here only the most important features and parameters will be given.

The channel data used here were acquired from broadband measurements from three single-antenna base stations, which are part of an LTE test network in Kista, Stockholm, Sweden [134]. The area is classified as urban, where the average building height is approximately 25 m. The antennas of all base station sites are above the average rooftop level and the distance between the base stations is between 350 m and 600 m. Commercially available antennas were used, with a gain of 18 dBi, $\pm 45^\circ$ linear polarization, half power

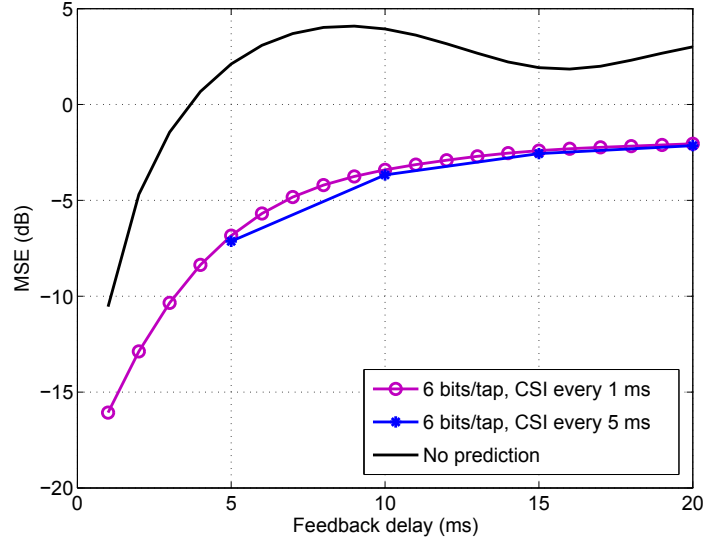


Figure 5.26: Impact of the CSI reporting interval on the prediction performance.

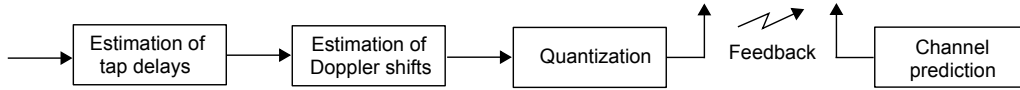


Figure 5.27: Channel taps and Doppler frequencies are estimated at the terminal (left), quantized and fed back to the base station (right), where channel prediction is performed.

beamwidth of 63° in azimuth and 5° in elevation, and a downtilt between 6° and 8° . The transmit power was set to 35 dBm for all base stations.

A measurement vehicle was moving with a speed up to 30 km/h. The receiver was equipped with 4 antennas (two electrical and two magnetic dipoles) which have been installed on the roof of the vehicle. The measurements were collected using a wide-band channel sounder with full MIMO capability, which is an LTE prototype developed by Ericsson. During the measurement campaign, however, only a single transmit antenna at each base station was used to guarantee perfect coherency among the base stations. The channel sounding capability was fully exploited by transmitting only pilot symbols over the entire bandwidth of 20 MHz at a carrier frequency of 2.66 GHz and every 5.33 ms. Each base station was transmitting pilots on every third OFDM subcarrier, separated by a subcarrier spacing of 15 kHz. In order to identify pilots from different base stations, a shift of one subcarrier was used, so that pilots from the same base station are transmitted every 45 kHz.

Optical fiber connection was used between the base stations. Accurate time synchronization among the base stations and with the receiver was achieved by Rubidium clocks from

Stanford Research Systems, which have an Allan standard deviation less than 10-12 Hz². The route consisted of passages with LOS propagation conditions, as well as parts where NLOS propagation dominated. During each ride, the channel sounder was measuring every 5.3 ms the channel for each pair of transmit and receive antennas.

Figure 5.28 evaluates the role of the observation time (T_{obs}), from which the Doppler frequencies are estimated. First, CSI quantization is not considered and the 10 major Doppler frequencies are estimated. It can be observed that using a channel history of 50 ms reduces the MSE by 1 dB, compared to using a history of 25 ms. However, using longer observation times of 100 ms or even 200 ms is beneficial only for longer prediction horizons beyond 6 ms. For a prediction horizons below 5 ms, Doppler frequency detection from the very recent channel history is recommended, so that large-scale channel parameters remain as stable as possible.

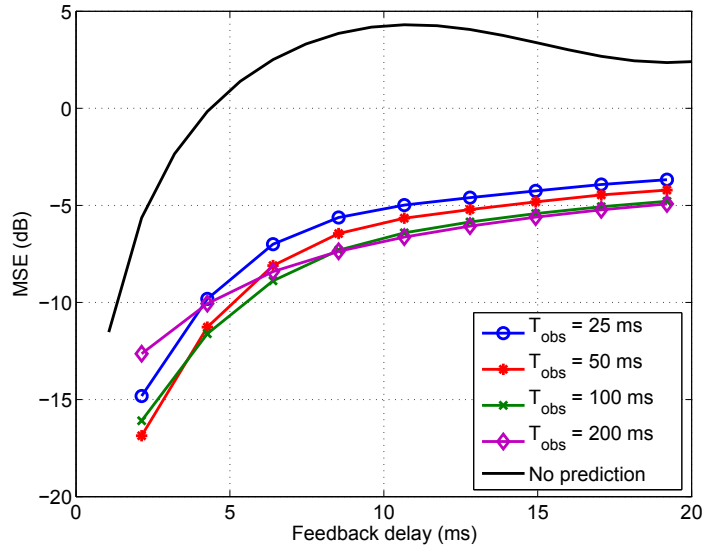


Figure 5.28: Impact of channel observation time (T_{obs}) onto the MSE. T_{obs} should be chosen according to the prediction horizon. Here, perfect CSI was assumed and 10 sub taps/tap were used.

Figure 5.29 evaluates the MSE in dependence of the number of the estimated sub taps. Based on perfect CSI, it can be observed that using 10 Doppler frequencies improves slightly the MSE only for short delays around 2 ms. We further introduced impairment effects such as AWGN of -120 dBm to the channel measurements and a 5 bit quantization of real and imaginary parts of the channel coefficients. In such more realistic scenario, the uncertainty caused by impairments overwhelms the MSE gain achieved by using more sub taps. As a result, the MSE lies at approximately the same level for 6 and 10 sub taps.

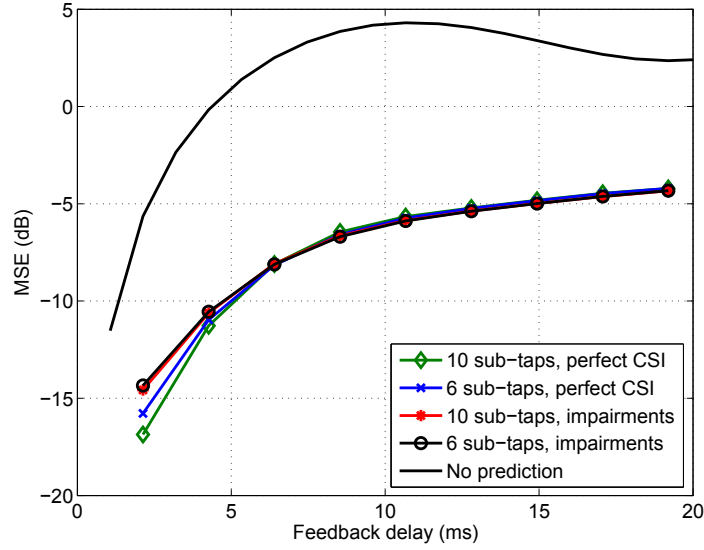


Figure 5.29: Estimation of 10 sub-taps from perfect CSI slightly improves the MSE for short delays, compared to estimating 6 sub-taps. For noisy and quantized CSI, the MSE cannot be further reduced by using more sub-taps.

As a state-of-the-art reference, channel prediction based on Kalman filtering is included. A detailed description and performance evaluation of the Kalman-based predictor used here can be found in [131] and [130]. According to this method, the channel on each subcarrier is modeled an autoregressive (AR) model of n_{AR} order on diagonal state space form. The n_{AR} poles of the AR-model are determined using the channel autocorrelation, which is estimated from the channel history. Here, perfect channel knowledge has been assumed, which maximizes the prediction accuracy, and $n_{\text{AR}} = 10$ is used. The filter poles are updated at sparse time instants, here every 0.43 s. A single Kalman filter can be estimated and used for several adjacent pilots (here for 4 pilots), as channel correlation in the frequency domain is provided. This reduces computational complexity without any noteworthy penalty in performance. Channel estimates are finally extrapolated into the future by using the pre-calculated filter.

There are conceptual differences between Kalman filtering and Doppler-delay based prediction, which make comparing them not a straightforward task. It should be taken in account that Doppler-delay prediction uses channel taps as an input, which are obtained from the frequency-domain pilots by an inverse FFT. This introduces a signal convolution with a sinc-function due to the limited bandwidth, which generates cross-talk between channel taps and introduces some difficulty in characterizing each of them by a certain number of Doppler frequencies. At the same time, the Kalman filter uses damped sinusoids instead of perfect sinusoids (Doppler frequencies), which introduces a small driving

noise and also limits the theoretically achievable accuracy [131].

Figure 5.30 evaluates the MSE for both methods. Perfect channel knowledge is assumed and the same order is used for both models, i.e. 10 subtaps and 10 poles, respectively. It can be observed that for typical feedback delays between 2 and 10 ms, significant improvements can be observed for both methods. For short prediction horizons, the Kalman method slightly outperforms the Doppler-delay method, while for larger horizons the two methods reach the same MSE level. This can be linked with high probability to the fact that the Kalman filter uses accurate information of the channel autocorrelation function, and is adjusted according to its values for those particular delay time.

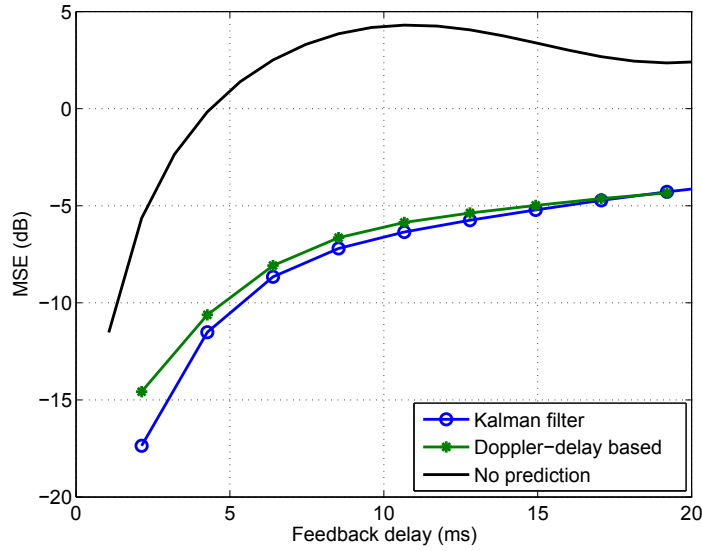


Figure 5.30: Channel prediction MSE for Doppler-delay based and Kalman filtering prediction, both using a 10th order model. Perfect CSI at subcarriers has been used as an input. Both methods offer similar and significant MSE reduction.

Overall, results in Section 5.3 show that Doppler-delay channel prediction reduces the MSE by roughly 10 dB, which implies significant SIR gains for the JT CoMP downlink. The prediction performance by using the SCME and measured channel data was found to be very similar. For system design it is recommended to implement channel tap estimation at the mobile station and provide afterwards the compressed CSI feedback to the base station. Doppler frequency estimation and channel prediction can be performed at the base station, so that feedback overhead is reduced and the terminal must not perform computationally complex operations.

5.4 SIR gains by mitigation of channel impairments in JT CoMP

In JT CoMP, improvements in CSI accuracy translate into performance gains, because the SIR is inversely proportional to the MSE, as shown in Chapter 2. The SIR further grows with the number of cooperating base stations (N_b) and drops with the number of users (N_u), which are served jointly on the same time and frequency resource. In this section, the SIR gains by Doppler-delay based channel prediction are evaluated analytically and by system-level simulations, using as an input the post-prediction MSE. A one-ring cluster of 7 base stations is considered, transmitting jointly to N_u mobile users over the SCME. Implementation follows the scheme shown in Figure 5.23. Out-of-cluster interference is not considered and the network is assumed to be perfectly synchronized in terms of carrier and sampling frequencies.

For numerical evaluation, the general model for precoded MIMO of Chapter 2 is used. The precoder \mathbf{W} is calculated from channel \mathbf{H} , while data vector \mathbf{s} is transmitted over the channel $\tilde{\mathbf{H}} = \mathbf{H} + \mathbf{\Delta}$, where $\mathbf{\Delta}$ denotes here the residual channel error matrix after channel prediction. Our goal is to evaluate the influence of the IUI caused by imperfect precoding, and will therefore neglect AWGN at the receiver. Hence, an arbitrary user j will receive

$$y_j = \underbrace{s_j \left(1 + \sum_{b=1}^{N_b} \delta_{jb} w_{bj} \right)}_{\text{self-signal } (\check{s}_j)} + \underbrace{\sum_{\substack{u=1 \\ u \neq j}}^{N_u} s_u \sum_{b=1}^{N_b} \delta_{jb} w_{bu}}_{\text{inter-user interference } (\bar{s}_j)}, \quad \text{with } j = 1, \dots, N_u \text{ and } N_u \geq 2. \quad (5.63)$$

Above, s_u , δ_{jb} and w_{bu} are entries of matrices \mathbf{s} , $\mathbf{\Delta}$ and \mathbf{W} , respectively. The SIR on OFDM subcarrier p of user j is defined by the power ratio of self-signal and IUI on this subcarrier as

$$\text{SIR}_{j,p} = \frac{|\check{s}_{j,p}|^2}{|\bar{s}_{j,p}|^2}. \quad (5.64)$$

For an OFDM system, (5.64) is an important performance indicator, as it influences the amount of data that can be successfully transmitted on this subcarrier. It is noted that due to the Jensen's inequality [135], the mean value of (5.64) is larger or equal than the mean power ratio of the mean SIR (mean self-signal to mean IUI power):

$$\mathbb{E}_p \{ \text{SIR}_p \} \geq \frac{\mathbb{E} \{ |\check{s}_j|^2 \}}{\mathbb{E} \{ |\bar{s}_j|^2 \}} \triangleq \text{SIR}_j. \quad (5.65)$$

The SIR_j expression provided in (2.13) in Chapter 2 and used in (5.65), is slightly different than the analytical SIR results of Section 5.1. This happens because of the mathematical channel model used in Section 5.1, which considers the temporal channel correlation. This influences the mean power level of self-signal and IUI. However, for evaluating the SIR

Table 5.5: System level and channel predictor parameters

No. of base stations (N_b)	7
No. of terminals (N_u)	3
Feedback reporting interval (ΔT)	2 ms
Feedback delay / prediction horizon	5 ms
Channel observation time (T_{obs})	50 ms
No. of CSI quantization bits (B)	6 / channel tap
No. of estimated sub taps (S)	5 / channel tap
SNR for parameter extraction	20 dB

after channel prediction, we can only use the "hard" channel error measured by $\delta = \tilde{h} - h$, which does not consider any correlation between the channel used for precoding and the channel error. Numerical evaluation of the correlation between the actual channel and the channel error after prediction was found to be small enough to be neglected.

Figure 5.31 illustrates the CDF of the SIR per OFDM subcarrier, according to (5.63). The parameters used are listed in Table 5.5. Here, 7 base stations serve jointly 3 mobile users over the SCME with 30 km/h. The black (dashed) line shows the SIR at a time instant 5 ms after the ZF precoder calculation, if no channel prediction is used. The SIR statistics of the CoMP system without channel prediction is close the geometry factor observed by interference-limited (non-cooperative) transmission with a frequency reuse factor of 1 over the SCME, which is illustrated by the red (dashed-dotted) line. Practically this means that the generated IUI due to imperfect precoding is significantly high and eliminates the potential gains in terms of SIR enhancement of CoMP transmission. Note that this result was used in 3GPP LTE Release 10 as a main argument indicating that CoMP was considered promising but not yet mature enough to be included in the standard. Finally, the blue (solid) line shows the SIR, which is achieved when the precoder is updated by using the output of the Doppler-delay channel predictor. It can be observed that, using channel prediction, an SIR gain of 10 dB can be achieved. Obviously, the gains of CoMP can be realized only using predicted channels, if the users are mobile. The SIR when seven base stations serve four users is shown in Figure 5.32, from where it is observed that adding more users decreases the SIR.

In general, the impact of mobility on the channel MSE is very important. Considering e.g. a ten times lower mobility reduces the channel MSE by 20 dB, according to (5.30). Correspondingly, the post-prediction MSE will be reduced, which improves the mean SIR (2.14), as well as the full statistics of the SIR on each OFDM subcarrier, by 20 dB. This means that for short feedback delays and low, pedestrian type mobilities, channel aging effects are less critical.

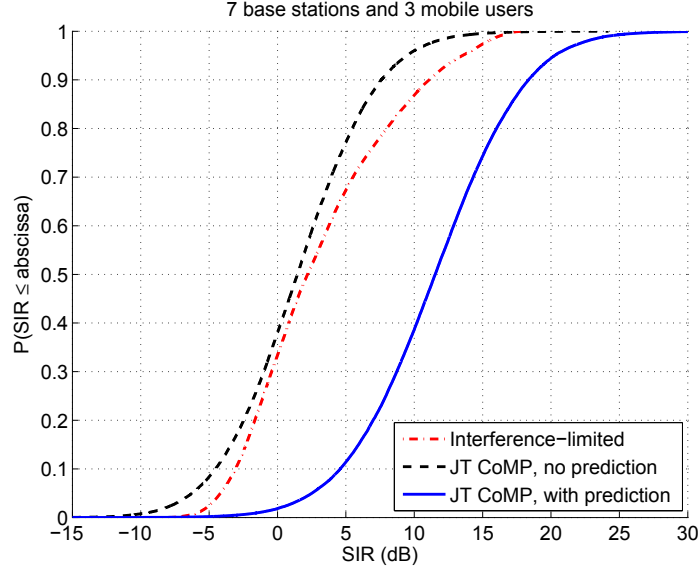


Figure 5.31: SIR for 7 BSs serving 3 users over the SCME with 30 km/h, 5 ms after precoder calculation. Channel prediction improves SIR by 10 dB. Without prediction, the SIR is close to the geometry factor of a non-coordinated network.

5.5 Summary of Chapter 5

In Section 5.1 of this chapter, a signal model for the downlink transmission in a multi-user multi-cellular systems with coordinated base stations using zero-forcing precoding was derived. The precoder was mismatched to the channel over which data was transmitted due to by imperfect channel estimation, CSI quantization and channel aging during the feedback delay. In the presence of channel impairments, each user receives a self-signal term and an additive term of inter-user interference. Exact expressions were derived for the mean power of those signals and for the resulting mean SIR of the jointly served users. It was found that if a desired mean SIR is targeted, and given a certain accuracy of channel estimation and quantization effects, there is a maximum tolerable feedback delay, which will also decrease with the mobility. The model provides clear insights into the tradeoff between channel estimation/quantization error and mobility/feedback delay, which can be used as guidelines for system design. Finally, the model was simplified and the channel impairments' effect was captured by the channel MSE, for which closed-form expressions and accurate approximations were derived for each impairment separately.

After having analyzed and evaluated the influence of channel impairment effects, mitigation tools and algorithmic approaches for dealing with it were developed. To this end, Section 5.2 introduced a practical feedback compression scheme for cooperative base stations. The method operates as follows: first, the channel to all nearby base stations is estimated from pilots symbols in the frequency domain and the strongest cells are identi-

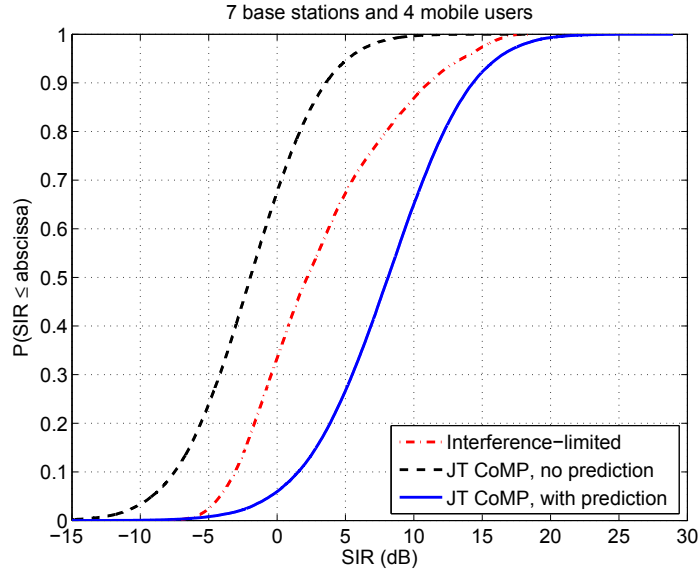


Figure 5.32: SIR for 7 BSs serving 4 users over the SCME with 30 km/h, 5 ms after precoder calculation. Channel prediction improves SIR by 10 dB. Without prediction, the SIR is close to the geometry factor of a non-coordinated network.

fied. Next, a time-domain representation of the channel is obtained and the most relevant taps are selected according to an estimated noise level. Adaptive quantization of the taps according to the SNR is used and it is shown that the feedback overhead is proportional to the SNR, which is also in line with the results of information theory. Finally, an interference-aware criterion is used for minimizing the number of quantization bits according to the out-of-cluster interference level. The scheme was evaluated over standard SCME as well as over measured channels. Without significantly enhancing the channel MSE, the required feedback for full CSI from all relevant cells in the cooperation cluster was reduced to 2.5 kbit per reporting interval at 20 MHz bandwidth. In summary, it was shown that the overhead for explicit multi-cell CSI feedback enabling JT CoMP can be reduced by 10 to 30 times, compared to scheme providing CSI for all 6 base stations for 144 pilots with 2 times 16 bit resolution for real and imaginary component for 4 individual links in our 2x2 MIMO configuration resulting into 55 kbit per reporting interval. It is noted that reduction of the feedback amount reduces the feedback delay likewise.

Section 5.3 presented a novel channel prediction mechanism based on a Doppler-delay model of the time-variant broadband channel. According to this method, channel taps are estimated over a short observation time, a high-resolution algorithm detects the major Doppler frequencies for each channel tap and channel prediction is performed by extrapolation of the time evolution of each tap. Results using the SCME as well as data from channel measurements indicated that the channel MSE can be reduced by around 10 dB for

typical feedback delays of 2 to 10 ms. This implies that larger feedback delays and higher mobility than previously believed, could be also supported in systems with cooperative base stations. It was also shown that the more complex procedure of Doppler frequencies estimation can be implemented at the base station, and that we can use quantized feedback information as an input without any significant performance degradation.

Section 5.4 evaluated the SIR gains achieved in JT CoMP using zero-forcing precoding, when deploying the above mitigation techniques of feedback compression and channel prediction. System-level simulations revealed an SIR enhancement around 10 dB can be achieved, which also depends on the number of base stations and mobile stations involved in the cooperation cluster.

Altogether, it was demonstrated thereby that a thorough understanding of the relevant impairment effects, in combination with effective feedback generation mechanisms and advanced prediction, is able to compensate the degradation effects of CoMP in realistic mobile scenarios. Taking these sophisticated algorithms into account, JT CoMP becomes more mature, and given the ever-increasing availability of signal processing, it may be useful and beneficial in a future standard.

6 Conclusions and Outlook

6.1 Summary and conclusions

In this work, wireless multi-cellular networks using coordinated multi-point (CoMP) have been investigated. The major difference to the vast of literature is the area that the transmission is subject to real-world impairments. Robustness to such impairments is important for practical implementation and use in mobile networks. The influence of channel and synchronization impairments onto the performance of the CoMP downlink has been investigated and the mechanisms responsible for limitation of the theoretical gains of CoMP have been analyzed and clarified.

The developed model has allowed for a thorough analysis of the degradation effects, while results have been verified by numerical simulations and evaluation over data from outdoor channel measurements. Novel mitigation techniques for compensation of the losses due to channel impairments and solutions for synchronizing distributed base stations have been proposed, forming practical concepts for CoMP system design.

At the beginning of this work, an introduction to multiple-input multiple-output (MIMO) was provided and it was explained how distributed CoMP increases the spectral efficiency of wireless cellular networks. A general multi-user multi-cellular signal model with zero-forcing (ZF) precoding based on imperfect channel knowledge was derived and used for power analysis of the users' self-signal and the inter-user interference. It was found that the signal-to-interference ratio (SIR) is inversely proportional to the mean square error (MSE) of the channel knowledge used for precoding. It also grows with the number of base stations and drops with the number of jointly served users. It was addressed how user selection can improve robustness against mismatched precoding and enhance the users' mean SIR.

The geographical limitations of the cooperation clusters were investigated, so that time synchronization of orthogonal frequency division multiplexing (OFDM) signals radiated from distributed base stations, thus arriving with propagation delay differences, and inter-symbol interference (ISI)-free removal of the cyclic prefix are feasible. Therefore, a statistical channel model was extended for broadband multi-point transmission and was first verified and parameterized in terms of root mean square (RMS) delay spread and 95% excess delay, based on outdoor measured channel data. It was interesting to observe that, when using a larger antenna downtilt, significantly smaller channel delay spreads can be realized and the inter-cell interference becomes more concentrated. Finally, channel delay statistics were predicted by using the parametrized model for larger inter-site

distances (ISDs). Results indicated that base station cooperation using Third Generation Partnership Project (3GPP) Long Term Evolution (LTE) system parameters is feasible for distances up to 1.7 km between the base stations at 2.65 GHz, without violating the short cyclic prefix more than 5% of the cases.

The MIMO signal model was extended for broadband systems using OFDM, while individual carrier frequency offsets (CFOs) and sampling frequency offsets (SFOs) were included on every transmitter and receiver branch. Based on this model, it was shown that the CFO has a significantly higher impact on the signal distortion than the SFO. It was also found that for unsynchronized CoMP systems, the caused inter-user interference dominates over the inter-carrier interference. The mean SIR drops quadratically with time and is inversely proportional to the variance of the base stations' CFOs. Following the general rule, the SIR also grows with the number of base stations and drops with the number of users. The model was simplified and the effect of imperfect carrier frequency synchronization was captured by its MSE, for which expressions were derived. Regarding system requirements, it was found that when a high SIR is targeted, oven-controlled crystal oscillators (OCXOs) locked to an accurate reference provided either by Global Positioning System (GPS) or by the backhaul network must be used at the base stations. Finally, Ethernet based IEEE1588 precision time protocol for network synchronization was discussed, especially for indoor base stations.

As a next step, the influence of channel impairments were investigated concretely. The joint transmission coordinated multi-point (JT CoMP) signal model from Chapter 2 was extended for mismatched precoding due to channel estimation, channel state information (CSI) quantization and channel aging during the feedback delay. The analytical SIR expressions were specialized, including critical parameters as mobility, feedback delay and estimation accuracy. It was shown that, if a desired SIR shall be attained and given a certain accuracy of channel estimation and quantization, there will be a maximum tolerable feedback delay for each mobility. Especially in its simplified form based on the channel MSE, our model provides practical insights, which can be used as system design guidelines. Evaluation results clearly revealed that the inter-user interference caused by mismatched precoding stemming from channel aging, limits significantly the potential performance gains of CoMP. In order to be able using CoMP for mobilities higher than pedestrian ones, mitigation techniques for coping with channel aging effects will be required.

As a first mitigation tool, an adaptive interference-aware feedback compression scheme was developed for JT CoMP. For the strongest cells, the most relevant channel taps are detected. By applying adaptive quantization to the selected taps according to the signal-to-noise ratio (SNR), the amount of feedback becomes proportional to the SNR, which is in line with the results of information theory. Interference-aware compression has been used for further reducing the number of quantization bits, with a small tolerable channel MSE. The scheme was evaluated over the spatial channel model extended (SCME) as well as over measured channels from the Fraunhofer Heinrich Hertz Institute (HHI) testbed. The

required feedback for full CSI for all relevant cells in the cooperation cluster was reduced to 2.5 kbit per reporting interval at 20 MHz bandwidth, which is 10 to 30 times less than uncompressed CSI to a ring of cells. The scheme was implemented on hardware and its real-time feasibility was demonstrated. It is also noted that reduction of the feedback overhead reduces the feedback delay likewise.

A further developed mitigation technique has been the Doppler-delay based channel prediction. According to this approach, channel taps have been estimated over a short observation time, before a high-resolution algorithm detects the major Doppler frequencies for each channel tap. Based on the acquired Doppler-delay channel representation, channel prediction was performed by time extrapolation. Evaluation with the SCME as well as using channel measurements indicated that the channel MSE can be reduced by around 10 dB for typical feedback delays of 2 to 10 ms, which is very close to the performance of Kalman filter predictors that require higher complexity. This MSE reduction implies that larger feedback delays and higher mobility than previously believed, can be supported in CoMP systems. It was also shown that the more complex part of the Doppler frequencies estimation can be implemented at the base station, without any significant performance degradation. The benefits of channel prediction for JT CoMP were evaluated by system level simulations, and SIR gains of around 10 dB were validated also in the multi-cell scenario.

In summary, it was demonstrated how part of the huge promises of CoMP can be realized in practice by including smart mitigation techniques. It was found that the major impairment lies in channel outdateding due to the mobility. A novel channel predictor was developed that makes the system more robust against mobility. It was found that the tight frequency synchronization requirements for distributed base stations can be fulfilled by technical solutions using today's commercial hardware. Outdoor channel measurements showed that inter-cell interference can be localized using antenna downtilt and that computational complexity as well as feedback and pilot overhead can be reduced by applying clustering and feedback compression techniques. Overall, the work presented in this thesis can be seen not only as a fundamental research, rather it is a contribution to the transition of CoMP from theory to practice.

6.2 Outlook towards next generation systems

In this work it was shown that CoMP is not only a promising technique in theory, but can be also included with practical concepts in next generation wireless communication systems. Practical enablers for synchronization, clustering, feedback compression and channel prediction can be included into such systems. Together with further system components such as multi-cell channel estimation, user selection and resource allocation, a concept will be possible to be realized for a full CoMP system. Such components have not been in the main focus of this work, though can be also considered as mature techniques [118, 136].

A robust CoMP technology will be a strong candidate for next-generation cellular systems and has been already discussed in the context of the coming 5G standard [69]. It is expected from 5G systems to fulfill high expectations of network operators and future demands. Such systems will have to support a multitude of new applications with a diverse set of requirements and characteristics, including higher peak and user data rates, reduced latency, enhanced indoor coverage and a large number of devices [137]. To this direction, current research investigates how to serve 10 to 100 times more devices, deliver 1000 times the traffic, and reduce the latency by a factor of 5 for mobile users, compared to the 3GPP LTE Release 8 to 11. Those already standardized systems include knowledge from research conducted over the last years and have been able to reach spectral efficiencies of 2-3 bits/s/Hz per macro-cell; outperforming them is already challenging.

As discussed in [87], the traffic growth expected in 10 or more years from now can be satisfied by the usage of more spectrum, higher spectral efficiency, and a densification of cells. This combination seems to be a reasonable breakdown of the main challenge of 1000 times more traffic into more manageable sub-terms. Practically this means the usage of high (mm-wave) frequencies, advanced interference mitigation techniques and the integration of *small cells*, resulting into so-called heterogeneous networks (HetNets) [138].

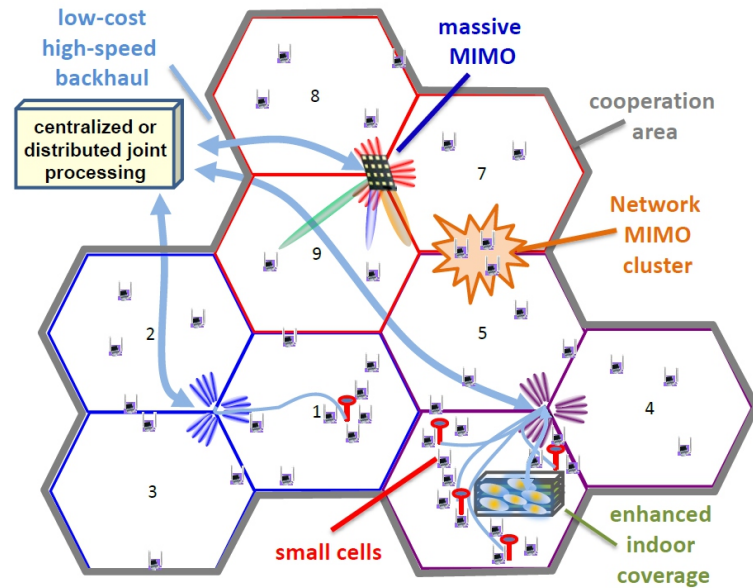


Figure 6.1: 5G network concept including small cells, CoMP, and massive MIMO.

To this end, a high-level perspective combination of small cells, JT CoMP and larger MIMO arrays (*massive MIMO*) [139] has been proposed in [87]. Under the term massive MIMO, a significant increase in the number of antennas at the base station and potentially also at the terminal has been proposed to enhance the spectral efficiency with affordable

complexity. Figure 6.1 shows the envisioned 5G system concept supporting key technologies for improving the spectral efficiency. Centralized or distributed joint signal processing controls the entire network. A high-speed backhaul network is needed to connect the cooperating base stations and exchange data and channel knowledge among them. First results based on measurements from our HHI testbed with macro-plus-small-cell scenarios showed that the spectral efficiency can be significantly improved by clustering and efficient user selection [63], and that our adaptive feedback compression scheme is capable for reducing the overhead. Moreover, it has been shown that fast feedback reporting combined with the proposed Doppler-delay channel prediction scheme are able to mitigate the impairment effects in coordinated networks.

Our vision for a next generation of wireless cellular techniques includes smart distributed signal processing as a powerful enabler for higher spectral efficiency. High-level coordination and network optimizations shall be supported with advanced algorithms for impairments' mitigation and robust transmission. The overall concepts shall consider high promising techniques as well as methods to meet the challenges they set, at reasonable costs of computational complexity and hardware.

7 Appendices

7.1 Appendices of Chapter 2

7.1.1 Mean value of the eigenvalues of the Wishart matrix

According to Theorem 1 in [35], the cumulative distribution function (CDF) $\rho(\lambda)$ of an eigenvalue λ of the Wishart-distributed matrix $\mathbf{H}\mathbf{H}^H$ is given by

$$\rho(\lambda) = \frac{1}{m} \sum_{i=1}^m [\phi_i^\alpha(\lambda)]^2 \lambda^\alpha e^{-\lambda}, \quad (7.1)$$

where $n = \max(N_r, N_t)$, $m = \min(N_r, N_t)$ and $\alpha = n - m$. N_r and N_t denote the number of receive and transmit antennas, respectively. The normalized functions

$$\phi_{k+1}^\alpha(\lambda) = \left[\frac{k!}{(k+\alpha)!} \right]^{\frac{1}{2}} L_k^\alpha(\lambda), \quad k = 0, \dots, m-1 \quad (7.2)$$

form an orthogonal set of polynomials with respect to the scalar product

$$\langle \phi_i^\alpha, \phi_j^\alpha \rangle = \int_0^\infty \phi_i^\alpha(\lambda) \phi_j^\alpha(\lambda) \lambda^\alpha e^{-\lambda} d\lambda = \delta_{ij}, \quad (7.3)$$

where $\delta_{ij} = 1$ for $i = j$ and $\delta_{ij} = 0$ else. $L_k^\alpha(\lambda)$ are the generalized Laguerre polynomials of degree k and order α , as described in [112].

The average eigenvalue $\mathbb{E}[\lambda]$ can be written as

$$\mathbb{E}[\lambda] = \int_0^\infty \lambda \cdot \rho(\lambda) d\lambda = \frac{1}{m} \sum_{k=0}^{m-1} \langle \phi_{k+1}^\alpha, \lambda \cdot \phi_{k+1}^\alpha \rangle. \quad (7.4)$$

According to [112], for the Laguerre polynomials following recursive formulas are known ($L_k^\alpha(\lambda)$ denoted as L_k^α for simplicity):

$$\lambda L_k^\alpha = (k + \alpha) L_k^{\alpha-1} - (k + 1) L_{k+1}^{\alpha-1} \quad (7.5)$$

and

$$L_k^{\alpha-1} = L_k^\alpha - L_{k-1}^\alpha. \quad (7.6)$$

We combine (7.5) and (7.6) in order to obtain all the polynomials with the same order α and to remove multiplication with λ within the scalar product in the sum on the right-hand side of expression (7.4). Due to orthogonality property (7.3), following term is simplified as:

$$\langle \phi_{k+1}^\alpha, \lambda \cdot \phi_{k+1}^\alpha \rangle = \alpha + 2k + 1. \quad (7.7)$$

By substituting (7.7) into (7.4), replacing $\alpha = n - m$ and considering a system with $N_t > N_r$ and thus $n = N_t$, results into

$$\mathbb{E}[\lambda] = \frac{1}{m} \sum_{k=0}^{m-1} (n - m + 2k + 1) = n = N_t. \quad (7.8)$$

7.1.2 Mean value of the inverse eigenvalues of the Wishart matrix

In equivalence to (7.4), the average of the inverse eigenvalue $\frac{1}{\lambda}$ is given by

$$\mathbb{E}\left[\frac{1}{\lambda}\right] = \int_0^\infty \frac{1}{\lambda} \cdot \rho(\lambda) d\lambda = \frac{1}{m} \sum_{k=0}^{m-1} \underbrace{\left\langle \phi_{k+1}^\alpha, \frac{1}{\lambda} \cdot \phi_{k+1}^\alpha \right\rangle}_{=X_k}, \quad (7.9)$$

where X_k is given by

$$X_k = \frac{k!}{(k + \alpha)!} \int_0^\infty e^{-\lambda} \lambda^{\alpha-1} L_k^\alpha(\lambda) L_{k'}^\alpha(\lambda) d\lambda. \quad (7.10)$$

From [112], is known for the Laguerre polynomials that

$$L_k^\alpha(\lambda) = \sum_{\nu=0}^k L_\nu^{\alpha-1}(\lambda). \quad (7.11)$$

By imposing (7.11) into (7.10) and using subindex μ for $L_{k'}^\alpha(\lambda)$, X_k can be expressed as

$$\begin{aligned} X_k &= \frac{k!}{(k + \alpha)!} \cdot \sum_{\nu=0}^k \left[\int_0^\infty e^{-\lambda} \lambda^{\alpha-1} L_\nu^{\alpha-1}(\lambda) L_\mu^{\alpha-1}(\lambda) d\lambda \right] \\ &= \frac{k!}{(k + \alpha)!} \cdot \underbrace{\sum_{\nu=0}^k \left[\frac{(\nu + \alpha - 1)!}{\nu!} \right]}_{= \frac{(\alpha+k)!}{\alpha k!}} = \frac{1}{\alpha}. \end{aligned} \quad (7.12)$$

In (7.12), due to the orthogonality properties of the Laguerre polynomials, only terms with $\nu = \mu$ are considered. For $\nu \neq \mu$, $X_k = 0$. Finally, by using (7.12) in (7.9), replacing $\alpha = n - m$ and considering $m = N_r$ and $n = N_t$ because of $N_t > N_r$, the average of the

inverse eigenvalue reaches

$$\mathbb{E} \left[\frac{1}{\lambda} \right] = \frac{1}{m} \cdot \sum_{k=0}^{m-1} \frac{1}{n-m} = \frac{1}{n-m} = \frac{1}{N_t - N_r}. \quad (7.13)$$

7.2 Appendices of Chapter 4

7.2.1 Analysis of K_U , K_{IUI} and K_{ICI}

The constants K_U , K_{IUI} and K_{ICI} are introduced in the main text in equations (4.26), (4.31) and (4.38), respectively. For identical channel statistics for all users and $K \triangleq \sum_{b=1}^{N_b} \mathbb{E} \{ |H_{jb} w_{bu}|^2 \}$, we have $K_U = 1 - K$, $K_{IUI} = (N_u - 1) \cdot K$ and $K_{ICI} = N_u \cdot K$. The following derivation gives an approximation for K in Rayleigh fading. The correlation between H_{jb} and w_{bu} can be considered as weak, because taking into account how the pseudo-inverse is calculated, there is only minor contribution of element H_{jb} to w_{bu} . Thus,

$$\begin{aligned} K &= \sum_{b=1}^{N_b} \mathbb{E} \{ |H_{jb} w_{bu}|^2 \} = \sum_{b=1}^{N_b} \mathbb{E} \{ |H_{jb}|^2 \mathbb{E} \{ |w_{bu}|^2 | H_{jb} \} \} \\ &\approx \sum_{b=1}^{N_b} \mathbb{E} \{ |H_{jb}|^2 \} \mathbb{E} \{ |w_{bu}|^2 \} = \sigma_h^2 \sum_{b=1}^{N_b} \mathbb{E} \{ |w_{bu}|^2 \}, \end{aligned} \quad (7.14)$$

where σ_h^2 is the mean channel power and $\mathbb{E} \{ \cdot | A \}$ denotes the conditional expectation given event A .

In [9], we analyzed (7.14) for zero-forcing (ZF) precoding of random matrices of dimension $N_u < N_b$ with complex Gaussian independent and identically distributed (i.i.d.) entries with zero mean and variance σ_h^2 . It is shown that

$$\sum_{b=1}^{N_b} \mathbb{E} \{ |w_{bu}|^2 \} = \frac{1}{\sigma_h^2 (N_b - N_u)} \geq \frac{1}{\sigma_h^2 N_b}. \quad (7.15)$$

The equality and bound in (7.15) can be used in (7.14) for calculating K and a bound for it, from where it is straightforward to obtain K_U , K_{IUI} and K_{ICI} and bounds for them. Those can then be used in (4.26), (4.31) and (4.38) in the main text.

7.2.2 Analysis of B_1 and B_2

We analyze $\sum_{\substack{\nu = -\frac{N_s}{2} \\ \nu \neq k}}^{\frac{N_s}{2}-1} \mathbb{E} \{ \beta_{jb_1}(k, \nu) \beta_{jb_2}^*(k, \nu) \}$, which is given in (4.35) in the main text,

while $\beta_{jb}(k, \nu)$ is given in (4.9). The base stations' and j^{th} mobile user's carrier frequency offsets (CFOs) are considered as i.i.d. Gaussian-distributed with zero mean and variance σ_f^2 and $\sigma_{f,j}^2$, respectively.

For the first case $b_1 = b_2 = b$, we proceed as follows:

$$\sum_{\substack{\nu=-\frac{N_s}{2} \\ \nu \neq k}}^{\frac{N_s}{2}-1} |\beta_{jb}(k, \nu)|^2 = \sum_{\nu=-\frac{N_s}{2}}^{\frac{N_s}{2}-1} |\beta_{jb}(k, \nu)|^2 - |\beta_{jb}(k, k)|^2 \quad (7.16)$$

$$= 1 - |\beta_{jb}(k, k)|^2 \quad (7.17)$$

$$= 1 - \frac{1}{N_s^2} \cdot \frac{\sin^2(\pi(f_j - f_b)TN_s)}{\sin^2(\pi(f_j - f_b)T)} \quad (7.18)$$

$$\approx \frac{\pi^2(f_j - f_b)^2}{3\delta^2} = \frac{\pi^2[(f_j - f_c) - (f_b - f_c)]^2}{3\delta^2}. \quad (7.19)$$

From (7.16) to (7.17) we used the result (7.24) of Appendix 7.2.3, which shows that the power of N_s samples of a function $\alpha(k) = \frac{1}{N_s} \frac{\sin(N_s \Phi(k))}{\sin(\Phi(k))}$ with $\Phi(k) = \pi k/N_s$, taken at frequencies $k + \phi$, is equal to 1 for any offset $\phi \in \mathbb{R}$. Imposing (4.9) into (7.17) gives (7.18). For typical values, the Taylor series expansion $\frac{1}{N_s^2} \frac{\sin^2(N_s x)}{\sin^2(x)} \approx 1 - \frac{1}{3} N_s^2 x^2$ ($N_s^2 - 1 \approx N_s^2$ for $N_s \gg 1$) is accurate and was used in (7.18) to reach (7.19). Note that $\delta = (N_s T)^{-1}$ is the subcarrier spacing. Taking the expectation of (7.19), and considering the independence between f_j and f_b , we reach

$$\sum_{\substack{\nu=-\frac{N_s}{2} \\ \nu \neq k}}^{\frac{N_s}{2}-1} \mathbb{E} \{ |\beta_{jb}(k, \nu)|^2 \} \approx \frac{\pi^2(\sigma_f^2 + \sigma_{f,j}^2)}{3\delta^2} \triangleq B_1. \quad (7.20)$$

For the second case $b_1 \neq b_2$, we have

$$\begin{aligned} \sum_{\substack{\nu=-\frac{N_s}{2} \\ \nu \neq k}}^{\frac{N_s}{2}-1} \mathbb{E} \{ \beta_{jb_1}(k, \nu) \beta_{jb_2}^*(k, \nu) \} &= \frac{1}{N_s^2} \cdot |\mathcal{F}_p(t_n)|^2 \\ &\cdot \sum_{\substack{\nu=-\frac{N_s}{2} \\ \nu \neq k}}^{\frac{N_s}{2}-1} \left| \mathbb{E} \left\{ \frac{\sin[\pi(k-\nu) + \pi(f_j - f_b)TN_s]}{\sin\left[\frac{\pi}{N_s}(k-\nu) + \pi(f_j - f_b)T\right]} \right\} \right|^2. \end{aligned} \quad (7.21)$$

Expression (7.21) was numerically evaluated and was found that for $f_j = f_c$ (perfectly synchronized mobiles) it is significantly smaller than (7.20). For $\sigma_{f,j} \geq \sigma_f$, and using $|\mathcal{F}_p(t_n)|^2 \approx 1$, (7.21) results into

$$\sum_{\substack{\nu=-\frac{N_s}{2} \\ \nu \neq k}}^{\frac{N_s}{2}-1} \mathbb{E} \{ \beta_{jb_1}(k, \nu) \beta_{jb_2}^*(k, \nu) \} \approx \frac{\pi^2 \sigma_{f,j}^2}{3\delta^2} \triangleq B_2. \quad (7.22)$$

Expressions (7.20) and (7.22) provide accurate approximations for B_1 and B_2 for Gaussian-distributed CFOs. Those results allow for taking the step from (4.36) to (4.37) in the main text.

7.2.3 Power of a periodic band-limited function sampled with an offset

Consider the function

$$\alpha(x) = \frac{1}{N_s} \sum_{n=-\frac{N_s}{2}}^{\frac{N_s}{2}-1} e^{j2\Phi(x)n} , \quad (7.23)$$

where $\Phi(x) = \pi x/N_s$. It can be seen that $\alpha(x)$ is a periodic band-limited function with period $T = N_s$ and Nyquist frequency $1/\Delta = 1$, and that $\alpha(x) = \frac{\sin(N_s \Phi(x))}{N_s \sin(\Phi(x))}$. We want to show that

$$\sum_{k=0}^{N_s-1} |\alpha(k + \phi)|^2 = \sum_{k=0}^{N_s-1} |\alpha(k)|^2 = 1 \quad (7.24)$$

for offset $\phi \in \mathbb{R}$. To prove this, we present following lemma.

Lemma: Let $\alpha(x) = \sum_{r=0}^{N-1} A_r \exp(j2\pi \frac{r}{T} x)$ be an arbitrary periodic band-limited function of period T with Fourier coefficients A_r . Lets define $\gamma^{(\phi)}(x)$ by sampling $\alpha(x)$ with frequency $1/\Delta$ and offset ϕ :

$$\gamma^{(\phi)}(x) = \alpha(x + \phi) \left(\sum_{k=-\infty}^{\infty} \delta(x - k\Delta) \right) = \sum_{k=-\infty}^{\infty} \alpha_k^{(\phi)} \delta(x - k\Delta) , \quad (7.25)$$

where $\alpha_k^{(\phi)} = \alpha(k\Delta + \phi)$, and $\delta(\cdot)$ is the delta distribution. Then, if $1/\Delta = N/T$ (which is the Nyquist frequency for $\alpha(x)$), the energy contained in one period of $\gamma^{(\phi)}$ is given by

$$\sum_{k=0}^{N-1} |\alpha_k^{(\phi)}|^2 = \frac{1}{\Delta} \int_0^T |\alpha(x)|^2 dx , \quad (7.26)$$

and therefore is independent of ϕ .

Proof: $\gamma^{(\phi)}$ is a periodic function for which we calculate Fourier coefficients $\Gamma_r^{(\phi)}$ in two ways.

First, if $\mathcal{F}\{f(x)\}(r) = 1/T \int_0^T f(x) \exp\{-j2\pi r x/T\} dx$ denotes the Fourier transform for a periodic function $f(x)$, using (7.25) one obtains

$$\Gamma_r^{(\phi)} = \left[\mathcal{F}\{\alpha(x + \phi)\}(s) * \mathcal{F}\left\{\sum_{k=-\infty}^{\infty} \delta(x - k\Delta)\right\}(s) \right](r) \quad (7.27)$$

$$= \left[\exp\left\{j2\pi \frac{s}{T} \phi\right\} A_s \right] * \left[\frac{1}{\Delta} \sum_{u=-\infty}^{\infty} \delta_s^{uN} \right](r) = \frac{\exp\left\{j2\pi \frac{r}{T} \phi\right\}}{\Delta} A_r , \quad (7.28)$$

where $r \in \mathbb{Z}$, $[a_s * b_s](r) = \sum_{s=-\infty}^{\infty} a_s b_{r-s}$ denotes the discrete linear convolution, δ_s^x is a sequence of numbers that has its s -th entry equal to 1 if $s = x$ and zero otherwise, and \check{r} is the smallest positive integer that satisfies $\check{r} \equiv r \pmod{N}$. If $r \in \{0, \dots, N-1\}$ then $\check{r} = r$.

Next, using (7.25) and the fact that $T = N\Delta$, the Fourier coefficient $\Gamma_k^{(\phi)}$ can also be found as:

$$\Gamma_r^{(\phi)} = \frac{1}{T} \int_{-\Delta/2}^{T-\Delta/2} \gamma^{(\phi)}(x) e^{-j2\pi \frac{r}{T}x} dx \quad (7.29)$$

$$= \frac{1}{T} \sum_{k=-\infty}^{\infty} \int_{-\Delta/2}^{(N-1/2)\Delta} \alpha_k^{(\phi)} \delta(x - k\Delta) e^{-j2\pi \frac{r}{T}x} dx \quad (7.30)$$

$$= \frac{1}{T} \sum_{k=0}^{N-1} \alpha_k^{(\phi)} e^{-j2\pi \frac{rk}{N}} \quad (7.31)$$

where (7.29) holds because the integral of a periodic function over its full period is translation invariant. Equation (7.31) implies that $\Gamma_r^{(\phi)}$ is the discrete Fourier transform (DFT) of $\alpha_k^{(\phi)}/T$, and therefore the DFT Parseval identity says that

$$\sum_{k=0}^{N-1} \left| \frac{\alpha_k^{(\phi)}}{T} \right|^2 = \frac{1}{N} \sum_{k=0}^{N-1} \left| \Gamma_r^{(\phi)} \right|^2. \quad (7.32)$$

Finally, using (7.28) with $r = r$ and (7.32), it can be proven that

$$\sum_{k=0}^{N-1} \left| \alpha_k^{(\phi)} \right|^2 = \frac{T^2}{N} \sum_{k=0}^{N-1} \left| \Gamma_r^{(\phi)} \right|^2 \quad (7.33)$$

$$= \frac{T^2}{N} \sum_{k=0}^{N-1} \left| \frac{\exp\{j2\pi \frac{r}{T}\phi\}}{\Delta} A_r \right|^2 \quad (7.34)$$

$$= N \sum_{k=0}^{N-1} |A_r|^2 \quad (7.35)$$

$$= \frac{N}{T} \int_0^T |\alpha(x)|^2 dx, \quad (7.36)$$

which is what we wanted to prove in (7.24). Note that (7.36) is obtained from (7.35) using the Parseval identity for Fourier Series.

7.3 Appendices of Chapter 5

7.3.1 High resolution estimator

We observe each of the $l = 1 \dots L$ channel taps for a period of time and estimate the Doppler frequencies. The observation of one channel tap over Q time samples can be modeled as

$$\mathbf{y}_{l,q} = \mathbf{h}_{l,q} + \mathbf{n}_{l,q}, \quad q \in \{1, 2, \dots, Q\} \quad (7.37)$$

where $\mathbf{y}_{l,q}$ is the channel observation of $\mathbf{h}_{l,q}$ at Q sample points in the time domain and $\mathbf{n}_{l,q}$ is additive white Gaussian noise (AWGN). We estimate S sub taps and their individual Doppler frequencies from the observation $\mathbf{y}_{l,q}$ in an iterative fashion in order to find a representation $\hat{\mathbf{h}}_{l,q}$ of the temporal channel tap evolution where most of the noise shall have been removed.

In each iteration step, we estimate the Doppler frequency $f_{l,s}$ of the s^{th} sub tap by

$$f_{l,s} = \arg \max_{f_s} \left| \sum_{q=1}^Q \mathbf{g}_{l,q} \cdot e^{-2\pi j \cdot f_s \cdot \frac{q-1}{Q}} \right|. \quad (7.38)$$

For the first step we use $\mathbf{g}_{l,q} = \mathbf{y}_{l,q}$ from (7.37). The search interval for the Doppler frequency is limited within $-f_D \leq f_{l,s} < f_D$, with f_D being the maximum value according to terminal velocity. For the amplitude $\alpha_{l,s}$ and phase $\phi_{l,s}$ follows

$$\alpha_{l,s} \cdot e^{j\phi_{l,s}} = \sum_{q=1}^Q \mathbf{g}_{l,q} \cdot e^{2\pi j \cdot f_{l,s} \cdot \frac{q-1}{Q}}. \quad (7.39)$$

In further iteration steps we can update $\mathbf{g}_{l,q}$ in following two ways, which are shown as iterative loops in the algorithm flow chart in Figure 7.1.subtap

1) We want to estimate a new Doppler frequency and already know S frequencies (outer loop in Figure 7.1). Therefore we remove all previously detected frequency components from the observation $\mathbf{y}_{l,q}$.

$$\mathbf{g}_{l,q}^{(S+1)} = \mathbf{y}_{l,q} - \sum_{s=1}^S \alpha_{l,s} \cdot e^{j\phi_{l,s}} \cdot e^{2\pi j \cdot f_{l,s} \cdot \frac{q-1}{Q}} \quad (7.40)$$

2) The values $\alpha_{l,s}$, $\phi_{l,s}$ and $f_{l,s}$ of each estimated sub tap are distorted by interference from the following (still undetected) sub taps and also by approximation errors of already estimated ones. We can increase the precision of an already detected Doppler frequency k by setting $\mathbf{g}_{l,q}$ to

$$\mathbf{g}_{l,q}^{(k)} = \mathbf{y}_{l,q} - \sum_{\forall s \neq k}^S \alpha_{l,s} \cdot e^{j\phi_{l,s}} \cdot e^{2\pi j \cdot f_{l,s} \cdot \frac{q-1}{Q}} \quad (7.41)$$

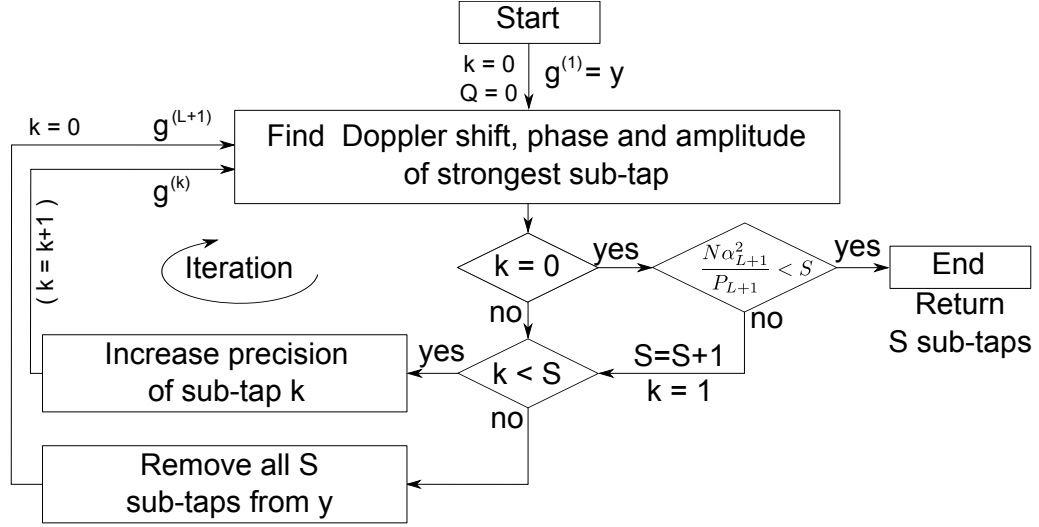


Figure 7.1: Flow chart of the iterative Doppler frequency detection with adaptive thresholding. The inner iteration loop can be repeated more than once for each detected frequency, resulting in further precision improvements.

and repeating the calculation for this tap (inner loop in Figure 7.1). Candes and Tao [140] state that for a sparse \mathbf{h} , which is satisfied when there are less sub-taps than input time samples, we can find a $\hat{\mathbf{h}}$ such that the mean square error (MSE) is within a factor of $\log Q$ of the ideal MSE:

$$\|\hat{\mathbf{h}} - \mathbf{y}\|^2 = O(\log Q) \cdot \mathbb{E}\{\|\mathbf{y} - \mathbf{h}\|^2\}. \quad (7.42)$$

Donoho and Johnstone [141] state that thresholding achieves the ideal MSE with a threshold level $\sqrt{2 \cdot \log Q} \cdot \sigma_n^2$. In general, the exact number of sub-taps is unknown. We can gain knowledge about the noise power σ_n^2 , and thus the threshold from the link budget. Nevertheless, if the exact value σ_n^2 is also unknown and we can certify that if $S \ll Q$, we can set the threshold in an adaptive fashion (if Q is not large enough compared to S the detection fails). When a new Doppler frequency is found, we update the power after removing all detected taps according to

$$P_{S+1} = \sum_{q=1}^Q \left(\mathbf{y}_{l,q} - \sum_{s=1}^{S+1} \alpha_{l,s} \cdot e^{j\phi_{l,s}} \cdot e^{-2\pi j \cdot f_{l,s} \cdot \frac{q-1}{Q}} \right)^2 \quad (7.43)$$

When there are S sub-taps above and the $(S+1)^{\text{st}}$ sub-taps falls below the threshold and it is provided that $|\mathbf{n}|^2 \sim \chi_2^2$, then we can set $\sigma_n^2 = 2 \cdot P_{S+1}$ and stop the iterative estimation when

$$\alpha_{S+1}^2 < \underbrace{2 \cdot \sqrt{2 \cdot \log Q}}_{=Th} \cdot \frac{P_{S+1}}{Q}, \quad (7.44)$$

where Th is the threshold level. When (7.44) is fulfilled, the $(S + 1)^{\text{st}}$ Doppler frequency is not any more part of $\hat{\mathbf{h}}_{l,q}$.

The output of the iterative Doppler frequency estimation can be used to de-noise the input data and to get an estimate of the signal-to-noise ratio (SNR). We therefore calculate $\hat{\mathbf{h}}$ at the same channel tap delays as in the original channel (7.37). The effective SNR then notes

$$\begin{aligned}
 p^{(\text{equiv})} &= \sum_{q=1}^Q \left| \hat{\mathbf{h}}_{l,q} \right|^2 \\
 p^{(\text{noise})} &= \sum_{q=1}^Q \left| \mathbf{y}_{l,q} - \hat{\mathbf{h}}_{l,q} \right|^2 \\
 \text{SNR}_{\text{dB}} &\approx 10 \cdot \log_{10} \left(\frac{p^{(\text{equiv})} - \frac{3S}{2Q} \cdot p^{(\text{noise})}}{(1 + \frac{3S}{2Q}) \cdot p^{(\text{noise})}} \right)
 \end{aligned} \tag{7.45}$$

The factor $\frac{3S}{2Q}$ accounts for the remaining noise which is proportional to the number of estimated sub taps.

List of Abbreviations

3GPP	Third Generation Partnership Project
AWGN	additive white Gaussian noise
BER	bit error rate
BS	base station
CDMA	Code Division Multiple Access
CDF	cumulative distribution function
CFO	carrier frequency offset
CFR	channel frequency response
CIR	channel impulse response
CoMP	coordinated multi-point
CP	cyclic prefix
CPE	common phase error
CSI	channel state information
CSIT	channel state information at the transmitter
DFT	discrete Fourier transform
FDD	frequency division duplex
FDMA	Frequency Division Multiple Access
FFT	fast Fourier transform
GSM	Global System for Mobile Communications
HHI	Fraunhofer Heinrich Hertz Institute
HR	high-resolution
HSPA+	Evolved High-Speed Packet Access
ICI	inter-carrier interference
IDFT	inverse discrete Fourier transform
IFFT	inverse fast Fourier transform
i.i.d.	independent and identically distributed
ISD	inter-site distance
ISI	inter-symbol interference
IUI	inter-user interference
JT	joint transmission
JT CoMP	joint transmission coordinated multi-point
GPS	Global Positioning System
KLT	Karhunen-Loève transform
LOS	line-of-sight

LTE	Long Term Evolution
LTE-A	Long Term Evolution – Advanced
MIMO	multiple-input multiple-output
ML	maximum-likelihood
MMSE	minimum mean square error
MRC	maximum ratio combining
MSE	mean square error
NLOS	non-line-of-sight
nSE	normalized square error
OCXO	oven-controlled crystal oscillator
OFDM	orthogonal frequency division multiplexing
OFDMA	orthogonal frequency division multiple access
PAPR	peak-to-average power ratio
pdf	probability distribution function
PDP	power delay profile
PPS	pulse per second
RD	rate-distortion
RMS	root mean square
SCME	spatial channel model extended
SFO	sampling frequency offset
SIR	signal-to-interference ratio
SISO	single-input single-output
SLNR	signal-to-leakage-and-noise ratio
SNR	signal-to-noise ratio
SVD	singular value decomposition
TDD	time division duplex
TDMA	Time Division Multiple Access
THP	Tomlinson-Harashima precoding
T-Labs	Telekom Innovation Laboratories
TUB	Technische Universität Berlin
UMTS	Universal Mobile Telecommunication System
V-BLAST	Vertical Bell Labs Space-Time
WSSUS	wide-sense stationary uncorrelated scattering
WLAN	wireless local area network
w.r.t.	with respect to
ZF	zero-forcing

List of Figures

2.1	Spectral efficiency according to Shannon's formula for serial ($N_t = 1$ stream) and parallel ($N_t = 4$ streams) data transmission versus the SNR [38].	12
2.2	Principle of a parallel data transmission in a MIMO system. Here, signal processing at the receiver is used for separating the multiple data streams [38].	13
2.3	Application of MIMO concepts, as given in [38]: <i>Left</i> : CSI at the receiver is useful for the uplink. <i>Center</i> : CSI at the transmitter is useful in the downlink. <i>Right</i> : CSI at both ends is useful for peer-to-peer links.	14
2.4	Distributed JT CoMP with two base stations and two terminals (FDD mode). Joint data precoding based on channel information feedback and synchronized base stations allow for inter-user interference-free data reception [38].	16
2.5	The multi-cell testbed of the Fraunhofer Heinrich Hertz Institute, located in the Technische Universität Berlin campus in the city center of Berlin, Germany.	19
2.6	Sources of mismatched precoding in FDD systems: channel estimation at the terminal and CSI feedback quantization, channel aging during the feedback delay and imperfect sampling and carrier frequencies at the base station. . .	20
2.7	Based on analysis and signal modeling, impairments can be captured by their MSE, vital for signal-to-interference ratio (SIR) analysis, link-layer abstraction and system-level evaluation.	24
2.8	Mean SIR upper bound (2.17) (analytical) and for Rayleigh fading channel (2.14) (analytical and numerical). $N_b = 7$ base stations (BSs) jointly serve N_u users with zero-forcing, normalized MSE is set to -35 dB, -25 dB and -15 dB.	25
2.9	Statistics of SIR measured per OFDM subcarrier for $N_b = 7$ BSs serving $N_u = \{3; 6\}$ terminals in Rayleigh fading channel and for different MSE values.	26
3.1	The cyclic prefix "absorbs" multipath echoes from the previous OFDM symbol and protects from inter-symbol interference. It also relaxes time synchronization requirements.	30

3.2	<i>Left</i> : Basic interference scenario. <i>Center</i> : Cells are identified using a frequency domain comb individually shifted in each cell. Antennas in the cell are identified by time-domain sequences. <i>Right</i> : Frequency reuse in cellular networks [38].	33
3.3	RMS delay spread measurements. The main beam of antennas meets the ground at a distance of 0.9 times the inter-site distance.	36
3.4	Multi-cell 95% excess delay measurements. The main beam of antennas meets the ground at a distance of 0.9 times the inter-site distance.	37
3.5	Multi-cell 95% excess delay measurements. The main beam of antennas meets the ground at a distance of 0.33 times the inter-site distance.	38
3.6	Multi-cell RMS delay spread (τ_{RMS}); main beam of antennas hits the ground at 0.9 or 0.33 times the inter-site-distance. Model is used for prediction at positions at least 210 m away from the base stations.	39
3.7	Multi-cell 95% excess delay (τ_{95}). The main beam of antennas hits the ground at 0.9 or 0.33 times the inter-site-distance. Model is used for prediction at positions at least 210 m away from the base stations.	39
3.8	Predicted multi-cell RMS delay spread (τ_{RMS}) for larger inter-site-distances and uniform user allocation between the base stations.	40
3.9	Predicted multi-cell 95% excess delay (τ_{95}) for larger inter-site-distances and uniform user allocation between the base stations.	40
4.1	Single-link system where transmitter and receiver have individual sampling periods T_i and T_j for digital-to-analog and analog-to-digital conversion and individual carrier frequencies f_i and f_j for up- and down-conversion.	43
4.2	Mean power of inter-user and inter-carrier interferences in a Rayleigh fading channel. Here, 7 base stations serve 3 and 6 users, respectively. Analytical results (4.33) and (4.38) are shown by lines, while markers show respective numerical evaluations of (4.14) and (4.15).	57
4.3	Mean SIR over time for Rayleigh fading channel and SIR upper bound. Here, 7 base stations using oscillators of accuracy given by Osc serve jointly 3 users. Analytical results are shown by lines, simulations by markers.	59
4.4	Mean SIR over time for Rayleigh fading channel and SIR upper bound. Here, 7 base stations using oscillators of accuracy given by Osc serve jointly 6 users. Analytical results are shown by lines, simulations by markers.	60
4.5	Mean users' SIR 10 ms after most recent precoder update, for the Rayleigh fading and upper bound. Here, 7 base stations serve jointly from 2 to 6 users. Analytical results are shown by lines, simulations by markers.	61
4.6	Equivalent channel MSE due to oscillator CFO. <i>solid</i> : numerical evaluation of exact expression (4.47); <i>dashed</i> : analytical approximation (4.48).	63

5.1	Sources of mismatched precoding in an FDD system: channel estimation, CSI quantization and channel aging during the feedback delay and CSI exchange delay over the backhaul network.	68
5.2	Required CSI accuracy after channel estimation/quantization vs. normalized feedback time, for attaining certain mean SIR levels in JT CoMP with 7 base stations and 5 users, in a Rayleigh fading channel, according to (5.24).	73
5.3	MSE due to channel aging according to numerical evaluation and exact analytic expression (5.26), second and fourth order approximation (5.30).	75
5.4	System model of the CSI feedback compression scheme. Solid lines connect the blocks for noise-based feedback compression; dashed lines connect the blocks for interference-aware compression.	79
5.5	Channel tap estimation from frequency domain pilots: smoothening window, reduced inverse discrete Fourier transform (IDFT) matrix, channel tap selection by AWGN estimation and removal and adaptive quantization.	80
5.6	Left: Estimated SNR vs. real SNR after four iterations and by using $\alpha = 4$ for threshold calculation in (5.42). Right: An SNR gain of around 7 dB is observed after noise removal.	81
5.7	The number of estimated taps grows linearly with the SNR before reaching a ceiling at the level given by the number of actual taps, which is here 18.	82
5.8	The PAPR lies between 7 and 17 dB for the SCME channel.	84
5.9	Number of quantization bits according to (5.54) with $\vartheta = 0$ dB, evaluated over a large number of channel realizations. The red dashed line corresponds to the rate-distortion function, which can be regarded as lower bound.	85
5.10	CDF of the normalized square error, evaluated for SCME on OFDM subcarriers as in (5.55): after IDFT (green), after tap selection (red) and after quantization with $\vartheta = 0$ dB and $\vartheta = 6$ dB (black and blue). The initial mean SNR is 10 dB.	86
5.11	Feedback packet format for multi-cell CSI. The number of bits is given in brackets for each field.	87
5.12	Frequency of cluster size appearance according to the threshold κ , set to 6, 12 and 18 dB; <i>Left</i> : downtilt of 0.33 ISD; <i>Right</i> : downtilt of 0.9 ISD.	89
5.13	Inter-cluster geometry factor \mathcal{G} in dB, according to (5.38), without clustering and for a cluster threshold κ of 6, 12 and 18 dB; <i>Left</i> : measurement with downtilt of 0.33 ISD; <i>Right</i> : SCME channel model.	89
5.14	CDF of feedback per reporting interval for different clustering thresholds κ . <i>Left</i> : noise-aware, <i>Right</i> : interference-aware feedback compression. <i>Solid lines</i> : measurement track shown in Figure 5.15. <i>Dashed lines</i> : SCME with 7 cells and one user in the middle cell.	90

5.15	CDF of feedback per reporting interval for all clustered cells after interference-aware compression. An antenna downtilt of 0.33 ISD is used and the clustering threshold set to $\kappa = 12$ dB. Transmit directions are shown by arrows.	91
5.16	CDF of feedback per reporting interval for all clustered cells after interference-aware compression. An antenna downtilt of 0.9 ISD is used and the clustering threshold set to $\kappa = 12$ dB. Transmit directions are shown by arrows.	92
5.17	Multi-cellular multi-user channel prediction scheme: channel parameter extraction, CSI feedback and channel prediction can be split as modules between terminals and base stations. Data precoding uses the predicted channel.	93
5.18	Blocks of the Doppler-delay channel prediction: channel tap identification, Doppler frequency estimation per tap and channel prediction by extrapolation.	93
5.19	Examples of accurate channel tap reconstruction for observation time $[-31, 0]$ ms. Prediction for $[1; 20]$ ms may diverge from the actual channel. Here, the 5 strongest out of 20 existent sub taps are used in the SCME.	95
5.20	Implementation of the total channel prediction procedure at the terminal. .	97
5.21	Channel MSE after Doppler-delay based prediction, using perfect CSI as an input. For feedback delays above 4 ms, estimating more than 3 Doppler frequencies does not offer additional MSE gains.	98
5.22	Channel MSE for Doppler frequency estimation at different SNR levels. The high-resolution estimator performs stable with noisy inputs.	99
5.23	Channel taps are estimated and quantized at the terminal (left) and fed back to the base station (right), where Doppler frequency estimation and channel prediction are performed.	99
5.24	Normalized MSE for Doppler-delay based channel prediction at the base station for an observation history of 32 ms, using as input quantized CSI, available every 1 ms. SCME with 30 km/h is used, while SNR is equal to 20 dB.	100
5.25	For typical feedback delays, channel prediction reduces the normalized channel square error (nSE) by around 10 dB. Here, 6 bits/tap quantization is used.	101
5.26	Impact of the CSI reporting interval on the prediction performance.	102
5.27	Channel taps and Doppler frequencies are estimated at the terminal (left), quantized and fed back to the base station (right), where channel prediction is performed.	102
5.28	Impact of channel observation time (T_{obs}) onto the MSE. T_{obs} should be chosen according to the prediction horizon. Here, perfect CSI was assumed and 10 sub taps/tap were used.	103

5.29	Estimation of 10 sub taps from perfect CSI slightly improves the MSE for short delays, compared to estimating 6 sub taps. For noisy and quantized CSI, the MSE cannot be further reduced by using more sub taps.	104
5.30	Channel prediction MSE for Doppler-delay based and Kalman filtering prediction, both using a 10 th order model. Perfect CSI at subcarriers has been used as an input. Both methods offer similar and significant MSE reduction.	105
5.31	SIR for 7 BSs serving 3 users over the SCME with 30 km/h, 5 ms after precoder calculation. Channel prediction improves SIR by 10 dB. Without prediction, the SIR is close to the geometry factor of a non-coordinated network.	108
5.32	SIR for 7 BSs serving 4 users over the SCME with 30 km/h, 5 ms after precoder calculation. Channel prediction improves SIR by 10 dB. Without prediction, the SIR is close to the geometry factor of a non-coordinated network.	109
6.1	5G network concept including small cells, CoMP, and massive MIMO. . . .	114
7.1	Flow chart of the iterative Doppler frequency detection with adaptive thresholding. The inner iteration loop can be repeated more than once for each detected frequency, resulting in further precision improvements.	124

List of Tables

3.1	Measurement parameters	34
3.2	Model parameters extracted from measurement	36
5.1	System and channel parameters	88
5.2	Frequency of cluster size appearance (%)	88
5.3	3GPP LTE system parameters	96
5.4	SCME channel parameters	97
5.5	System level and channel predictor parameters	107

Publication List

- [1] Konstantinos Manolakis, Christian Oberli, Volker Jungnickel, and Fernando Rosas. Analysis of synchronization impairments for cooperative base stations using OFDM. *International Journal on Antennas and Propagation, Hindawi Publications*, 2015. in press.
- [2] Volker Jungnickel, Konstantinos Manolakis, Wolfgang Zirwas, Berthold Panzner, Mikael Sternad, and Tommy Svensson. The role of small cells, coordinated multi-point and massive MIMO in 5G. *IEEE Communications Magazine*, May 2014.
- [3] Konstantinos Manolakis, Volker Jungnickel, Christian Oberli, Thorsten Wild, and Volker Braun. An overview of impairments in CoMP and mitigation techniques. In *33rd Meeting of the World Wide Research Forum (WWRF): 5G Beyond the Headlines*, Guilford, United Kingdom, September 2014.
- [4] Fernando Rosas, Lurys Herrera, Christian Oberli, Konstantinos Manolakis, and Volker Jungnickel. Downlink performance limitations of cellular systems with coordinated base stations and mismatched precoder. *IET Communications*, Jan. 2014.
- [5] Konstantinos Manolakis, Miguel Angel Gutierrez-Estevez, and Volker Jungnickel. Adaptive modulation and turbo coding for 3GPP LTE systems with limited feedback. In *79th Vehicular Technology Conference (VTC)*, Seoul, Republic of Korea, May 2014.
- [6] Konstantinos Manolakis, Volker Jungnickel, Christian Oberli, Thorsten Wild, and Volker Braun. Impairments in cooperative mobile networks: Models, impact on performance and mitigation. In *20th European Wireless Conference*, Barcelona, Spain, May 2014. invited.
- [7] Konstantinos Manolakis, Stephan Jaeckel, Volker Jungnickel, and Volker Braun. Channel prediction by doppler-delay analysis and benefits for base station cooperation. In *IEEE 77th Vehicular Technology Conference (VTC)*, Dresden, Germany, June 2013. Best Paper Award.
- [8] Konstantinos Manolakis, Christian Oberli, Lurys Herrera, and Volker Jungnickel. Analytical models for channel aging and synchronization errors for base station cooperation. In *21st European Signal Processing Conference (EUSIPCO)*, Marrakech, Morocco, September 2013.

- [9] Konstantinos Manolakis, Christian Oberli, and Volker Jungnickel. Random matrices and the impact of imperfect channel knowledge on cooperative base stations. In *14th International Workshop on Signal Processing Advances for Wireless Communications (SPAWC)*, Darmstadt, Germany, June 2013. invited.
- [10] Volker Jungnickel, Konstantinos Manolakis, Stephan Jaeckel, Moritz Lossow, Peter Farkas, Michael Schlosser, and Volker Braun. Backhaul requirements for inter-site cooperation in heterogeneous LTE-Advanced networks. In *IEEE International Conference on Communications (ICC)*, Budapest, Hungary, June 2013. invited.
- [11] Lars Schulz, Konstantinos Manolakis, and Volker Jungnickel. Adaptive Feedback Compression for Joint Transmission Coordinated Multi-Point. In *IEEE 77th Vehicular Technology Conference (VTC)*, Dresden, Germany, June 2013.
- [12] Miguel Angel Gutierrez-Estevez, Udo Krüger, Kirsten Krüger, Konstantinos Manolakis, Volker Jungnickel, Katrin Jaksch, Kai Krüger, Stefan Mikulla, Robert Giese, Michael Sohmer, and Matthias Reich. Acoustic broadband communications over deep drill strings using adaptive OFDM. In *IEEE Wireless Communications and Networking Conference (WCNC)*, Shanghai, China, April 2013.
- [13] Miguel Angel Gutierrez-Estevez, Udo Krüger, Kirsten Krüger, Konstantinos Manolakis, and Volker Jungnickel. Acoustic channel model for a drill string to optimize OFDM transmission. In *38th International Conference on Acoustics, Speech, and Signal Processing (ICASSP)*, Vancouver, Canada, May 2013.
- [14] Miguel Angel Gutierrez-Estevez, K. A. Krüger, Kirsten Krüger, M. Groh, A. Jurczyk, M. Sohmer, Udo Krüger, Volker Jungnickel, Konstantinos Manolakis, Katrin Jaksch, R. Giese, and M. Reich. Vibrationen aus der Tiefe. Wie neue Mobilfunktechniken helfen, große Datenmengen in kürzerer Zeit akustisch über einen Bohrstrang zu übertragen. In *DGMK/ÖGEW-Frühjahrstagung, Fachbereich Aufsuchung und Gewinnung*, Celle, Germany, April 2013.
- [15] Volker Jungnickel, Holger Gaebler, Udo Krüger, Konstantinos Manolakis, and Thomas Haustein. LTE trials in the return channel over satellite. In *6th Advanced Satellite Multimedia Systems Conference (ASMS)*, pages 238–245, Baiona, Spain, September 2012.
- [16] V. Jungnickel, M. A. Gutierrez Estevez, K. A. Krüger, U. Krüger, K. Manolakis, R. Giese, M. Groh, K. Jaksch, A. Jurczyk, K. Krüger, S. Mikulla, S. Weisheit, M. Reich, and M. Sohmer. Anwendung der neuesten Mobilfunktechniken auf akustische Wellen zur Verbesserung der Kommunikation in der Tiefbohrtechnik. In *DGMK/ÖGEW-Frühjahrstagung 2012, Fachbereich Aufsuchung und Gewinnung, April 2012*, Celle, Germany, April 2012.

- [17] K. Jaksch, M. A. Gutierrez Estevez, K. A. Krüger, U. Krüger, K. Manolakis, R. Giese, M. Groh, V. Jungnickel, A. Jurczyk, K. Krüger, S. Mikulla, S. Weisheit, M. Reich, and M. Sohmer. Projekt SPWD-BUSData: Übertragung seismischer Daten mittels akustischer Wellen entlang des Bohrstranges. In GtV Bundesverband Geothermie, editor, *Der Geothermie Kongress*, Karlsruhe, Germany, November 2012.
- [18] Konstantinos Manolakis, Stephan Jaeckel, Eva Salvador Márquez, and Volker Jungnickel. Impact of path loss and delay spread on base station cooperation. In *5th European Conference on Antennas and Propagation (EuCAP)*, Rome, Italy, April 2011.
- [19] Konstantinos Manolakis, Lars Thiele, Christian Oberli, Thomas Haustein, and Volker Jungnickel. Impairment modeling for joint transmission CoMP. In *2nd International Conference on Wireless Communications, Vehicular Technology, Information Theory and Aerospace & Electronic System Technology (Wireless VITAE)*, Chennai, India, March 2011.
- [20] Konstantinos Manolakis, Udo Krüger, Kirsten Krüger, Miguel Angel Gutierrez-Estevez, Stefan Mikulla, and Volker Jungnickel. Borehole communication with acoustic OFDM. In *16th International OFDM-Workshop 2011 (InOWo)*, Hamburg, Germany, September 2011.
- [21] Konstantinos Manolakis, Christian Oberli, and Volker Jungnickel. Synchronization requirements for OFDM-based cellular networks with coordinated base stations: Preliminary results. In *15th International OFDM-Workshop*, Hamburg, Germany, September 2010.
- [22] Wen Xu and Konstantinos Manolakis. Robust synchronization for 3GPP LTE system. In *IEEE Global Communications Conference (Globecom 2010)*, Miami, Florida, USA, December 2010.
- [23] Konstantinos Manolakis, David-Manuel Gutierrez-Estevez, Volker Jungnickel, Wen Xu, and Christian Drewes. A closed concept for synchronization and cell search in 3GPP LTE systems. In *IEEE Wireless Communications and Networking Conference 2009 (WCNC)*, Budapest, Hungary, April 2009.
- [24] V. Jungnickel, K. Manolakis, L. Thiele, T. Wirth, and T. Haustein. Handover sequences for interference-aware transmission in multicell MIMO networks. *Workshop on Smart Antennas (WSA)*, Feb. 2009.
- [25] Konstantinos Manolakis and Volker Jungnickel. Synchronization and cell search for 3GPP LTE. In *13th International OFDM Workshop (InOWo)*, Hamburg, Germany, August 2008.

- [26] Konstantinos Manolakis, Andreas Ibing, and Volker Jungnickel. Performance evaluation of a 3GPP LTE terminal receiver. In *European Wireless Conference*, Prague, Czech Republic, June 2008.
- [27] Andreas Ibing and Konstantinos Manolakis. MMSE channel estimation and time synchronization tracking for cooperative MIMO-OFDM with propagation delay differences. In *IEEE International Symposium on Wireless Communication Systems (ISWCS)*, Reykjavik, Iceland, October 2008.
- [28] Malte Schellmann, Konstantinos Manolakis, Andreas Ibing, and Marcel Kuszak. Impact of the preamble bandwidth on the synchronization performance. In *12th International OFDM-Workshop (InOWo)*, Hamburg, Germany, August 2007.
- [29] V. Jungnickel, M. Schellmann, A. Forck, H. Gäbler, S. Wahls, A. Ibing, K. Manolakis, T. Haustein, W. Zirwas, J. Eichinger, E. Schulz, C. Juchems, F. Luhn, and R. Zavrtak. Demonstration of virtual MIMO in the uplink. In *IET Smart Antennas and Cooperative Communications Seminar*, London, United Kingdom, October 2007. invited.

Bibliography

- [30] C. Oberli, “ML-based tracking algorithms for MIMO-OFDM,” *IEEE Transactions on Wireless Communications*, vol. 6, no. 7, pp. 2630–2639, 2007.
- [31] 3rd Generation Partnership Project, *TS 36.300, V11.7.0, Evolved Universal Terrestrial Radio Access (E-UTRA) and Evolved Universal Terrestrial Radio Access Network (E-UTRAN); Overall description*, 3GPP Std., Sep 2013.
- [32] —, *TR 25.996 V11.0.0 Technical Specification Group Radio Access Network; Spatial channel model for Multiple Input Multiple Output (MIMO) simulations*, 3GPP Std., Sept 2012.
- [33] C. E. Shannon, “A mathematical theory of communication,” *The Bell System Technical Journal*, vol. 27, pp. 379 – 423, 623–656, October 1948.
- [34] G. J. Foschini and M. J. Gans, “On limits of wireless communications in a fading environment when using multiple antennas,” *Wireless Personal Communications*, vol. 6, pp. 311–335, 1998.
- [35] E. Telatar, “Capacity of multi-antenna gaussian channels,” *European Transactions on Telecommunications*, vol. 10, no. 6, pp. 585–595, 1999.
- [36] M. Karakayali, G. Foschini, and R. Valenzuela, “Network coordination for spectrally efficient communications in cellular systems,” *IEEE Wireless Communications*, vol. 13, no. 4, pp. 56–61, 2006.
- [37] R. Irmer, H. P. Mayer, A. Weber, V. Braun, M. Schmidt, M. Ohm, N. Ahr, A. Zoch, C. Jandura, P. Marsch, and G. Fettweis, “Multisite field trial for LTE and advanced concepts,” *IEEE Communications Magazine*, vol. 47, no. 2, pp. 92–98, 2009.
- [38] V. Jungnickel, “Multiple antennas in mobile networks. from fundamentals to network mimo experiments,” Habilitation thesis, Technische Universität Berlin, 2013.
- [39] J. Winters, “Optimum combining in digital mobile radio with cochannel interference,” *IEEE Transactions on Vehicular Technology*, vol. 33, no. 3, pp. 144 – 155, Aug. 1984.
- [40] —, “On the capacity of radio communication systems with diversity in a rayleigh fading environment,” *IEEE Journal on Selected Areas in Communications*, vol. 5, no. 5, pp. 871–878, Jun 1987.

- [41] G. J. Foschini, "Layered space-time architecture for wireless communication in a fading environment when using multi-element antennas," *Bell Labs Technical Journal*, vol. 1, no. 2, pp. 41–59, Autumn 1996.
- [42] C. Eckart and G. Young, "A Principal Axis Transformation for Non-Hermitian Matrices," *Bull. Am. Math. Society*, vol. 45, no. 2, pp. 118–121, 1939, <http://projecteuclid.org/euclid.bams/1183501633>.
- [43] P. Wolniansky, G. Foschini, G. Golden, and R. Valenzuela, "V-BLAST: an architecture for realizing very high data rates over the rich-scattering wireless channel," in *URSI International Symposium on Signals, Systems, and Electronics*, Sep 1998, pp. 295–300.
- [44] C. Windpassinger, R. F. H. Fischer, and J. Huber, "Lattice-reduction-aided broadcast precoding," *IEEE Transactions on Communications*, vol. 52, no. 12, pp. 2057–2060, Dec 2004.
- [45] M. H. M. Costa, "Writing on dirty paper," *IEEE Transactions on Information Theory*, vol. 29, no. 3, pp. 439–441, 1983.
- [46] G. Caire and S. Shamai, "On the achievable throughput of a multiantenna gaussian broadcast channel," *IEEE Transactions on Information Theory*, vol. 49, no. 7, pp. 1691–1706, July 2003.
- [47] S. Vishwanath, N. Jindal, and A. Goldsmith, "Duality, achievable rates, and sum-rate capacity of gaussian MIMO broadcast channels," *IEEE Transactions on Information Theory*, vol. 49, no. 10, pp. 2658–2668, Oct 2003.
- [48] M. Schubert and H. Boche, "Solution of the multiuser downlink beamforming problem with individual SINR constraints," *IEEE Transactions on Vehicular Technology*, vol. 53, no. 1, pp. 18–28, Jan 2004.
- [49] Q. Spencer, A. Swindlehurst, and M. Haardt, "Zero-forcing methods for downlink spatial multiplexing in multiuser MIMO channels," *IEEE Transactions on Signal Processing*, vol. 52, no. 2, pp. 461–471, 2004.
- [50] F. Boccardi and H. Huang, "A near-optimum technique using linear precoding for the MIMO broadcast channel," in *IEEE International Conference on Acoustics, Speech and Signal Processing (ICASSP)*, vol. 3, April 2007, pp. III–17–III–20.
- [51] G. Lebrun, J. Gao, and M. Faulkner, "MIMO transmission over a time-varying channel using SVD," *IEEE Transactions on Wireless Communications*, vol. 4, no. 2, pp. 757–764, March 2005.

-
- [52] G. Foschini, K. Karakayali, and R. Valenzuela, "Coordinating multiple antenna cellular networks to achieve enormous spectral efficiency," *IEE Proceedings on Communications*, vol. 153, no. 4, pp. 548–555, 2006.
 - [53] D. Gesbert, M. Kountouris, R. Heath, C.-B. Chae, and T. Salzer, "Shifting the MIMO paradigm," *IEEE Signal Processing Magazine*, vol. 24, no. 5, pp. 36–46, 2007.
 - [54] M. Sharif and B. Hassibi, "On the capacity of MIMO broadcast channels with partial side information," *IEEE Transactions on Information Theory*, vol. 51, no. 2, pp. 506 – 522, feb 2005.
 - [55] A. Goldsmith, S. Jafar, N. Jindal, and S. Vishwanath, "Capacity limits of MIMO channels," *IEEE Journal on Selected Areas in Communications*, vol. 21, no. 5, pp. 684–702, 2003.
 - [56] Q. Spencer, C. Peel, A. Swindlehurst, and M. Haardt, "An introduction to the multi-user MIMO downlink," *IEEE Communications Magazine*, vol. 42, no. 10, pp. 60 – 67, oct. 2004.
 - [57] H. Huang and S. Venkatesan, "Asymptotic downlink capacity of coordinated cellular networks," in *Asilomar Conference on Signals, Systems and Computers*, vol. 1, Nov 2004, pp. 850–855 Vol.1.
 - [58] V. Jungnickel, S. Jaeckel, L. Thiele, U. Krüger, A. Brylka, and C. von Helmolt, "Capacity measurements in a multicell MIMO system," in *IEEE Global Telecommunications Conference (GLOBECOM)*, San Francisco, California, Nov. 2006.
 - [59] V. Jungnickel, S. Jaeckel, L. Thiele, L. Jiang, U. Kruger, A. Brylka, and C. von Helmolt, "Capacity measurements in a cooperative MIMO network," *IEEE Transactions Vehicular Technology*, vol. 58, no. 5, pp. 2392 –2405, Jun. 2009.
 - [60] A. Papadogiannis, D. Gesbert, and E. Hardouin, "A dynamic clustering approach in wireless networks with multi-cell cooperative processing," in *IEEE International Conference on Communications (ICC)*. IEEE, 2008, pp. 4033–4037.
 - [61] H. Huang, M. Trivellato, A. Hottinen, M. Shafi, P. Smith, and R. Valenzuela, "Increasing downlink cellular throughput with limited network MIMO coordination," *IEEE Transactions on Wireless Communications*, vol. 8, no. 6, pp. 2983–2989, 2009.
 - [62] W. Zirwas, W. Mennerich, and A. Khan, "Main enablers for advanced interference mitigation," *Transactions on Emerging Telecommunications Technologies*, vol. 24, no. 1, pp. 18–31, 2013.
 - [63] M. Lossow, S. Jaeckel, V. Jungnickel, and V. Braun, "Efficient MAC Protocol for JT CoMP in Small Cells," in *IEEE 2nd International Workshop on Small Cell Wireless Networks (SmallNets)*, June 2013.

- [64] V. Jungnickel, A. Forck, S. Jaeckel, F. Bauermeister, S. Schiffermueller, S. Schubert, S. Wahls, L. Thiele, T. Haustein, W. Kreher, J. Mueller, H. Droste, and G. Kadel, "Field trials using coordinated multi-point transmission in the downlink," in *IEEE 21st International Symposium on Personal, Indoor and Mobile Radio Communications Workshops (PIMRC)*, 2010.
- [65] F. Boccardi, B. Clerckx, A. Ghosh, E. Hardouin, G. Jöngren, K. Kusume, E. Onggosanusi, and Y. Tang, "Multiple-antenna techniques in LTE-advanced," *IEEE Communications Magazine*, vol. 50, no. 3, pp. 114–121, 2012.
- [66] D. Lee, H. Seo, B. Clerckx, E. Hardouin, D. Mazzaresse, S. Nagata, and K. Sayana, "Coordinated multipoint transmission and reception in LTE-advanced: deployment scenarios and operational challenges," *IEEE Communications Magazine*, vol. 50, no. 2, pp. 148–155, 2012.
- [67] R. Irmer, H. Droste, P. Marsch, M. Grieger, G. Fettweis, S. Brueck, H. P. Mayer, L. Thiele, and V. Jungnickel, "Coordinated multipoint: Concepts, performance, and field trial results," *IEEE Communications Magazine*, vol. 49, no. 2, 2011.
- [68] X. Tao, X. Xu, and Q. Cui, "An overview of cooperative communications," *IEEE Communications Magazine*, 2012.
- [69] A. Osseiran, F. Boccardi, V. Braun, K. Kusume, P. Marsch, M. Maternia, O. Queuth, M. Schellmann, H. Schotten, H. Taoka, H. Tullberg, M. Uusitalo, B. Timus, and M. Fallgren, "Scenarios for the 5G mobile and wireless communications: The vision of the METIS project," *IEEE Communications Magazine*, may 2014.
- [70] S. Haykin, *Adaptive filter theory*, 4th ed. Prentice Hall, 2001.
- [71] N. Goodman, "Statistical analysis based on a certain multivariate complex gaussian distribution (an introduction)," *The Annals of Mathematical Statistics*, vol. 34, nr. 1, pp. 152–177, 1963.
- [72] V. Jungnickel, T. Haustein, E. Jorswieck, and C. von Helmolt, "On linear pre-processing in multi-antenna systems," in *Global Telecommunications Conference (GLOBECOM)*, Taipei, Taiwan, nov 2002, pp. 1012 – 1016.
- [73] P. Shaman, "The inverted complex wishart distribution and its application to spectral estimation," *Journal of Multivariate Analysis*, vol. 10, no. 1, 1980.
- [74] D. Maiwald and D. Kraus, "Calculation of moments of complex wishart and complex inverse wishart distributed matrices," *IEE Proceedings on Radar, Sonar and Navigation*, vol. 147, no. 4, pp. 162 –168, aug 2000.

-
- [75] L. Greenstein, V. Erceg, Y. Yeh, and M. Clark, "A new path-gain/delay-spread propagation model for digital cellular channels," *IEEE Transactions on Vehicular Technology*, vol. 46, no. 2, pp. 477–485, 1997.
 - [76] E. Sousa, V. Jovanovic, and C. Daigneault, "Delay spread measurements for the digital cellular channel in toronto," *IEEE Trans. Veh. Technol.*, vol. 43, no. 4, pp. 837–847, 1994.
 - [77] C.-X. Wang, X. Hong, X. Ge, X. Cheng, G. Zhang, and J. Thompson, "Cooperative mimo channel models: A survey," *IEEE Communications Magazine*, vol. 48, no. 2, pp. 80–87, Feb 2010.
 - [78] S. Jaeckel, L. Thiele, A. Brylka, L. Jiang, and V. Jungnickel, "Intercell interference measured in urban areas," *IEEE International Conference on Communications (ICC)*, 2009.
 - [79] V. Jungnickel, M. Schellmann, L. Thiele, T. Wirth, T. Haustein, O. Koch, E. Zirwas, and E. Schulz, "Interference aware scheduling in the multiuser MIMO-OFDM downlink," *IEEE Communications Magazine*, vol. 47, pp. 56–66, 2009.
 - [80] S. Jaeckel, L. Thiele, and V. Jungnickel, "Interference limited MIMO measurements," *IEEE Vehicular Technology Conference (VTC)*, 2010.
 - [81] L. Thiele, T. Wirth, K. Börner, M. Olbrich, V. Jungnickel, J. Rumold, and S. Fritze, "Modeling of 3D field patterns of downtilted antennas and their impact on cellular systems," *Proc. Workshop on Smart Antennas (WSA)*, 2009.
 - [82] T. M. Schmidl and D. C. Cox, "Robust frequency and timing synchronization for ofdm," *IEEE Transactions on Communications*, vol. 45, no. 12, pp. 1613–1621, 1997.
 - [83] J.-J. van de Beek, M. Sandell, and P. O. Börjesson, "ML estimation of time and frequency offset in OFDM systems," *IEEE Transactions on Signal Processing*, vol. 45, no. 7, pp. 1800–1805, 1997.
 - [84] T. S. Rappaport, *Wireless Communication - Principles and Practice*. Prentice Hall, 2002.
 - [85] V. Jungnickel, L. Thiele, T. Wirth, T. Haustein, S. Schiffermuller, A. Forck, S. Wahls, S. Jaeckel, S. Schubert, H. Gabler, C. Juchems, F. Luhn, R. Zavrtak, H. Droste, G. Kadel, W. Kreher, J. Mueller, W. Stoermer, and G. Wannemacher, "Coordinated multipoint trials in the downlink," in *Global Communications Conference (GLOBECOM)*. IEEE, 2009.
 - [86] S. Jaeckel and V. Jungnickel, "Estimating MIMO Capacities from Broadband Measurements in a Cellular Network," in *European Conference on Antennas and Propagation*, Barcelona, Spain, 2010.

- [87] V. Jungnickel, K. Manolakis, W. Zirwas, B. Panzner, M. Sternad, and T. Svensson, "The role of small cells, coordinated multipoint and massive MIMO in 5G," *IEEE Communications Magazine*, May 2014.
- [88] M. Speth, S. Fechtel, G. Fock, and H. Meyr, "Optimum receiver design for wireless broad-band systems using OFDM: Part I," *IEEE Transactions on Communications*, vol. 47, no. 11, pp. 1668–1677, 1999.
- [89] L. Häring, S. Bieder, A. Czylik, and T. Kaiser, "Estimation algorithms of multiple channels and carrier frequency offsets in application to multiuser OFDM systems," *IEEE Transactions on Wireless Communications*, vol. 9, no. 3, 2010.
- [90] M. Schellmann and V. Jungnickel, "Multiple CFOs in OFDM-SDMA uplink: Interference analysis and compensation," *EURASIP Journal on Wireless Communications and Networking*, vol. 2009, no. 1, 2009.
- [91] C. Oberli and M. Rios, "OFDM-based SDMA networks: Signal model under imperfect synchronization and channel state information," in *12th International OFDM Workshop (InOWo)*, Hamburg, Germany, Aug. 2007.
- [92] K. Manolakis, C. Oberli, and V. Jungnickel, "Synchronization requirements for OFDM-based cellular networks with coordinated base stations: Preliminary results," in *15th International OFDM-Workshop*, Hamburg, Germany, Sep. 2010.
- [93] P. Marsch and G. Fettweis, Eds., *Coordinated Multi-Point in Mobile Communications: From Theory to Practice*. Cambridge University Press, 2011.
- [94] R. Mudumbai, D. Brown, U. Madhow, and H. Poor, "Distributed transmit beamforming: challenges and recent progress," *IEEE Communications Magazine*, vol. 47, no. 2, pp. 102–110, 2009.
- [95] T. Koivisto and V. Koivunen, "Impact of time and frequency offsets on cooperative multi-user MIMO-OFDM systems," in *IEEE 20th International Symposium on Personal, Indoor and Mobile Radio Communications (PIMRC)*, 2009.
- [96] —, "Low complexity estimation of multiple frequency offsets using optimized training signals," in *IEEE 11th International Symposium on Spread Spectrum Techniques and Applications (ISITA)*, 2010.
- [97] B. Zarikoff and J. Cavers, "Multiple frequency offset estimation for the downlink of coordinated MIMO systems," *IEEE Journal on Selected Areas in Communications*, vol. 26, no. 6, pp. 901–912, August 2008.
- [98] —, "Coordinated multi-cell systems: Carrier frequency offset estimation and correction," *IEEE Journal on Selected Areas in Communications*, vol. 28, no. 9, pp. 1490–1501, December 2010.

-
- [99] Y.-R. Tsai, H.-Y. Huang, Y.-C. Chen, and K.-J. Yang, "Simultaneous multiple carrier frequency offsets estimation for coordinated multi-point transmission in OFDM systems," *IEEE Transactions on Wireless Communications*, vol. 12, no. 9, pp. 4558–4568, 2013.
- [100] V. Kotzsch and G. Fettweis, "Interference analysis in time and frequency asynchronous network MIMO OFDM systems," in *IEEE Wireless Communications and Networking Conference (WCNC)*, 2010, pp. 1–6.
- [101] I. Brown, D.R. and H. Poor, "Time-slotted round-trip carrier synchronization for distributed beamforming," *IEEE Transactions on Signal Processing*, vol. 56, no. 11, pp. 5630–5643, 2008.
- [102] V. Jungnickel, T. Wirth, M. Schellmann, T. Haustein, and W. Zirwas, "Synchronization of cooperative base stations," in *IEEE International Symposium on Wireless Communication Systems (ISWCS)*, 2008.
- [103] R. Rogalin, O. Bursalioglu, H. Papadopoulos, G. Caire, A. Molisch, A. Michaloliakos, V. Balan, and K. Psounis, "Scalable synchronization and reciprocity calibration for distributed multiuser MIMO," *IEEE Transactions on Wireless Communications*, vol. 13, no. 4, pp. 1815–1831, April 2014.
- [104] O. Simeone, U. Spagnolini, Y. Bar-Ness, and S. H. Strogatz, "Distributed synchronization in wireless networks," *IEEE Signal Processing Magazine*, vol. 25, no. 5, pp. 81–97, 2008.
- [105] C. Oberli, "Erratum to ML-based tracking algorithms for MIMO-OFDM," *available upon request*, 2007.
- [106] F. Rosas, L. Herrera, C. Oberli, K. Manolakis, and V. Jungnickel, "Downlink performance limitations of cellular systems with coordinated base stations and mismatched precoder," *IET Communications*, Jan. 2014.
- [107] A. Papoulis, *Probability, Random Variables and Stochastic Processes*. Mc-Graw Hill, 1991.
- [108] K. Seong, M. Mohseni, and J. Cioffi, "Optimal resource allocation for OFDMA downlink systems," in *IEEE International Symposium on Information Theory*, July 2006, pp. 1394–1398.
- [109] S. Shi, M. Schubert, and H. Boche, "Rate optimization for multiuser MIMO systems with linear processing," *IEEE Transactions on Signal Processing*, vol. 56, no. 8, pp. 4020–4030, 2008.

- [110] M. A. Lombardi, L. M. Nelson, A. N. Novick, and V. S. Zhang, "Time and frequency measurements using the global positioning system," *Cal Lab: International Journal of Metrology*, vol. 8, no. 3, pp. 26–33, 2001.
- [111] "IEEE standard for a precision clock synchronization protocol for networked measurement and control systems," *IEEE Std 1588-2008 (Revision of IEEE Std 1588-2002)*, pp. c1–269, July 2008.
- [112] I. S. Gradshteyn and I. M. Ryzhik, *Table of integrals, series, and products*, 7th ed. Elsevier/Academic Press, Amsterdam, 2007.
- [113] V. Jungnickel, A. Forck, T. Haustein, S. Schiffermüller, C. von Helmolt, F. Luhn, M. Pollock, C. Juchems, M. Lampe, W. Zirwas, J. Eichinger, and E. Schulz, "1Gbit/s MIMO-OFDM Transmission Experiments," in *Proc. 62nd IEEE Vehicular Technology Conference (VTC)*, vol. 2, Dallas, USA, Sep. 2005, pp. 861–866.
- [114] P. Noll, "A comparative study of various quantization schemes for speech encoding," *The Bell System Technical Journal*, vol. 54, no. 9, pp. 1597 – 1614, nov 1975.
- [115] V. Jungnickel, S. Jaeckel, K. Börner, M. Schlosser, and L. Thiele, "Estimating the mobile backhaul traffic in distributed coordinated multi-point systems," in *Workshop on Hybrid Optical Wireless Access Networks Program, Wireless Communications and Networking Conference (WCNC)*, Paris, France, Apr. 2012.
- [116] D. J. Love, R. Heath, V. K. Lau, D. Gesbert, B. D. Rao, and M. Andrews, "An overview of limited feedback in wireless communication systems," *IEEE Journal on Selected Areas in Communications*, vol. 26, no. 8, pp. 1341–1365, 2008.
- [117] T. Wild, "Coping with out-of-cluster leakage in downlink coordinated multi-point," in *8th International Symposium on Wireless Communication Systems (ISWCS)*, 2011, pp. 710–714.
- [118] P. Baracca, F. Boccardi, and V. Braun, "A dynamic joint clustering scheduling algorithm for downlink CoMP systems with limited CSI," in *9th International Symposium on Wireless Communication Systems (ISWCS)*. Paris, France: IEEE, Aug 2012, pp. 830–834.
- [119] G. Caire and H. Shirani-Mehr, "Feedback schemes for multiuser MIMO-OFDM downlink," in *Information Theory and Applications Workshop*, 2008.
- [120] H. Minn and V. Bhargava, "An investigation into time-domain approach for OFDM channel estimation," *IEEE Transactions on Broadcasting*, vol. 46, no. 4, pp. 240–248, Dec 2000.

-
- [121] S. Lee, D. Kwon, G. Caire, and H. Shirani-Mehr, "Method for channel state feedback by quantization of time-domain coefficients," USA Patent US20 090 185 607, Jul., 2009, uS Patent App. 12/274,046.
 - [122] N. Jindal, "MIMO broadcast channels with finite-rate feedback," *IEEE Transactions on Information Theory*, vol. 52, no. 11, pp. 5045–5060, Nov 2006.
 - [123] T. Wild, "A rake-finger based efficient channel state information feedback compression scheme for the MIMO-OFDM FDD downlink," in *71st Vehicular Technology Conference (VTC)*. IEEE, may 2010.
 - [124] T. Wild, L.-H. Nguyen, and S. ten Brink, "Multi-stage channel estimation across multiple cells in uplink joint reception," in *77th Vehicular Technology Conference (VTC)*, 2013.
 - [125] D. Baum, J. Hansen, and J. Salo, "An interim channel model for beyond-3G systems: extending the 3gpp spatial channel model (SCM)," in *IEEE 61st Vehicular Technology Conference*, May 2005.
 - [126] S. Jaeckel and V. Jungnickel, "Multi-cell outdoor MIMO-measurements," *VDE Kongress*, vol. 1, pp. 101–106, 2006.
 - [127] S. Zhou and G. Giannakis, "How accurate channel prediction needs to be for transmit-beamforming with adaptive modulation over rayleigh mimo channels?" *IEEE Transactions on Wireless Communications*, vol. 3, no. 4, pp. 1285 – 1294, july 2004.
 - [128] M. Sternad and D. Aronsson, "Channel estimation and prediction for adaptive OFDM downlinks [vehicular application]," in *58th Vehicular Technology Conference (VTC)*, vol. 2, 2003, pp. 1283–1287.
 - [129] L. Thiele, M. Olbrich, M. Kurras, and B. Matthiesen, "Channel aging effects in CoMP transmission: gains from linear channel prediction," in *Asilomar Conference on Signals, Systems and Computers*, nov. 2011.
 - [130] R. Apelfröjd, M. Sternad, and D. Aronsson, "Measurement-based evaluation of robust linear precoding for downlink CoMP," in *IEEE International Conference on Communications (ICC)*, Ottawa, Canada, 2012.
 - [131] D. Aronsson, "Channel estimation and prediction for MIMO OFDM systems: Key design and performance aspects of kalman-based algorithms," Ph.D. dissertation, Uppsala University, 2011.
 - [132] I. Wong, A. Forenza, R. Heath, and B. Evans, "Long range channel prediction for adaptive OFDM systems," in *Asilomar Conference on Signals, Systems and Computers*, nov. 2004.

- [133] N. Palleit and T. Weber, "Time prediction of non flat fading channels," in *IEEE International Conference on Acoustics, Speech and Signal Processing (ICASSP)*, 2011, pp. 2752–2755.
- [134] J. Medbo, I. Siomina, A. Kangas, and J. Furuskog, "Propagation channel impact on LTE positioning accuracy: A study based on real measurements of observed time difference of arrival," in *IEEE 20th International Symposium on Personal, Indoor and Mobile Radio Communications*, Sept 2009.
- [135] F. Hansen and G. K. Pedersen, "Jensen's Operator Inequality," *ArXiv Mathematics e-prints*, Apr. 2002.
- [136] T. Wild, L.-H. Nguyen, and S. ten Brink, "Joint channel estimation across multiple cells in coordinated multi-point," in *International Symposium on Wireless Communication Systems (ISWCS)*, 2012.
- [137] "Net!works european platform, broadband wireless beyond 2020," May 2011.
- [138] D. Lopez-Perez, I. Guvenc, G. De La Roche, M. Kountouris, T. Q. Quek, and J. Zhang, "Enhanced intercell interference coordination challenges in heterogeneous networks," *IEEE Wireless Communications*, vol. 18, pp. 22–30, 2011.
- [139] E. G. Larsson, F. Tufvesson, O. Edfors, and T. L. Marzetta, "Massive MIMO for next generation wireless systems," *IEEE Communications Magazine*, 2013.
- [140] E. Candes and T. Tao, "The dantzig selector: statistical estimation when p is much larger than n ," 2005.
- [141] D. L. Donoho and I. M. Johnstone, "Ideal denoising in an orthonormal basis chosen from a library of bases," *Comptes Rendus Acad. Sci., Ser. I*, vol. 319, pp. 1317–1322, 1994.